Thermochemical Evaluation of Sustainable Sorbents for Ammonia Gas Sequestration

By

Marlon V. Ramlogan

A dissertation submitted to the

Graduate School-Newark

Rutgers, The State University of New Jersey

In partial fulfillment of requirements

For the degree of

Doctor of Philosophy

Graduate Program in Environmental Sciences

Written under the direction of

Dr. Ashaki A. Rouff

and approved by

_____

_____

_____

_____

Newark, New Jersey

May, 2020

ABSTRACT OF THE DISSERTATION

Thermochemical Evaluation of Sustainable Sorbents for Ammonia Gas Sequestration

By Marlon V. Ramlogan

Dissertation Director:

Dr. Ashaki A. Rouff

Atmospheric ammonia gas ($NH_3(g)$) forms particulate matter, negatively impacting human and environmental health. Agriculture is the largest source of $NH_3(g)$, primarily emitted from nitrogen (N) fertilizers and livestock waste. Sustainable sorbents for managing N-volatilization from agriculture is urgently needed to promote N-conservation. Sorbents reclaimed from agricultural wastes may be viable substrates. Struvite ($MgNH_4PO_4 \cdot 6H_2O$), reclamation in nutrient-rich wastewaters encourages recycling of N and phosphorus (P) from wastes.

Thermal analysis (TA) indicated struvite thermally decomposes, undergoing phase transitions at various temperatures, releasing partial to complete water vapor ($H_2O(g)$), and N as $NH_3(g)$. Volatilizing ammonium ($NH_4^+(s)$) from struvite at low temperatures may enhance struvite's potential for capture of $NH_3(g)$.

Comparing struvite-based sorbents, with conventional biochar and MOF sorbents, for $NH_3(g)$ sequestration, a simultaneous thermal analysis-pulse thermal analysis-Fourier transform infrared spectroscopy (STA-PTA-FTIR) technique was used. Sorbents were obtained by heating commercial struvite (HTS) from 55-300 °C, and struvite-bearing solids recovered from swine (S, 95-98% struvite) and dairy (D, 28-33% struvite) livestock waste to 150 and 300 °C. For HTS sorbents, HTS-150 resulted in highest uptake (23.5 mg $NH_3(g)$ g^{-1} sorbent). For S sorbents, heating to 150 °C (S-150) enhanced sorption capacity (47.2-49.9 mg $NH_3(g)$ g^{-1} sorbent) compared to unheated solids (9.9-11.2 mg $NH_3(g)$ g^{-1} sorbent). Heating D solids caused marginal increases in $NH_3(g)$ sorption, and was therefore not as effective, likely due to high calcite content. Biochar (BC) uptake (50.8 mg $NH_3(g)$ g^{-1} sorbent) was similar to S-150; and MOF was significantly higher (289.7 mg $NH_3(g)$ g^{-1} sorbent). After desorption, HTS-150 (38%) and BC (41%) were found to retain similar percentages of $NH_3(g)$.

Sorption-desorption enthalpies indicated sorption mechanisms were physisorption and chemisorption to solid-state FTIR binding sites.

For HTS sorption, speciation of reactive sites was more important than surface area. Sorption-desorption kinetic parameters were calculated from TA curves by model-dependent kinetics. Model-independent kinetics described sorption-desorption as fast, with simultaneous and rate-limiting steps.

The STA and kinetic modeling confirm high-struvite content solids from livestock wastes are promising non-traditional sorbents for NH_3(g) sequestration. This work demonstrated STA-PTA-FTIR is an ideal technique for evaluation of gas sorption-desorption phenomena, providing fundamental data comparing common and novel, sustainably-sourced sorbents for NH_3(g) sequestration.

Acknowledgement

Without a doubt, the first and single most important statement of thankfulness is reserved for my mentor and advisor, Dr. Ashaki Rouff. Professor Rouff brought me into the world of environmental geochemistry, and I became very interested in her work on struvite. She took a chance on me and supported and encouraged my studies in her laboratory. I still remember a casual conversation when she said to me, " You can be my thermal guy". I was excited and thrilled for the opportunity. Ashaki taught me the fundamentals of pristine, precise and accurate lab work. Under her discerning eye, I learned complicated analytical techniques including thermal analysis, infrared spectroscopy, and many others. I always strived to maintain the deep honor and respect, and sincere privilege I felt, of learning from such a highly respected scientist. I would not have reached this point in my education if not for Ashaki supporting me with patience, intelligence, swift guidance and friendship. Thank you, Professor!

I would like to thank my committee members, Drs. Eef Elzinga, Karina Schäfer and Dimitrios Ntarlagiannis. Dr. Schäfer provided important feedback and necessary support during the completion of this dissertation.

Dimitri was a terrific mentor, always there to share a smile or a laugh while enhancing and helping to develop my teaching skills. Eef allowed me free use of his lab and helped to develop my analytical skills particularly with deciphering complex IR and XRD signals, and I simply felt smarter after any conversation with Eef.

Special thanks to Dr. Ning Ma, who took me under his wing and provided me with key tools to build this dissertation. Ning helped me develop some fundamental ideas during thermal decomposition studies of struvite. I am thankful to my lab mate Alon Rabinovich for providing wastewater solids for use as sorbents.

Thanks to super lab tech and fellow researcher Mike Kalczynski for being there for me as a friend and making my academic life at Rutgers so much easier and pleasant, from day one. Cheers buddy!

This work would not be possible if not for my Mother, Rohenee, my first teacher, who instilled her love of spirituality, nature and books in me, my father, Krishna, who never once let me down, and my sisters, all who provided a strong foundation and home built on unconditional love.

Finally to my wife, who encouraged me from the start, who has kept my head high, belly full, and who has blessed and enriched my life immeasurably, thank you Dorota, for supporting my dreams, and for being an incredible mother to our two boys. Thank you for always believing in me.

I am proud to dedicate this work to my sons, Jax and Kai, the greatest loves I've ever known.

Table of Contents

List of Tables

List of Illustrations

Chapter 1: Introduction

1.1. *Ammonia gas in the atmosphere*

Ammonia gas ($NH_3(g)$) represents one of the largest volumes of chemicals on Earth and is continuously produced. It is a vital component of the biogeochemical nitrogen (N) cycle. Anthropogenic perturbations of the N cycle from synthesis and application of $NH_3(g)$ is of great concern and was recognized as a critical issue by the United States National Academy of Engineering (NAE), who highlighted management of the N cycle as one of the 14 Grand Challenges for Engineering in the 21st Century [Cech, 2012]. In order to be assimilated by plants and animals, N must first be fixed (transformed) into an appropriate moiety such as ammonium (NH_4^+). Input of bioavailable N to the N cycle is performed by biological fixation which reductively converts atmospheric (molecular) nitrogen gas ($N_2(g)$) to (reactive) $NH_3(g)$. However, the most important input pathway for reactive N is anthropogenic synthesis of $NH_3(g)$ which involves industrial $N_2(g)$ fixation.

Industrial generation of $NH_3(g)$ is performed by the Haber-Bosch process [Cherkasov et al., 2015] which combines hydrogen gas ($H_2(g)$) and $N_2(g)$ under elevated temperatures (400-700 °C) and pressures (80-300 atm) [Marnellos and Stoukides, 1998; Modak, 2002]. This process is highly energy intensive, consuming ~27-60 gigajoules per ton (GJ t^{-1}) NH_3 depending on region, with average global energy demands of 36.6 GJ t^{-1} NH_3 [Kool et al., 2012]. Industrial production of $NH_3(g)$ uses fossil fuels (natural gas, coal) and releases significant quantities of carbon dioxide ($CO_2(g)$) with average global emissions of 2.07 equivalent tons CO_2 per ton NH_3 [Kool et al., 2012]. China produces the largest volume

(30%) of the world's $NH_3(g)$ at an energy cost of approximately 48.8 GJ t^{-1} $NH_3(g)$ [Kool et al., 2012]. In 2010, fixed $N_2(g)$ by Haber-Bosch (120 teragrams (Tg) N yr^{-1}) was twice that of natural terrestrial sources of bioavailable N (63 Tg N yr^{-1}) [Fowler et al., 2013]. Increasing anthropogenic N fluxes represent human acceleration of the N cycle that will cause detrimental N accumulation in the environment.

A reduction in atmospheric $NH_3(g)$ is urgently needed because pollution caused by emissions of malodorous $NH_3(g)$ is a serious concern. Atmospheric $NH_3(g)$ is the principal alkaline, water-soluble molecule that participates in acid-neutralizing reactions to form ammonium (NH_4^+) salt aerosols. These NH_4^+ containing, condensation aerosols are secondary products [Battye et al., 2003], formed from parallel sequences of reactions involving primary emission products [Duffy, 2011]. A common example is the oxidation of sulfur dioxide (SO_2) to form sulfuric acid (H_2SO_4), which then reacts with $NH_3(g)$ to form a solid particle, as shown in Equations 1.1-1.4 [Duffy, 2011]:

$$SO_2(g) + OH \rightarrow HSO_3(g) \quad (1.1)$$

$$HSO_3(g) + O_2 \rightarrow SO_3 + HO_2 \quad (1.2)$$

$$SO_3 + H_2O \rightarrow H_2SO_4(g) \quad (1.3)$$

$$2NH_3(g) + H_2SO_4(g) \rightarrow (NH_4)_2SO_4(s) \quad (1.4)$$

Following formation of ammonium hydrogen sulfate, (NH_4HSO_4), and ammonium sulfate, (($(NH_4)_2SO_4(s)$) residual $NH_3(g)$ can then combine with nitric acid (HNO_3) to form ammonium nitrate (NH_4NO_3). The NH_4^+ aerosols contribute significantly to the concentration of fine particulate matter ($PM_{2.5}$) in the troposphere [Battye et al., 2003; Lonati et al., 2005]. Tropospheric aerosols alter the Earth's climate by boosting the reflectivity of clouds [Xu, 2012], thus influencing radiative forcing. Recently in China, an

increased frequency of severe haze events drew wide scientific interest due to local and global adverse impacts of NH_4^+(s) haze formation [Pan et al., 2020]. These aerosols have injurious human health effects [McCubbin et al., 2002], may lower visibility [Barthelmie et al., 1998] and promote eutrophication [Moore et al., 1995] and soil acidification [Baek et al., 2004] upon deposition. Lifetimes of NH_3(g) and NH_4^+(s) in the atmosphere range from 1-5 days, to 1-15 days respectively [Aneja et al., 2001]. The increased residence time for NH_4^+(s) indicates transport over wider distances, thus affecting wider areas as compared to NH_3(g), which is deposited closer to its source [Bouwman et al., 1997].

1.1.1. NH_3(g) Emissions Sources

The majority of NH_3(g) produced by industrial fixation of N_2(g) is used for manufacturing synthetic N-fertilizers. Increases in reactive N production and utilization in agriculture have mainly driven NH_3(g) emissions. In the United States, ~ 85% of NH_3(g) emissions are from agriculture; roughly 30 and 55% of that quantity originates from volatilized fertilizer and livestock waste respectively. Vehicular and powerplant flue gas emissions account for the remaining ~15% of total NH_3(g) emissions in the United States [Berner and Felix, 2020]. Therefore, N-losses to the atmosphere occur chiefly when NH_3(g) is volatilized from ammonium (NH_4^+(s)) in livestock waste and fertilizers. The extent of N lost from synthetic fertilizers due to volatilization of NH_3(g) depends on, but is not limited to, environmental conditions such as temperature and precipitation, soil properties and inefficient application. Using NH_3(g) emission factors, Bouwman et al., 1997 published N

content (%) lost from several fertilizers, including urea (15-25%), ammonium bicarbonate (NH_4HCO_3(s)) (20-30%), $(NH_4)_2SO_4$(s) (8%), and anhydrous NH_3 (5%).

Globally, natural and anthropogenic sources of NH_3(g) contribute 57.6 Tg N yr^{-1} with agricultural emissions, comprised of domestic animals, synthetic fertilizers and crops, totaling 37.4 Tg N yr^{-1} [Seinfeld and Spyros, 2012]. Other work has cited domesticated animal waste as the most important source of NH_3(g) to the atmosphere contributing 20 to 35 Tg N yr^{-1} globally [Bouwman et al., 1997]. To manage animal waste, aerobic composting is frequently used [Paillat et al., 2005], but this process can emit harmful quantities of NH_3(g) [Bernal et al., 2009]. In poultry housing, volatilized NH_3(g) from litter not only exacerbates N deficits but is also damaging to the health of the birds [Rothrock et al., 2013]. One study demonstrated 50-63% of excreted NH_4-N from livestock waste was lost during animal housing, manure storage and land application [Bittman and Mikkelsen, 2009]. Composted pig manure is a useful environmentally friendly fertilizer but NH_3(g) losses are also a factor limiting the efficacy of the final compost product [Wang et al., 2017]. In addition, decaying organic matter, especially under reducing conditions, can be a major contributor of NH_3(g) depending on pH [Duffy, 2011]. For example, a past work stated N-transformations occurring in deep litter compost heaps corresponded to 20-40% of N lost as NH_3(g) [Sommer and Gjedde, 2001]. Urban areas downwind from farms are especially susceptible to severe localized effects from combined agricultural and vehicular sources due to the short atmospheric residence time of NH_3(g) [Pan et al., 2020].

Overall, the NH_3(g) emissions mentioned above represent significant sustainability and environmental challenges for global N conservation. Global food production is

currently accelerating which increases utilization of N-fertilizers to meet the demand for higher crop yield [Haroon et al., 2019]. Therefore, sustainable and conservative fertilizer application combined with alternative measures to deter $NH_3(g)$ volatilization from agricultural systems is necessary to minimize environmental impacts of increasing global food production.

1.1.2. Current Abatement Techniques for Nutrient Conservation

The use of slow-release fertilizers can help improve fertilizer efficiency and minimize the negative impacts associated with N loss. For example, a study found slow pyrolyzed biochar loaded with urea exhibited slow release behavior as compared to controls [Manikandan and Subramanian, 2015]. Urea can also be applied at lower rates, low soil pH and inhibited urease activity to minimize $NH_3(g)$ emissions [Nye, 1986]. Other synthetic fertilizers such as anhydrous liquid ammonia ($NH_3(l)$) directly applied to soils at depth has been shown to help lower $NH_3(g)$ losses [Jackson and Chang, 1947]. Another sustainable and conservative fertilizer technique is using reclaimed fertilizers from farm effluents and compost. Livestock slurry is a valuable resource, but N volatilization over time lowers the effectiveness of the slurry as a sustainable fertilizer [McCrory and Hobbs, 2001]. The control of $NH_3(g)$ by amendments has been studied for broiler houses [Reece et al., 1979, Moore et al., 1996], poultry litter composting [DeLaune et al., 2004], stored poultry manure [Li et al., 2006], dairy slurry [Lefcourt and Meisinger, 2001], dairy waste compost [Liang et al., 2006], and livestock waste [McCrory and Hobbs, 2001]. A flat gas permeable membrane with an acid trap was used to capture and recover 80-100% $NH_3(g)$

emitted from poultry litter under natural and optimized (alkaline) conditions [Rothrock et al., 2013]. In another study, chemical amendments, ferric chloride and ferrous sulfate reduced NH_3(g) losses by 40-77% respectively [Moore et al., 1995]. Although chemical amendments are useful, there are serious prospective drawbacks associated with their use [Pescastore and Harter-Dennis, 1989, Moore et al., 1996]. For example, reports have shown amendments such as ferrous sulfate may affect mortality due to iron toxicity [Pescatore and Harter-Dennis, 1989]. Furthermore, it is clear some chemical treatments for NH_3(g), such as phosphoric acid amendments, are prone to harmful leaching of phosphorus (P) [Moore et al., 1996]. Therefore, there is an urgent need to develop alternative NH_3(g) mitigation techniques.

1.1.3. Sorption for mitigation

Sorbent addition could be a safer alternative to reduce emissions. The surface phenomenon of gas adsorption is defined as a discernable increase in pressure of a gas (adsorptive) close to a solid surface (adsorbent). Whereas absorption describes the interactions of an absorbent within the bulk of a material. Sorption processes occur when both adsorption and absorption occur during solid-gas interactions. Sorption processes using solids recovered from waste streams for NH_3(g) abatement could represent an energy savings, cost effective, and safer option.

Sorbents are advantageous because their use can be implemented under ambient conditions and at a lower cost as compared with other treatments [Vikrant et al., 2017]. Typical sorbents for NH_3(g) added to compost heaps have included activated carbon

[Tsutomu et al., 2004, Fortier et al., 2008], zeolite, basalt [Witter and Kirchmann, 1989] and biochars [Chen et al., 2017]. Larger scale compost facilities may use sorbents like biofilters to mitigate NH_3(g) but this technology still needs evaluation, particularly when gas concentrations are high [Smet et al., 2000]. Commonly used cation exchangers such as clinoptilolite have been used for reducing N losses [Allen et al., 1993]. Although the zeolite-sorbate complex can be applied as a slow-release fertilizer [Barbaric et al., 1990; Polat et al., 2004], without the sorbed N species, the zeolites themselves do not release additional macronutrients following deposition. Metal organic frameworks (MOFs) have been designed for capturing NH_3(g) and assessments have demonstrated remarkable uptake [Jasuja et al., 2015]. Most MOF application for agriculture however is likely limited due to toxicity issues, loss of structural integrity after reactions, and significant functionalization requirements [Vikrant et al., 2017]. Moreover, MOF production cost is high, thus operation is not sustainable as compared to waste-sourced products, such as biochars.

Biochar is appealing due to its potential for sequestering NH_3(g), for example in composting processes [Krolcyzk, 2014]. During composting of poultry manure, wheat straw biochar lowered NH_3(g) emission by 30-44% [Janczak et al., 2017]. Another study showed a wood-based biochar reduced NH_3(g) losses from ruminant urine by 45% [Taghizadeh-Toosi et al., 2012]. Though biochar application could be more suitable as compared to other types of sorbents (for example, MOF), there are some concerns regarding biochar production, including the significant energy inputs during pyrolysis which requires temperatures that may range from 400-900 °C [Day et al., 2005; Yakout and Elsherif, 2015] and concomitant emissions of harmful volatiles released during biochar

synthesis. Biochar sorption performance is highly dependent on original parent material and pyrolysis temperature [Day et al., 2005]. Moreover, activation, or significant pretreatment by heat or chemical treatment, for example by phosphoric acid addition [Ro et al., 2015], is often required, further increasing cost and application complexities of biochar utilization.

Though many sorbent treatment options exist, their use is limited due to higher expense and expertise required to use on a large scale, thus it is apparent new fundamental work is needed to assess innovative technologies for N conservation. Recent scientific attention has been directed towards mitigation methods that solve emissions problems but are also economically feasible and practical to farmers [McCrory and Hobbs, 2001]. Hence, safer, ecofriendly techniques for conserving N should be explored, of which sorption mediated control, is very promising. Thus, there is a demand for the development and evaluation of low-cost sorbents to be utilized as additives in agriculture for sequestering $NH_3(g)$.

1.2. Struvite Nitrogen Sequestration and Release

Struvite, ($MgNH_4PO_4 \cdot 6H_2O$), has long been recognized as a valuable, low-cost wastewater resource with excellent potential for supporting sustainable agriculture [Etter et al., 2011] and nutrient management [Taddeo et al., 2018]. The economic and environmental advantages of using struvite recovered from wastewaters for use as fertilizer has been published [de Vries et al., 2016]. As urban density increases, more wastewater volume is produced so problems associated with nutrient discharge limits need to be

addressed [Wei et al., 2003]. By identifying wastewater as a renewable resource, wastewater streams rich in P and N are an ideal source for recovery and repurposing of these macronutrients.

Struvite is a mineral that has been proposed as a sustainable, replacement for P reserved in rocks because struvite precipitated in waste effluents can simultaneously recover and recycle P and N [Booker et al., 1999], and subsequently be applied as a slow-release fertilizer [Rouff, 2012, Rouff et al., 2016]. Though the primary focus is on P recovery, intentional precipitation of struvite has been shown to also reduce N losses. For example, a past work reported N losses during composting were considerably lowered by struvite crystallization, incorporating N in struvite's crystal structure [Jeong and Kim, 2001]. Thus, by producing struvite-containing compost, additional nutrients such as P are also supplied, further increasing the agronomic value of the final product when compared to normal compost [Jeong and Kim, 2001]. In a different study, N loss during pig manure and cornstalk composting was reduced from 35% down to almost 1% due to struvite precipitation [Ren et al., 2009]. Besides composting, other systems such as industrial and agricultural waste streams have tremendous potential for N recovery by intentional struvite precipitation [Diwani et al., 2017; Kim et al., 2007].

Since surplus struvite is spontaneously precipitated in wastewater systems under favorable conditions, and is readily available, further uses besides application as fertilizer should be explored. The use and reuse of struvite and its decomposition products for the recovery of NH_4^+(aq) in aqueous systems such as landfill leachate [Li and Zhao, 2003; He et al., 2007; Zhang et al., 2009] and waste waters [Sugiyama et al., 2005] were shown to be effective. When subjected to elevated temperatures, structural NH_4^+(s) is volatilized

from struvite, and the percentage removed from the mineral depends on the temperature [Sugiyama et al., 2005]. Previous work used heat-treated struvite products as adsorbents for removal of NH_4^+(aq) from a 100 mL solution containing 8.15 mmol NH_4^+ as NH_4Cl and reported removal rates for $MgHPO_4$ (49%) > $Mg_3(PO_4)_2$ (34%) > $Mg_2P_2O_7$ (0%) after 1 h [Sugiyama et al., 2005]. Heat-treated struvite may also be used as an adsorbent for NH_3(g). The use of adsorbents for NH_3(g), derived from struvite heat treated at 105 °C have shown loadings of 2.56 mol–N kg^{-1} adsorbent with related enthalpy of adsorption of -3.0 kJ mol^{-1} [Fumoto et al., 2009]. By comparison, studies done using zeolites recorded 0.8 mol–N kg^{-1}-zeolite [Bernal and Lopez-Real, 1993]. Based on these results, the efficiency of struvite-related sorbents for NH_3(g) should be evaluated. Though struvite's own contribution to NH_3(g) emissions have not been extensively reported, struvite can release NH_4^+(s) completely or partially, depending on time and temperature of thermal treatment [Sarkar, 1991; Ma et al., 2014]. Thus, struvite can be both source and sink for N.

1.2.1. NH_3(g) Sequestration by Sustainable Struvite Sorbents

Sorbing NH_3(g) onto struvite, and its heated decomposition products may reduce associated malodors and mitigate some of the N-loss in compost heaps, thus increasing productivity and augmenting the fertilizer potential of the compost. Mitigation of nutrient loss by compost or commercial fertilizer (e.g. urea) amelioration could be especially useful in agricultural areas where N-retention capacity is a concern. For example, calcareous and sandy soils such as those found in Florida's citrus growing locations have high potential for nutrient loss [He et al., 2002] and benefit from fertilizer additives for N conservation.

Lowering N losses in agricultural systems by mitigating $NH_3(g)$ emissions is economically and ecologically advantageous and requires innovative, sustainable approaches for optimizing synthetic [Nye, 1986] and alternative fertilizers [Rothrock et al., 2013; Rouff and Juarez, 2014]. Furthermore, repurposing of agricultural wastes, for example by reclaiming nutrients from effluents, may offer benefits to the farmer with regard to financial and carbon credits.

1.2.2. Thermal Analysis and Role in Evaluating Sorption

Surface properties that facilitate sorption, for example porosity, acidity, and functional groups vary drastically between different types of sorbents. Some drawbacks include necessary functionalizing or tailoring sorbents for specific sorbates which is time consuming, requires expertise, and is uneconomical. In order to develop and evaluate sorbents quickly and efficiently, novel techniques are needed. Common practice to determine sorption capacity, concomitant sorption enthalpy and desorption typically need multiple experimental apparatus. However, other studies [Eigenmann et al., 2000] demonstrated that it was feasible to describe all these sorption-desorption phenomena using a single experimental setup: simultaneous thermal analysis-pulse thermal analysis STA-PTA. STA has been well established as a method for describing thermal properties of many types of materials and reactions.

The thermal stability and decomposition of struvite has been elucidated by thermal analysis [Frost, 2004; Rouff 2016]. Thermal analysis relates mass changes to time or temperature. Important parameters such as temperature of decomposition (85 °C) and mass

loss steps correlated to stoichiometry were reported for struvite [Frost, 2004]. Heat flow during TG decomposition indicated the reaction is endothermic as monitored simultaneously by differential scanning calorimetry (DSC). The endothermic peak for struvite was found to be 126 °C and the integrated area under the peak gives the enthalpy of decomposition [Rouff 2011]. However, thermal properties of struvite decomposition such as onset temperature, and endothermic transitions can change depending on the background solutions from which the mineral is recovered [Rouff et al., 2016; Rabinovich et al., 2018]. Therefore, thorough characterization of the thermal behavior of struvite is important [Rouff et al., 2016]. Therefore, it is relevant to perform thermal analyses (chapter 2) to investigate the environmental impact of structural NH_4^+(s) evolved from struvite. Furthermore, struvite's potential to act as a sorbent for NH_4^+(aq) needs evaluating since increasing the N-load of the mineral via sorption processes would increase the volatile content as well.

The hyphenated STA-PTA method is a novel approach for describing sorption-desorption processes. The technique in this dissertation involves an STA-PTA setup and Fourier transform infrared spectrometer for evolved gas analysis (STA-PTA-FTIR), where a known quantity of adsorptive is pulsed into the carrier gas stream (Figure 1.1). This method has other advantages which includes: dynamic flow which is more convenient than static procedures requiring vacuum conditions, observing sorption phenomena under ambient conditions (25 °C, 1atm) unlike volumetric procedures, and temperature selection which is important when studying sorption reactions since high and low temperatures speed up or slow down the time need to achieve thermodynamic equilibrium between sorbent and sorbate. The STA-PTA technique was shown to be reliable by comparing datasets to other

related data in previous work [Eigenmann et al., 2000]. Finally, employing kinetics software to treat mass and heat flow changes can provide determinations of kinetic parameters including activation energy, rate of reaction and preexponential factors.

1.3. Objectives

This dissertation addresses problems associated with NH_3(g) emissions from agriculture to the atmosphere by providing fundamental information on a sustainable approach for minimizing N losses. The focus of this dissertation is evaluation of low-cost, non-conventional sorbents for NH_3(g) suitable for agricultural systems. The underlying aim of this study was to :

1. Identify thermal decomposition products of struvite heated to 55-300 °C, (chapter 2),
2. Evaluate the potential of struvite and its thermal decomposition products as alternative sorbents for NH_3(g) as performed by simultaneous thermal analysis-pulse thermal analysis (STA-PTA) (chapter 3),
3. Demonstrate the validity and value of STA-PTA as an economically feasible, fast, reliable, accurate and precise method for evaluating gas sorption-desorption (chapters 3, 4),
4. Determine efficacy of sorbents derived from livestock waste for NH_3(g) capture, in comparison with conventional sorbents including biochar and metal organic frameworks. (chapters 3, 4),
5. Establish simple kinetic models to describe gas sorption-desorption (chapter 4).

This work was performed using a novel technique optimized to conduct sorption tests quickly, for a range of sorbents to provide multiple relevant data sets with high precision and accuracy. The main findings and conclusions provide insight and fundamental information that allow for more complete understanding of NH_3(g)-solid interactions under ambient conditions. Facile evaluations to quantify the capacity of sorbents demonstrated that potential exists to develop practical, cost-effective sorbents from wastes.

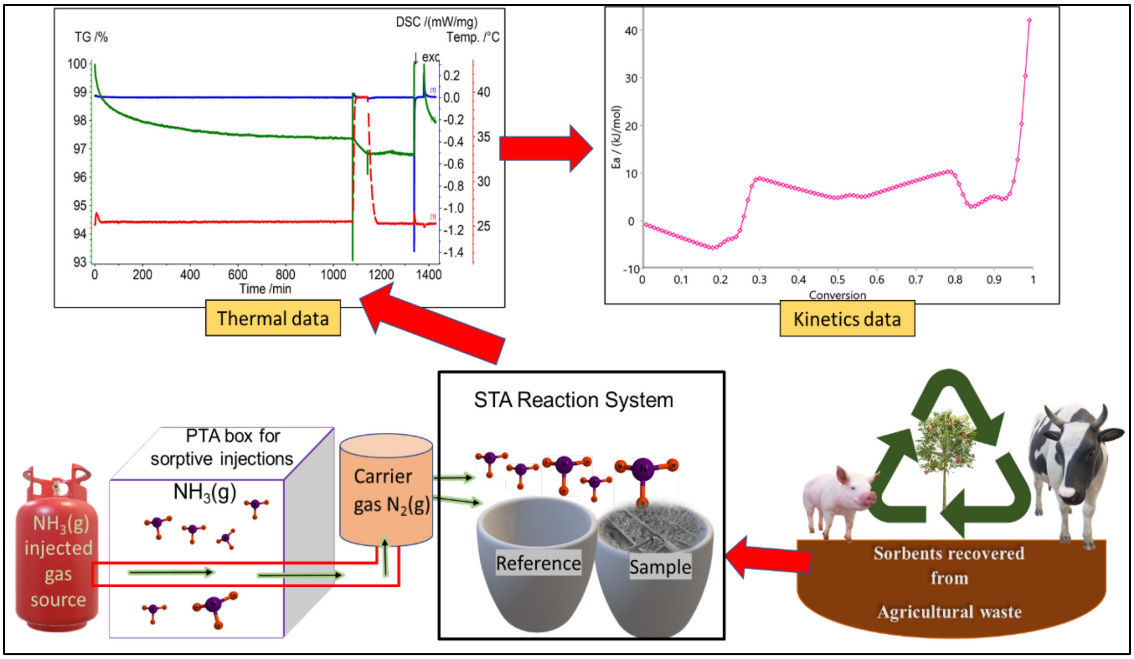

Figure 1.1. The complete STA-PTA-FTIR technique. Sorbents are recovered from sustainable parent materials. Pulses of $NH_3(g)$ are carried into the STA system with inert $N_2(g)$ and reacted with sample-filled pan. Mass and heat flow data are measured simultaneously against an empty reference pan. Collected STA data is subsequently analyzed for thermal and kinetic information.

Chapter 2: An Investigation of the Thermal Behavior of Magnesium Ammonium Phosphate Hexahydrate[1]

Abstract

Struvite ($MgNH_4PO_4 \cdot 6H_2O$) was heated to temperatures from 55-300 °C. X-ray diffraction (XRD) analysis revealed struvite was stable at 55 °C, partially decomposed to dittmarite ($MgNH_4PO_4 \cdot H_2O$) at 100-200 °C, and formed an amorphous phase at 250-300 °C. Thermogravimetric analysis (TG) confirmed sample mass loss consistent with dittmarite formation at 100-200 °C and evolution of all volatiles at 250-300 °C. Fourier transform infrared (FTIR) spectroscopy detected the ν_4 NH_4^+ band in 55-200 °C solids, as expected for struvite and dittmarite. This band decreased in intensity at 250 °C, and was not evident at 300 °C, confirming loss of NH_4^+(s) at these temperatures. FTIR spectra also showed changes in the vibrations of the ν_3 PO_4^{3-} band. At 55 °C splitting in the band indicated destabilization of the PO_4^{3-}(s) group despite no change in mineralogy. Vibrations at 100-200 °C were associated with dittmarite and $MgHPO_4$, and at 250-300 °C, $MgHPO_4$ and $Mg_2P_2O_7$. Analysis of acid-digested solids indicated the presence of P other than P-PO_4 at 200-250 °C, confirming $Mg_2P_2O_7$ formation. Overall, heat treatment of struvite produces several decomposition products, complete identification of which requires the use of

[1] This chapter is published as: Ramlogan, M.V., Rouff, A.A., 2016. An investigation of the thermal behavior of magnesium ammonium phosphate hexahydrate. J. Therm. Anal. Calorim. 123(1), 145-152.

multiple approaches. Temperature-induced phase transformations along with emission of $NH_3(g)$ has implications for use of struvite in multiple applications.

2.1. Introduction

Recovery of nitrogen (N) and phosphorous (P) from wastewater treatment facilities and agricultural runoff prior to their deposition into natural waters is important both from conservation and environmental health impact standpoints. Phosphorus is extensively mined from phosphate bearing rocks for use in fertilizer and due to an ever increasing demand, this non-renewable supply of P is projected to be severely depleted within the next 50-100 years [Cordell et al., 2009]. It is widely accepted there lacks another substantial source of P for use in agriculture, similar to phosphate reserved in rocks. As a result, focus has been directed at sustainable recovery and repurposing of phosphates [Bezbaruah and Almeebi, 2014]. In addition to alleviating the demand for P, recovery of P from wastewater helps abate the possibility of eutrophication [Paerl and Huisman, 2009]. Also present in wastewater designated for release back into the environment, N species such as $NH_4^+(aq)$ contribute to the superfluity of N in natural waters leading to increased eutrophication [Smith et al., 1991]. Where equimolar amounts of $Mg^{2+}(aq)$, $NH_4^+(aq)$, and $PO_4^{3-}(aq)$ exist, struvite ($MgNH_4PO_4 \cdot 6H_2O$, MAP) is a mineral which precipitates according to Equation (2.1) [Liu et al., 2011]:

$$Mg^{2+}(aq) + NH_4^+(aq) + H_2PO_4^-(aq) + 6H_2O \rightarrow MgNH_4PO_4 \cdot 6H_2O + 2H^+ \quad (2.1)$$

Sludge produced by wastewater treatment plants is often treated at high temperatures [Bhuiyan et al. 2008; Neyens and Baeyens, 2003], therefore it is pertinent to

examine the behavior of struvite upon heating. Temperature may also affect the solubility and sorption behavior of pollutants in wastewater sludge. For example, sorbed chromium (Cr) affects the thermal stability of struvite [Rouff, 2012], and removal in struvite saturated solutions was increased with temperature up to 300 °C [Rouff, 2013]. Thermal behavior of struvite should also be considered during other applications, for example in magnesium phosphate cement (MPC). Struvite is a significant reaction product during MPC synthesis [Mestres and Ginebra, 2011]. MPC has been used in civil engineering for rapid fixes due to its quick setting properties [Mestres and Ginebra, 2011] and has been shown to play a role in biomedical application, specifically for endodontic hard tissue repair [Mesres et al., 2014]. One of the problems that has been identified with MPC storage and handling is ammonia release causing corrosion of storage facilities and potentially increasing ammonia pollution in the environment [Mestres and Ginebra, 2011; Michalowski and Pietryzk, 2006]. Ammonia or ammonium ion evolution from struvite is enhanced upon heating to temperatures higher than 55°C [Sarkar, 1991], but has also been shown to occur at room temperature when brought into contact with CO_2–containing water [Sarkar, 1991].

The solid decomposition products of struvite are related to the conditions under which the decomposition process occurs [Frost, 2004]. Whitaker, 1968, stated struvite decomposed subaerially to newberyite ($MgHPO_4 \cdot 3H_2O$) at 20 °C. Kurtulus and Tas, 2011, reported obtaining an amorphous phase on heating crystalline struvite powders in air at 200 °C. Bhuiyan and Koch, 2008, reported struvite decomposition was dependent on the heating rate by thermogravimetric analysis (TG), and that boiling in excess water completely transformed struvite to dittmarite ($MgNH_4PO_4 \cdot 6H_2O$). The present work seeks to further investigate decomposition of struvite when it is subjected to specific

temperatures by examining furnace treated struvite samples using x-ray diffraction (XRD), Fourier transform infrared spectroscopy (FTIR), ultra violet visible spectroscopy (UV-VIS) and inductively coupled plasma-optical emission spectroscopy (ICP-OES). TG was used to provide data on mass loss and volatile release to further understand the decomposition process.

2.2. Materials and Methods

Masses of 500 mg of commercial struvite (Alfa Aesar 99%) were added to 10 mL glass beakers and were heated from room temperature to final temperatures of 55, 100, 150, 200, 250 and 300 °C for 22 h in a Fisher Scientific Isotemp Muffle Furnace. Six different final temperatures were chosen to determine possible phase changes as a function of heating. Samples recovered from the furnace were allowed to cool to room temperature in a Fisher Scientific desiccator prior to additional analysis.

2.2.1. X-ray Diffraction

A sample of unheated commercial struvite (Alfa Aesar 99%) placed on a glass microscope slide and fixed with acetone was prepared for XRD analysis using a Phillips X'pert Pro instrument. An XRD pattern was obtained from this unheated sample, and used as a standard struvite pattern for comparison with heated samples. All heated samples recovered from the furnace were similarly fixed to slides and analyzed using XRD. Data were collected over a range of 5-60° 2θ with a 0.01 step size, 1 s per step, for a total time

of 5500 s. X'pert High Score software was used in a comparative matching procedure to interpret the peaks of heated samples.

2.2.2. Thermogravimetric Analysis

Struvite (Alfa Aesar 98%) samples each weighing approximately 22-32 mg, placed in an open ceramic crucible, were subjected to TG using a PerkinElmer STA 6000. Dry Nitrogen gas (N_2) was used as a sample purge with a flow rate of 20 mL min^{-1}. Samples were heated from 25 °C at a rate of 30 °C min^{-1} to a final sample temperature of 55, 100, 150, 200, 250 or 300 °C. The time to final temperature ranged from 1-9.2 min. Once at temperature, the samples were held isothermally for 1 h prior to cool down.

2.2.3. Fourier Transform Infrared Spectroscopy

A Perkin Elmer Spectrum 100 instrument with a universal attenuated total reflectance (UATR) accessory was used to collect FTIR data for unheated struvite and samples recovered from the furnace. The FTIR spectra were recorded in the region from 650 to 4000 cm^{-1} with a resolution of 4 cm^{-1}. The calculated average of 20 scans was used as a final result per sample.

2.2.4. Compositional Analysis

Unheated struvite and samples recovered from the furnace were analyzed to determine the composition. Solids were weighed, transferred to 15 mL tubes and acid digested in 2 mL of 2% HNO_3 for 24 h followed by dilution with 8 mL of deionized (DI) water. A further 1:100 dilution was carried out for all samples. A HACH 3900 spectrophotometer was used for analysis of $P\text{-}PO_4$ by the ascorbic acid method at a wavelength of 880 nm, and for $N\text{-}NH_3$ by the salicylate method at a wavelength of 694 nm. A Perkin Elmer Optima DV5300 ICP-OES was used to obtain elemental Mg concentrations of the solids. Results were converted from mg L^{-1} to mol kg^{-1} of solid and compared to calculated values for struvite and other phases of interest.

2.3. Results and Discussion

2.3.1. X-Ray Diffraction

The XRD patterns for unheated struvite and the heated solids are plotted in Figure 1, as well as ideal XRD patterns obtained from the American Mineralogist Crystal Structure Database (AMCSD) for struvite and dittmarite. Results confirmed struvite was the dominant phase in the sample heated at 55 °C. This indicated the struvite crystal structure remained intact at 55 °C even after 22 h of heat treatment, and the sample was stable at this temperature. However, at temperatures higher than 55 °C, changes in the crystal structure were observed. For the 100, 150 and 200 °C samples, increase in intensity of the peaks at 10.1°, 18.7°, 21.1° and 31.8° 2θ, and diminishing of the peaks at 10.0°, 21.0°, and at 30.8-33.9° 2θ, indicated the presence of dittmarite. Thus, the decomposition

products for samples heated from 100-200 °C contained a mixture of phases as a result of evolution of $H_2O(s)$ upon heating and formation of dittmarite:

$$MgNH_4PO_4 \cdot 6H_2O(s) \rightarrow MgNH_4PO_4 \cdot H_2O(s) + 5H_2O(g)\uparrow \quad (2.2)$$

No peaks were detected in the XRD patterns for samples heated at 250 and 300 °C. Instead, broad XRD patterns for these two solids were found to closely match the glass slide background pattern, indicating amorphization occurred at these temperatures.

2.3.2. Thermogravimetric Analysis

The mass loss with time, and the mass percentage remaining in samples heated under isothermal conditions at 55-300 °C using the TG method is plotted in Figure 2.2. The rate of mass loss increased with temperature (Figure 2.2a). At 55 °C slow mass loss occurred over the entire 60 min, whereas at 100 °C mass loss was more rapid, stabilizing after ~40 min. At higher temperatures mass loss stabilized after ~15 min. The percentage mass loss also increased as temperature increased (Figure 2.2b). The 0.99% mass loss at 55 °C could be due to release of adsorbed water from the surface of the crystalline powder sample, while the 44.96% mass loss recorded at 100 °C was attributed to struvite decomposition to the monohydrate dittmarite due to release of $H_2O(s)$. This interpretation is in agreement with previous studies that proposed thermal decomposition of struvite to dittmarite in air occurred at 103 °C [Abdelrazig and Sharp, 1988] (Equation 2.2). At 250-300 °C the total mass loss at 51.89-52.62% is close to the calculated percentage of $NH_4^+(s)$ and $H_2O(s)$ in unheated struvite at 51.4%. Therefore, the observed mass loss indicated complete loss of volatiles from the struvite structure, which may correspond to the reaction:

$$MgNH_4PO_4 \cdot 6H_2O(s) \rightarrow MgHPO_4(s) + NH_3(g) \uparrow + 6H_2O(g) \uparrow \quad (2.3)$$

This newly formed phase is amorphous based on the XRD pattern. The temperature of decomposition for struvite has been reported to be 125 °C [Paul et al., 2002], therefore overall mass loss was attributed to volatile release of $H_2O(g)$ and $NH_3(g)$ upon heating in the 100-300 °C range.

2.3.3. Fourier Transform Infrared Spectroscopy

The FTIR spectra of unheated struvite and samples recovered from the furnace are shown in Figure 2.3. The vibrations in the region of the NH_4^+ ν_4 asymmetric and the ν_3 antisymmetric band of PO_4^{3-} provide further insight into the impact of temperature on the decomposition products of struvite. The bands centered at 1471 cm^{-1} and 1430 cm^{-1} in the unheated struvite sample are attributed to NH_4^+ ν_4 asymmetric bending. These bands were observed in samples heated from 55 to 200 °C. Therefore, $NH_4^+(s)$ is present in these samples, consistent with struvite at 55 °C and the formation of dittmarite at higher temperature. At 200 °C the peaks decreased in intensity and broadened, indicating the presence of an additional phase with no structural $NH_4^+(s)$. This phase is likely amorphous as dittmarite is the only additional phase detected by XRD. At 250 and 300 °C the peaks associated with the NH_4^+ ν_4 asymmetric bending disappeared, confirming no detectable $NH_4^+(s)$ in the solid. This is in line with the observed mass loss by TG, which indicates loss of all volatiles, and thus also $NH_4^+(s)$ at these temperatures.

The ν_3 antisymmetric stretching vibration of PO_4^{3-} is located in the band centered at 1000 cm^{-1}. For unheated struvite, the highest intensity bands due to P-O ν_3 and ν_1

stretching vibrations were found in the region between peaks at 1017 cm^{-1} and 951 cm^{-1}. In samples up to 200 °C, the weak peak at 951 cm^{-1} was assigned to the ν_1 P-O stretch [Soptrajanov et al., 2002]. The sample treated at 55 °C exhibited substantial splitting in the P-O ν_3 band resulting in two peaks at 1063 cm^{-1} and 983 cm^{-1} with the peak at 1063 cm^{-1} having a lower intensity than the one at 983 cm^{-1}. Published FTIR spectra of dittmarite cite maxima for the ν_3 PO_4 modes at 1063 cm^{-1} and 978 cm^{-1} [Soptrajanov et al., 2002]. However, the XRD pattern of the 55 °C sample was consistent with that of unheated struvite, indicating no discernable change in mineralogy. Assuming no change in crystal structure, splitting in the P-O ν_3 band does indicate an increase in disorder at the phosphate site as a result of application of heat to the mineral structure. This may be due to increased vibrational energy with heat addition. Furthermore, the loss of adsorbed water, as suggested by TG results, could increase the disorder in near-surface phosphate groups by breaking stabilizing surface bonds. Perturbations to phosphate groups at the mineral surface can in turn translate to bulk disorder, an effect observed when inner-sphere adsorbates form at the mineral surface [Rouff and Juarez, 2014]. The overall impact appears to be rearrangement of PO_4^{3-}(s) within the struvite crystal structure, which is likely precursory to the transition to dittmarite. Furthermore, the formation of a small amount of dittmarite, below the detection of XRD, cannot be ruled out for this sample. Samples heated to 100, 150 and 200 °C also exhibited well defined splitting of the P-O ν_3 band. For these samples, the peak at 1063 cm^{-1} increased in intensity, and became more dominant relative to the peak at 983 cm^{-1}. This is consistent with the transition from struvite to dittmarite in these samples, as confirmed by XRD. At 200 °C, the peaks within this band became less defined with weaker intensities, indicating a decrease in the contribution of dittmarite to the sample. As

dittmarite is the only decomposition product detected by XRD, and peaks in this region broaden, this is indicative of the formation of an amorphous phase in the sample. At 250 °C and 300 °C the peaks at 1063 cm^{-1} and 983 cm^{-1} disappeared, likely due to significant broadening, with formation of broad peaks centered at 929 cm^{-1} and 1105 cm^{-1}. This indicated a further change in the composition of these samples and complete loss of crystallinity, and thus dominance of an amorphous phase. Since δ(POH) vibrational bands of HPO_4^{2-} are detected between 1160 cm^{-1} and 900 cm^{-1} [Boonchom, 2009; Frost et al., 2005], a potential decomposition product is $MgHPO_4$, as indicated above (Equation 2.3). Though direct formation of $MgHPO_4$ from struvite is possible, dittmarite dominates the 100-150 °C samples. Thus at 200-300 °C formation of amorphous $MgHPO_4$ would proceed as a direct decomposition product of dittmarite:

$$MgNH_4PO_4 \cdot H_2O\,(s) \rightarrow MgHPO_4\,(s) + NH_3\,(g)\uparrow + H_2O\,(g)\uparrow \quad (2.4)$$

The peaks at 929 cm^{-1} and 1105 cm^{-1} and the broadening in this region of the FTIR spectrum is also observed for formation of $Mg_2P_2O_7$ [Boonchom, 2009; Umbreit and Paukszta, 2009]. At temperatures > 250 °C formation of amorphous $Mg_2P_2O_7$ may occur by decomposition from $MgHPO_4$(s) or decomposition of dittmarite by the reactions:

$$2MgHPO_4(s) \rightarrow Mg_2P_2O_7(s) + H_2O(g)\uparrow \quad (2.5)$$

$$2MgNH_4PO_4 \cdot H_2O(s) \rightarrow Mg_2P_2O_7(s) + 2NH_3(g)\uparrow + 3H_2O(g)\uparrow \quad (2.6)$$

2.3.4. Compositional Analysis of Solids

The UV-Vis P-PO_4 and N-NH_3 data and ICP-OES Mg data were converted from mg L^{-1} to mol kg^{-1} solid P, N and Mg (Table 2.1). The NH_4^+(s) content of the samples

decreased over the temperature range. As all NH_4^+(s) is either associated with struvite or dittmarite, a slight decrease in the NH_4^+(s) content of 100-200 °C samples suggests the presence of some amorphous $MgHPO_4$ at these temperatures. This is not evident based solely on the XRD patterns for the 100-200 °C samples, or the FTIR results for the 100 and 150 °C samples. However, these results confirm the presence of $MgHPO_4$ in the 200 °C sample, as alluded to by the FTIR results which show decreased intensity of the NH_4^+ ν_4 band and broadening of the ν_3 PO_4^{3-} band. For samples heated up to 200 °C this also suggests that a small fraction of the mass loss at these temperatures by TG is due to evolution of NH_3(g) and not H_2O(g) alone. In the 250 and 300 °C samples, the measured NH_4^+(s) concentrations are close to the error on the measurement, indicating little to no NH_4^+(s) in these solids, consistent with the presence of $MgHPO_4$. This interpretation is supported by total loss of volatiles from the sample by TG and the disappearance of the NH_4^+ ν_4 band in the FTIR spectra. The Mg:P ratios for the solids were compared to calculated values for all potential phases in the sample. The Mg:P ratios were approximately 1:1 for temperatures from 55-200 °C indicating no change in this ratio relative to struvite with heat treatment. At 55 °C, the absolute molar concentrations of Mg and P are the same as those measured for unheated struvite and the calculated concentrations for struvite. From 100-200 °C the Mg and P concentrations are slightly higher and approach that for dittmarite, indicating the presence of both struvite and dittmarite in the samples. Considering the presence of an amorphous NH_4^+(s)-free phase in these samples, the dittmarite content is calculated to range from ~80% to 40% in these samples. At 250-300 °C the Mg concentrations are closer to those for $MgHPO_4$ and $Mg_2P_2O_7$. The lower P concentration and thus high Mg:P ratio is indicative of the presence

of P speciated other than P-PO_4 as measured by UV-Vis. Thus speciation of P as $P_2O_7^{4-}$(s) could account for this discrepancy. This confirms the presence of $Mg_2P_2O_7$ in these samples at ~40 to 50 % of the sample composition.

2.4. Conclusion

This study utilized solid and aqueous spectroscopic methods to explore the thermal decomposition of struvite. The decomposition products are contingent upon temperature, and detection of these products depends on the implemented technique (Table 2.2). Structural changes in furnace treated struvite samples observed with XRD can be correlated with TG mass loss as well as shifting in the FTIR bands associated with PO_4^{3-}(s) and NH_4^+(s). Dittmarite was the primary crystalline phase derived from struvite heated to 100, 150 and 200 °C. The loss of dittmarite peaks in the diffraction patterns at 250 and 300 °C in our results were consistent with Abdelrazig and Sharp, 1988, who reported dittmarite decomposed between 200 and 300 °C. Disappearance of NH_4^+(s) bands at temperatures higher than 200 °C is in agreement with previous findings that NH_4^+(s) is released from the struvite structure above 200 °C [Ma et al., 2014]. However analysis by UV-Vis indicated NH_4^+(s) was partially released as NH_3(g) at lower temperature, in 100-200 °C samples. Loss of NH_4^+(s) and loss of crystallinity indicated the formation of amorphous $MgHPO_4$, which in turn decomposed to form $Mg_2P_2O_7$ confirmed by FTIR and P-PO_4 analysis. The overall decomposition products from 25-300 °C, and the stable temperatures of products observed within this range are summarized in Figure 2.4.

The thermal behavior of struvite reported in this study has important implications for agricultural and engineering processes. By precipitating struvite in compost heaps, nutrients such as P and N can be sequestered, preventing losses via leaching, or volatilization [Jeong and Kim, 2001]. Struvite has great potential as a slow-release fertilizer that may lower high production costs and pollution associated with inefficient use of fertilizers [Yetilmezsoy and Sapci-Zengin, 2009]. In addition to agriculture, struvite decomposition may be relevant to other industries such as biomedical and civil engineering. Historically, biocements have been synthesized with calcium phosphate cements for bone tissue repair, but magnesium phosphate cements are now generating interest [Vorndran et al.; Moeske et al., 2011]. MPC's containing struvite as the binding phase is a promising novel application where fast setting cements are needed for civil engineering repairs [Chau et al., 2011; Zhang et al., 2013]. Of note is that struvite undergoes structural changes even at 55 °C, despite no change in mineralogy. Since struvite decomposition results in release of NH_3(g) at temperatures > 100 °C, further studies are needed to quantify the evolution of gases from the mineral. Thus, thermal stability of struvite should be considered, particularly during the mineral's application, storage and transport.

Acknowledgements

Support was provided by the National Science Foundation Grant No. EAR-1506653. The authors thank Ning Ma for assistance with sample preparation and analysis.

Tables and Figures

Table 2.1 UV-Vis and ICP-OES data for unheated and heat-treated samples. Data was converted from mg L^{-1} and reported in mol kg^{-1} of solid.

		Moles per kg Solid			
	Sample/Phase	[a]Mg	[b]P	[c]NH_4^+	Mg:P
Measured	Unheated MAP	4.5	4.6	3.5	1.0
	55 °C	4.5	4.4	3.9	1.0
	100 °C	5.4	5.2	2.3	1.0
	150 °C	5.2	5.4	2.8	1.0
	200 °C	5.6	5.7	1.5	1.0
	250 °C	9.8	6.1	0.7	1.6
	300 °C	10.2	4.8	0.4	2.1
Calculated	Struvite	4.1	4.1	4.1	1.0
	Dittmarite	6.4	6.4	6.4	1.0
	$MgHPO_4$	8.3	8.3		1.0
	$Mg_2P_2O_7$	9.0	9.0		1.0

[a]Mg error ± 0.3 mol kg^{-1}
[b]P error ± 0.4 mol kg^{-1}
[c]NH_4^+ error ± 0.4 mol kg^{-1}

Table 2.2 Thermal decomposition products as identified using implemented techniques for samples heated from 55-300°C. Total detected phases and estimated relative proportions are also reported.

Temperature	XRD	TG	FTIR	ICP-OES/UV-Vis	Total Phases
55 °C	Struvite	Struvite	Struvite Dittmarite*	Struvite	Struvite > Dittmarite*
100 °C	Dittmarite	Dittmarite	Dittmarite	$MgHPO_4$	Dittmarite > $MgHPO_4$
150 °C	Dittmarite	Dittmarite	Dittmarite	$MgHPO_4$	Dittmarite > $MgHPO_4$
200 °C	Dittmarite	Dittmarite	Dittmarite $MgHPO_4$	Dittmarite $MgHPO_4$	$MgHPO_4$ > Dittmarite
250 °C		$MgHPO_4$	$MgHPO_4$ $Mg_2P_2O_7$	$MgHPO_4$ $Mg_2P_2O_7$	$MgHPO_4$ > $Mg_2P_2O_7$
300 °C		$MgHPO_4$	$MgHPO_4$ $Mg_2P_2O_7$	$MgHPO_4$ $Mg_2P_2O_7$	$Mg_2P_2O_7$ > $MgHPO_4$

*Dittmarite-like phosphate vibrations detected.

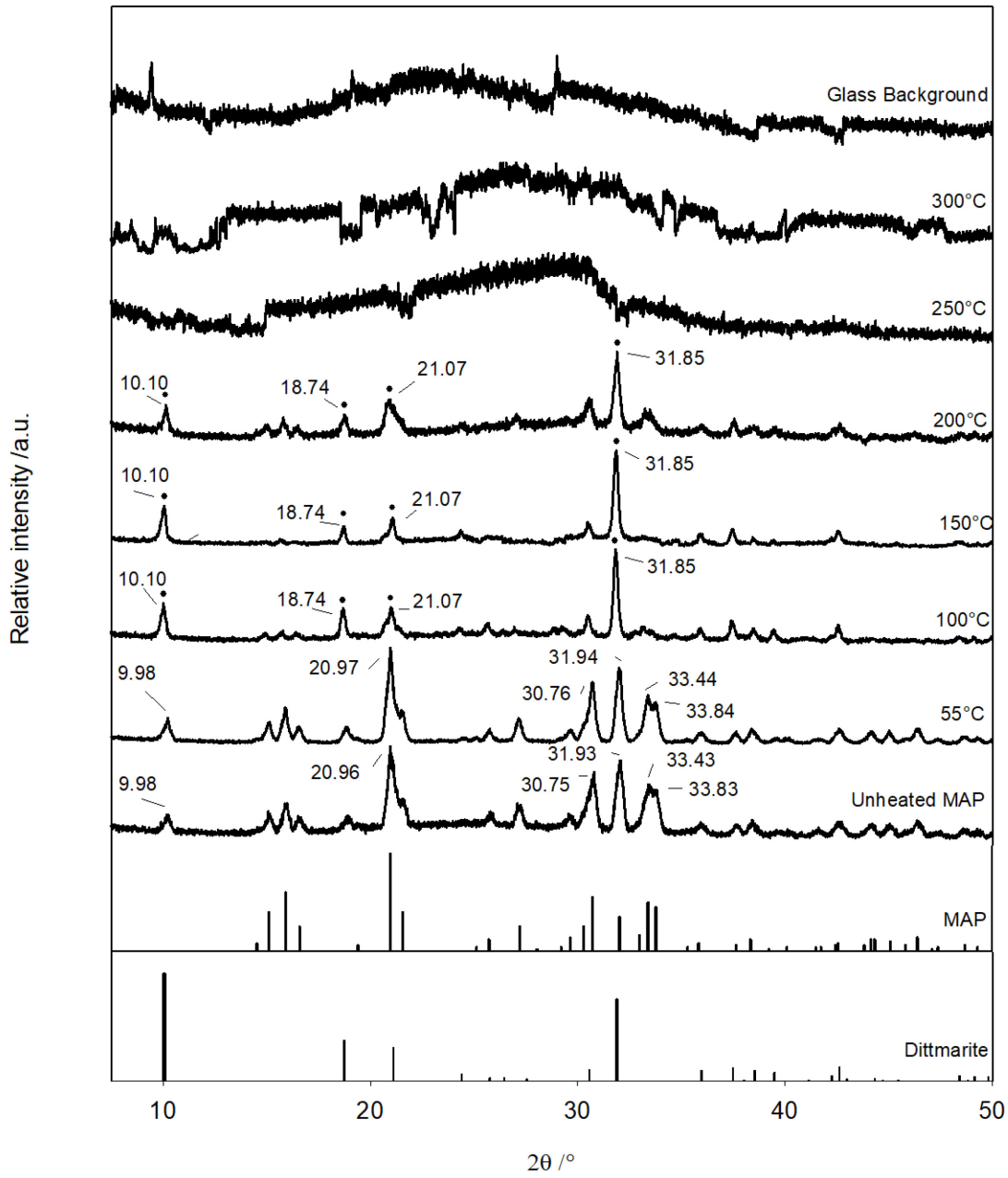

Fig. 2.1 XRD spectra of unheated struvite (MAP) and furnace treated samples. Glass slide background is also shown. The diamond (◆) identifies dittmarite peaks which are dominant in three samples.

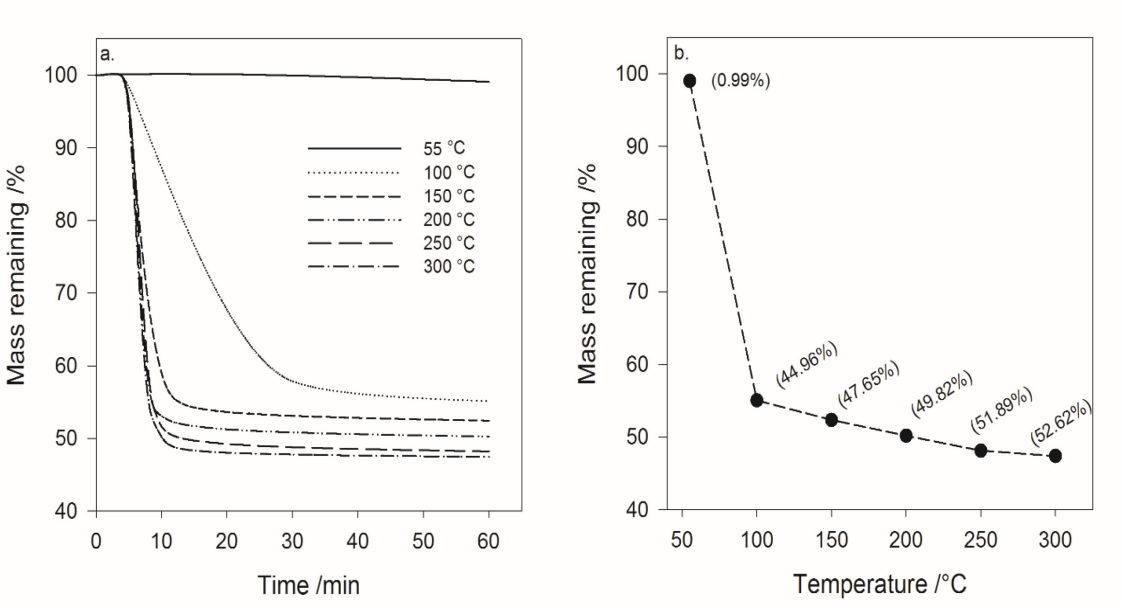

Fig. 2.2 Results from 60 min isothermal TG scans at 55-300 °C. a) Mass loss curves reported as mass percentage solid remaining as a function of time; and b) the mass percentage solid remaining at the 60 min end point at each temperature, with the percentage mass loss indicated in brackets.

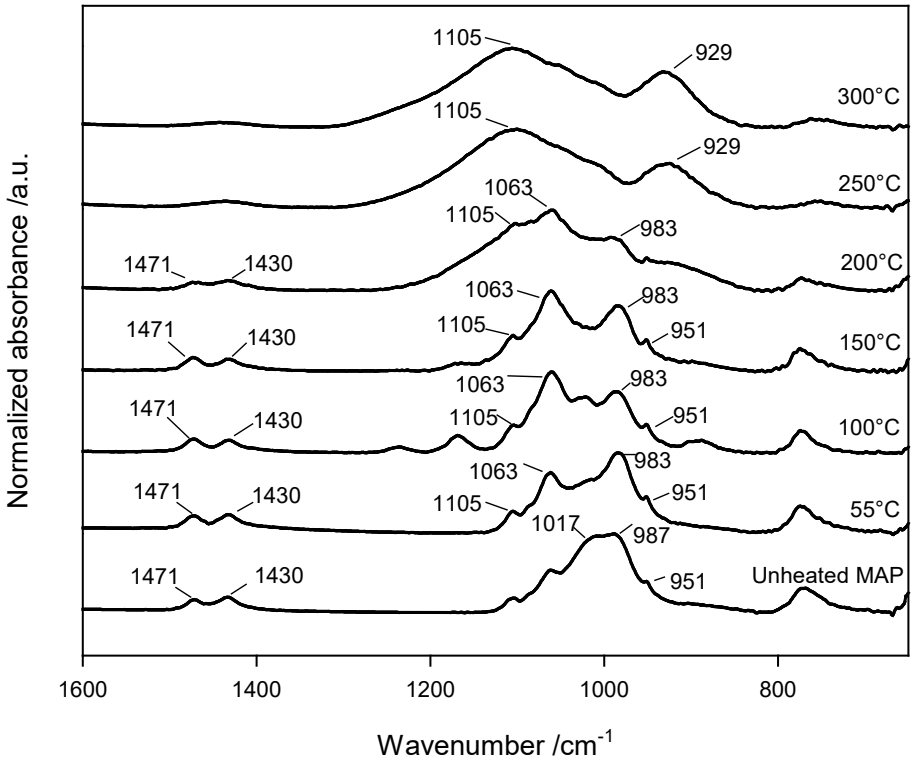

Fig. 2.3 ATR-FTIR spectra of unheated struvite and heat treated solids at wavenumbers in the region of PO_4^{3-} and NH_4^+ vibrations

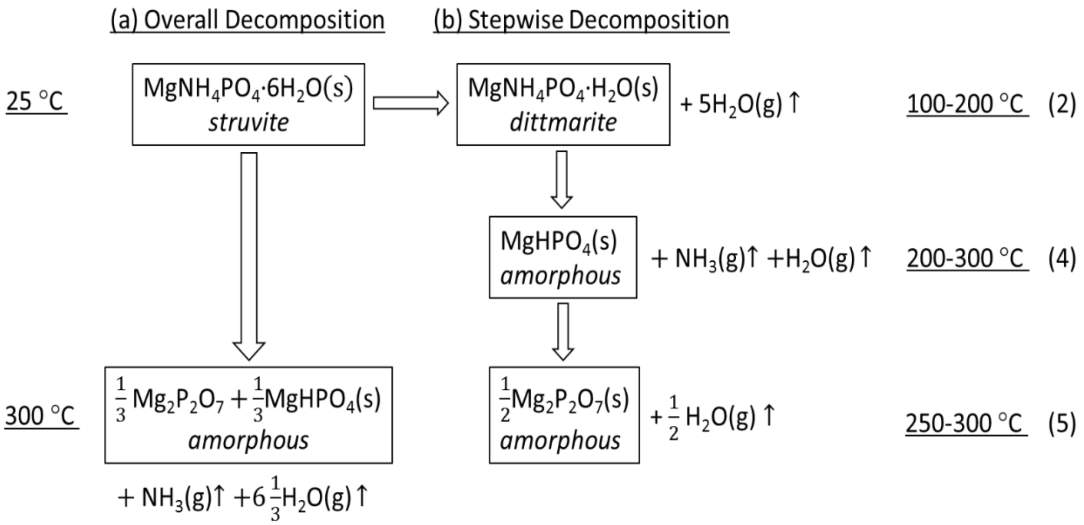

Fig. 2.4 Summary of a) overall decomposition process from 25 to 300 °C and b) stepwise decomposition showing the stable temperature range of each phase. Numbers in brackets are the relevant equations as reported in the text.

Chapter 3: Evaluation of heat-treated struvite as a non-conventional sorbent for ammonia gas using STA-PTA-FTIR[2]

Abstract

Struvite ($MgNH_4PO_4 \cdot 6H_2O$, S-25), a mineral recovered from nutrient-rich wastewaters, was heat-treated at 55-300 ºC, and resultant substrates (HTS-55 to HTS-300) evaluated as sustainable, low-cost sorbents for ammonia gas (NH_3(g)). Experiments were conducted using simultaneous thermal analysis (STA), coupled with pulse thermal analysis (PTA) for gas injection, and Fourier transform infrared spectroscopy (FTIR) for evolved gas analysis (EGA). The STA-PTA-FTIR technique was used to investigate in-situ sorption and desorption of NH_3(g) by HTS substrates, and the associated energetics. The HTS-150 (dittmarite, $MgNH_4PO_4 \cdot H_2O$) sorbent had the highest NH_3(g) uptake, at 23.5 mg g^{-1}. By comparison, commercial biochars exhibited higher NH_3(g) sorption at 42.1-52.6 mg g^{-1}. Sorption was partly reversible, with HTS-150 retaining 37.9% sorbed NH_3(g), which was comparable to or better than biochar retention (12.0-40.8%). Sorption-desorption behavior and associated enthalpies indicate that HTS substrates sorb NH_3(g) by both physisorption, via van der Waals and hydrogen bonding, and chemisorption, via hydroxyl and phosphate groups. Though biochars sorb more NH_3(g), HTS-150 is produced at lower temperatures, requires less energy for pretreatment, and retains an equivalent fraction of NH_3(g) following desorption. Additionally, the HTS starting material is readily recovered from

[2] This chapter is published as: Ramlogan, M.V., Arrue,D.A., Rouff, A.A., 2018. Evaluation of heat-treated struvite as a non-conventional sorbent for ammonia gas using STA-PTA-FTIR. J. Environ. Chem. Eng. 6(2), 2461-2469.

wastewater, promoting valorization. Therefore, HTS substrates are promising non-traditional sorbents for NH_3(g) sequestration.

3.1. Introduction

Ammonia gas (NH_3(g)) is an extensively applied chemical, used in fertilizer [Helminen et al., 2001], household cleaning products [Lee et al., 2011], and industrial flue gas scrubbing [He et al., 2003]. Volatilization of solid-phase and aqueous ammonium (NH_4-N) to produce NH_3(g) causes environmental hazards such as particulate matter formation, eutrophication and soil acidification [Anderson et al., 2003; Moore et al., 1995; Barthelmie and Pryor, 1998; McCubbin et al., 2002; Baek et al., 2004; Lonati et al., 2005; Battye et al., 2003; Xu and Penner, 2012]. Domesticated animal waste is cited as the most important source of NH_3(g) to the atmosphere, contributing 20-35 Tg N yr^{-1} globally [Bouwman et al., 1997]. To manage animal waste, aerobic composting is frequently used [Paillat et al., 2005], but can emit harmful quantities of NH_3(g) [Bernal et al., 2009]. For example, during composting of straw and manures NH_3(g) release resulted in 47-77% of N losses [Martins and Dewes, 1992], thus capture of NH_3(g) for N conservation is of importance.

Existing technologies for NH_3(g) abatement such as air scrubbers are often not viable for agronomic applications. Gas-solid adsorption techniques have been implemented for capture of NH_3(g) generated during industrial processes [Helminen et al., 2001], and adsorption of NH_3(g) has been used to ascertain surface properties of substrates, such as acidity [Nagao, 1976]. Development of environmentally safe, low-cost sorbents for reducing NH_3(g) pollution, especially in agricultural systems, is needed [Kastner et al.,

2009]. Sorbents for NH_3(g) include coconut shell activated carbon [Tsutomu et al., 2004], woody charcoal [Fortier et al., 2008], peat, basalts [Witter et al., 1988], zeolites [Bernal et al., 1993] and metal-organic frameworks [Chen et al., 2018]. Zeolites applied to compost for reducing NH_3(g) emissions immobilized up to 88% NH_4-N [Bernal et al., 1993]. Compost nitrogen losses can also be reduced through solid-phase sequestration of NH_3(g) by addition of Mg and P to induce struvite ($MgNH_4PO_4 \cdot 6H_2O$) crystallization [Jeong and Kim, 2001]. Due to the capacity to sequester NH_4-N in the structure, struvite may also be a viable sorbent for NH_3(g). Struvite can be generated in vast quantities from nutrient-rich wastewater [Le Corre et al., 2009], and recovery for use as a slow-release fertilizer is advantageous [Rahman et al., 2011]. Since struvite is precipitated in excess of what can be applied as fertilizer, the mineral can be used as an easily recoverable and sustainable sorbent.

Struvite heated at elevated temperatures loses waters of crystallization (H_2O(s)) and structural ammonium (NH_4^+(s)), with the percentage of volatiles removed depending on the temperature [Sugiyama et al., 2005; Ma et al., 2014; Ramlogan and Rouff, 2016]. The products can subsequently be used as sorbents. Struvite exposed to a temperature range of 100-800 ºC generated $MgHPO_4$, $Mg_3(PO_4)_2$ and $Mg_2P_2O_7$ for use as adsorbents for aqueous ammonium (NH_4^+(aq)). Highest NH_4^+(aq) removal was observed for $MgHPO_4$ (49%), followed by $Mg_3(PO_4)_2$ (34%), with no sorption observed for $Mg_2P_2O_7$ [Sugiyama et al., 2005]. Struvite decomposition products were also assessed as sorbents for NH_3(g) [Fumoto et al., 2009]. Struvite heated to 105 °C and reacted with NH_3(g) had a loading of 2.56 mol N kg^{-1} and an adsorption enthalpy of -3.0 kJ mol^{-1} [Fumoto et al., 2009]. Assuming all NH_4^+(s) needs to be expelled from the struvite structure to maximize NH_3(g) uptake, a

temperature treatment of 300 ºC is required [Ramlogan and Rouff, 2016]. However, struvite heated to temperatures ≤ 150 ºC retains NH_4^+(s) [Ramlogan and Rouff, 2016], avoiding release of NH_3(g) during sorbent preparation. This temperature range is lower than that required for biochar, another sustainable sorbent, which has pyrolysis temperatures up to 900 ºC. Struvite may therefore be a promising starting material for synthesizing low-cost, sustainable sorbents, with energy-savings compared to biochars.

Gas adsorption can be studied by volumetric and gravimetric methods [Helminen et al., 2001; Belmabkhout et al., 2004; Talu, 1998; Arami-Niya et al., 2017]. In this work, gravimetric adsorption experiments were conducted using a simultaneous thermal analyzer (STA) coupled to a pulse thermal analyzer (PTA) for gas introduction, and a Fourier transform infrared spectrometer (FTIR) for evolved gas analysis (EGA). Compared to typical volumetric and gravimetric methods, adsorption by STA-PTA can be conducted at atmospheric pressure. There are however temporal limitations per pulse leading to shorter durations of adsorptive-adsorbent interaction [Eigenmann et al., 2000]. The most important aspect of STA-PTA-FTIR is that both adsorption and desorption studies can be conducted in-situ, while collecting three sets of data, thermogravimetric (TG), differential scanning calorimetry (DSC) and FTIR, under the same experimental conditions for one sample. Previously, STA-PTA was used to investigate NH_3(g) sorption by H-ZSM-5 zeolite and H-mordenite at 200 °C, and silica-titania aerogel at 50 °C, while varying gas flow rates, temperature, and adsorbent bed thickness [Eigenmann et al., 2000]. Results showed strong (chemisorption) and weak (physical) adsorption by TG, with DSC data correlated to the sorption process [Eigenmann et al., 2000]. The current study implements the STA-PTA-FTIR technique to investigate NH_3(g) adsorption by struvite (S-25) and struvite heat-

treated from 55-300 °C (HTS-55 to HTS-300). For comparison with typical sorbents, NH_3(g) adsorption to two commercial biochars (BC-A, BC-B), was also evaluated. Re-purposing of struvite precipitated from wastewaters promotes wastewater valorization, and re-use for HTS generation could be an environmentally friendly, and sustainable approach for producing low-cost, non-traditional sorbents for NH_3(g).

3.2. Materials and methods

3.2.1. Preparation of sorbents

To produce heat-treated struvite (HTS), 500 mg struvite (Alfa Aesar 98%) was added to a 30 mL high-form porcelain crucible, and heated from room temperature (~25 °C) to 55, 100, 150, 200, 250 or 300 °C for 22 h in a Fisher Scientific Isotemp Muffle Furnace. The recovered substrates were labelled HTS-55 to HTS-300, with the numbers referencing the treatment temperature. According to information obtained from the manufacturer, the commercial biochars (BC-A and BC-B) were formed via slow pyrolysis, at temperatures up to 600 °C.

3.2.2. Characterization of sorbents

The HTS substrates were characterized by x-ray diffraction (XRD), attenuated total reflectance-FTIR spectroscopy (ATR-FTIR), ultra-violet visible spectroscopy (UV-VIS) and inductively coupled plasma optical emission spectroscopy (ICP-OES), as described in

a previous work [Ramlogan and Rouff, 2016]. Results indicated that HTS-55 is struvite, HTS-100, 150 and 200 are the monohydrate dittmarite ($MgNH_4PO_4 \cdot H_2O$) with minor $MgHPO_4$, HTS-250 is $MgHPO_4$ with minor amounts of $Mg_2P_2O_7$, and HTS-300 is $Mg_2P_2O_7$ with minor amounts of $MgHPO_4$ [Ramlogan and Rouff, 2016]. A Perkin Elmer Spectrum 100 FTIR with a universal ATR accessory was used to collect spectra for all substrates before and after reaction with NH_3(g). Spectra were recorded from 650 to 4000 cm^{-1} at a resolution of 4 cm^{-1}. The calculated average of 20 scans was used as a final result. Surface areas were determined by the Brunauer-Emmett-Teller (BET) method using a Micromeritrics accelerated surface area and porosimetry system (ASAP 2020) with N_2(g) as adsorptive. Substrates were degassed at 40 ºC for approximately 24 h prior to BET measurements, which were also conducted at 40 ºC to prevent decomposition of struvite-based substrates at temperatures higher than 50 ºC [Ramlogan and Rouff, 2016; Bhuiyan et al., 2008]. Substrates were coated with iridium for scanning electron microscopy (SEM) analysis (Hitachi S-4800) to determine surface properties and morphology.

3.2.3. Adsorption experiments

A Netzsch Jupiter STA 449 F3, coupled to a Bruker Alpha FTIR (Netzsch Perseus) and a Netzsch PTA 300 was used for the NH_3(g) adsorption experiments. All STA-PTA-FTIR experiment steps, (pretreatment, adsorption, desorption) were conducted at 25 ºC, under a N_2(g) atmosphere, with purge (carrier) and protective flow rates set to 50 and 20 mL min^{-1} respectively. A Netzsch mass flow controller was used to regulate the gas flow rates. The FTIR was used to identify gases evolved during pretreatment, and to monitor

adsorptive flow throughout the adsorption-desorption processes. The FTIR recorded measurements every 16 s from 4400–600 cm^{-1} at 4 cm^{-1} resolution. The gas cell was heated to 200 °C to prevent volatile condensation. Approximately 18.5-25.7 mg substrate was weighed using an analytical balance, and placed in an open ceramic crucible for loading onto the STA sample carrier. Crucible lids were not used so as to maximize contact between sorbent and adsorptive. For removal of pre-adsorbed gases, substrates were heated at a rate of 5 ºC min^{-1} from room temperature, held isothermally at 40 ºC for 1 h, and subsequently cooled to 25 ºC. A pretreatment temperature of 40 ºC was chosen to ensure the S-25 and HTS-55 substrates did not undergo phase transitions that could occur due to heating struvite above 55 ºC [Ramlogan and Rouff, 2016; Bhuiyan et al., 2008]. Pretreatment was stopped when TG/DSC signal stabilization occurred such that mass and heat flow changes were no longer detected. A volume of 50 ppm anhydrous NH_3(g) (99.995%) was used as the adsorptive. When the pulse gas was turned on, each of two 1 mL loops in the PTA 300 box were filled, just prior to injection. Pulse gas was constantly injected in 1 mL increments during the adsorption step until TG/DSC signals remained constant. Stabilization of the STA curves occurred after 171-321 mL NH_3(g) was pulsed in. The FTIR was used to monitor the flow of pulsed NH_3(g). Gram-Schmidt plots provided the total IR absorbance of pulsed gas in the spectral range [Cervantes et al., 2007]. Following the adsorption step, the pressure of NH_3(g) was removed from the carrier gas stream to induce desorption. The desorption step involved flowing N_2(g) over the sorbent until no mass and heat flow changes were detected by TG/DSC. The STA-PTA process (Fig. 3.1) for each tested substrate was performed in duplicate.

3.2.4. Data analysis

Netzsch Proteus software for thermal analysis, version 6.1.0, was used to analyze STA curves produced during the adsorption experiments. Mass changes were calculated from TG plots, with related integral heats of adsorption and desorption determined from the areas under the heat flow curves. Enthalpy data calculated from constant temperature experiments were carried out so that change in temperature over time was zero ($\frac{dT}{dt}=0$), therefore specific heat changes did not influence the DSC signal [Muller et al., 1998]. All reported uptake and enthalpy data represents the mean of two sets of experimental data. Data was reported with a number of significant figures well within the measurement resolution of ± 0.1 μg for TG and <1 μW for DSC. Statistical analysis, carried out for duplicate sorption data, was done using a Student's T test to determine 90% confidence intervals with one degree of freedom.

3.3. Results and discussion

3.3.1. Pretreatment of sorbents

Mass changes were recorded by TG during the three processes of the adsorption experiment, which included sorbent pretreatment (heating, then cooling to 25 ºC), adsorption under atmospheric pressure (injection) and desorption (Fig. 3.2). Mass loss during the pretreatment process for all substrates ranged from 0.32-4.58% (Table 3.1). The pretreatment mass loss for the HTS substrates was lower with higher initial treatment temperature. For biochars, the BC-B substrate showed significantly higher mass loss (4.58%) than the BC-A substrate (0.71%). Pretreatment mass loss may occur from

evolution of surface-bound species [Liu et al., 2015] such as carbon dioxide (CO_2(g)) and water vapor (H_2O(g)) [Ramlogan and Rouff, 2016], and can be used to ascertain optimal temperatures for removal of preadsorbed gases [Eigenmann et al., 2000]. Release of CO_2(g) and H_2O(g) during substrate pretreatment was confirmed by EGA using FTIR (Table 1). Preadsorbed molecules bound to substrate surfaces could limit the total available adsorption sites for NH_3(g). A previous study found that chemisorption of NH_3(g) on dehydroxylated sites occurred when one molecule of NH_3(g) replaced one molecule of desorbed H_2O(g) [Nagao et al., 1976]. Therefore pretreatment to generate an outgassed substrate is probably necessary to optimize sorption [Linares-Solano et al., 1998].

3.3.2. Ammonia gas adsorption by Pulse TA

Injection of NH_3(g) resulted in a rapid increase in mass in the TG curves (Fig. 3.3), confirming uptake of NH_3(g). Mass percentage increased with continuous injections of adsorptive. A plateau in the TG curves was established after injecting volumes ranging from 171-321 mL NH_3(g) (Table 3.2). Additional injections did not result in further mass change (Fig. 3.3), suggesting available adsorption sites were filled. The total mass adsorbed at the plateaus was dependent on the substrate and ranged from 4.1 (S-25) to 50.6 (BC-B) mg NH_3(g) g^{-1} sorbent with 90% confidence intervals ranging from 1.8 to 0 (Table 3.2). The trend in NH_3(g) adsorption was BC-B > BC-A > HTS-150 > HTS-200 >HTS-250 > HTS-300 > HTS-100 > S-55 > S-25 (Table 3.2). The adsorption capacities of the HTS substrates ranged from 4.1 to 23.5 mg NH_3(g) g^{-1} sorbent. In general, mass adsorbed increased with increasing HTS treatment temperature. Adsorption capacity increased

roughly fivefold for HTS-150 compared to S-25 and HTS-55. Structural water appeared to affect uptake of NH_3(g) since the heat-induced phase transition from hexahydrate, $MgNH_4PO_4 \cdot 6H_2O$ (S-25, HTS-55) to monohydrate, $MgNH_4PO_4 \cdot H_2O$ (HTS-100, HTS-150, HTS-200) promoted uptake. The HTS-150 substrate, which was primarily the monohydrate dittmarite [Ramlogan and Rouff, 2016], showed the highest uptake of the three monohydrate-bearing substrates (HTS-100, HTS-150, and HTS-200). Then with loss of both structural H_2O(s) and NH_4^+(s) in HTS-250 ($MgHPO_4$) and HTS-300 ($Mg_2P_2O_7$), uptake decreased relative to the observed trend.

The instantaneous response (fast kinetics) in the TG signal to pulsing of NH_3(g) observed for all substrates is an indication of physical adsorption [Panella et al., 2006]. Physical adsorption involves London dispersion forces, polar interactions leading to specific interactions [Thommes, 2010], van der Waals forces [Tao and Rappe, 2014], hydrogen bonding [Chen et al., 2016] and attractive dispersion forces, leading to non-specific molecular interactions. Images from SEM (Fig. 4) revealed thermal effects from heating (furnace heat treatment 55-300 ºC) on the morphology of the HTS substrates including increased presence of surface pores, and other features (roughness, pitting), that could lead to greater surface area. Results from BET analysis (Fig. 3.5) confirmed an increase in surface area for HTS-150, HTS-250 and HTS-300 compared to S-25. These substrates showed higher adsorption capacity for NH_3(g) relative to S-25. The increased presence of pores and coarseness in the HTS substrates, as observed by SEM, probably caused the increased surface area in HTS substrates compared to S-25. Since physisorption is enhanced by increased surface area [Berger and Bhown, 2011], this may partially explain some of the adsorption capacities observed for the HTS substrates. However, factors other

than physical properties, such as the speciation of available binding sites, as dictated by the mineralogy, will strongly influence sorption. For example, the HTS-200 substrate had the lowest BET surface area, but the second highest NH_3(g) sorption of the HTS substrates (Fig. 3.5), indicating chemical rather than physical factors dictating sorption. For the biochars, surface speciation, in particular the presence of acidic functional groups, along with porosity and high surface area contribute to NH_3(g) sorption [Tsutomu et al., 2004].

3.3.3. Desorption of ammonia gas

Removal of NH_3(g) from the carrier gas stream resulted in desorption of some adsorbed NH_3(g) (Fig. 3.3). The percentage of NH_3(g) remaining after desorption ranged from 0 to 40.8% (Fig. 3.5). With the exception of the S-25 and HTS-55 substrates, for which all NH_3(g) was desorbed, the sorbents retained some mass of NH_3(g), with BC-B > HTS-150 > HTS-100 > HTS-300 > HTS-250 > HTS-200 > BC-A (Table 3.2, Fig. 3.5). All HTS substrates retained 26.2%-37.9% of the total adsorbed NH_3(g), with the value for HTS-150 (37.9%) comparable to BC-B (40.8%). For BC-A, only 12% of adsorbed NH_3(g) was retained subsequent to desorption, and was the lowest for the sorbents for which partial sorption reversibility was observed.

For the S-25 and HTS-55 substrates, based on the fully reversible desorption behavior recorded by TG, it is unlikely that chemisorption, which requires an activation energy, occurred. However, for the HTS-150 substrate, some mass of NH_3(g) remaining after desorption may be attributed to chemisorption [Eigenmann et al., 2000]. Based on BET measurements, HTS-150 had a lower surface area than HTS-250 and HTS-300, yet

had higher adsorption capacity, suggesting surface area was less important for NH_3(g) adsorption. This further indicated a higher affinity of NH_3(g) for the HTS-150 surface compared to the other HTS substrates, perhaps arising from differences in the speciation and availability of reactive surface sites such as OH^-(s), PO_4^{3-}(s) and NH_4^+(s). Therefore, it is likely stronger sorbate-sorbent bonds were formed, such that simply removing the flow of NH_3(g) did not result in full reversibility in the adsorption. For HTS-250 and HTS-300, as surface area increased, the mass of sorbate retained after desorption also increased (Fig. 3.5). A facile explanation for the observed desorption behavior for HTS-250 and HTS-300 could be that some mass of NH_3(g) was trapped inside surface pores and pits, which effectively sequestered the adsorptive, hence limiting desorption. Though HTS-200 had slightly higher NH_3(g) sorption than HTS-250 and HTS-300, which may also be influenced by the type of binding sites, the fraction of irreversibly bound NH_3(g) was slightly lower, indicative of more weakly bound surface complexes.

3.3.4. Thermodynamics of adsorption

During pretreatment, DSC measurements confirmed small endothermic transitions (Fig. 3.2), ranging from 5.2-17 J g^{-1}, attributed to preadsorbed gas evolution (Table 3.1). A smaller pretreatment endotherm for HTS-150 compared to BC-B could be beneficial since a less energy intensive process would be needed to optimize the substrate surface for adsorption. To determine integral adsorption enthalpies, DSC measurements were carried out during NH_3(g) uptake (Fig. 3.3). Surface energetics, or binding energy of adsorption sites, play a key role in determining the adsorption behavior of heterogeneous surfaces.

Powdered minerals typically have heterogeneous surfaces due to natural disruptions in mineralogy, impurities, variable pore sizes, and crystal surfaces with different energies [Villieras et al., 1992]. The powdered HTS substrates produced heat flow curves with varying magnitudes of exothermic transitions caused by the adsorption process (Fig. 3.3). The observed exotherms were expected since gas adsorption onto a solid is spontaneous [Chiang et al., 2001] when Gibb's free energy is negative ($-\Delta G°$), and the change in adsorptive entropy ($\Delta S°$) is negative, therefore $\Delta H°$ ads must be a negative value because:

$$\Delta G° = \Delta H° - T\Delta S° \quad (3.1)$$

and for $\Delta G°$ to be negative due to the spontaneous nature of gas-solid adsorption, $\Delta H°$ must be a negative value and $|\Delta H°| > |T\Delta S°|$.

Integral heats of adsorption (J g^{-1}) were calculated from the areas under the exothermic peaks [Pires et al., 2000] that were associated with mass gain (Table 3.2). The adsorption enthalpies ranged from -4.6 to -118.9 J g^{-1}. In general, the higher the adsorbed mass of NH_3(g), the larger the magnitude of the exothermic response in the DSC signal, and the magnitude of these values suggested physisorption was the dominant mechanism [Sexton and Hughes, 1984] (Table 3.2). The affinity of the adsorptive for the tested substrates can be described by the magnitudes of the exothermic responses. For example, the S-25 (-4.6 J g^{-1}) and HTS-55 (-6.8 J g^{-1}) substrates produced very low exothermic responses during pulsing, which was probably due to a decrease in affinity resulting in low adsorption capacity for NH_3(g). All other HTS substrates produced exotherms that were larger than S-25 and HTS-55, but smaller than the BC substrates, which retained more adsorptive during pulsing (Table 3.2).

During desorption, endothermic transitions were caused by evolution of sorbate to the gas phase [Scheirs et al., 2001]. Positive enthalpies ranged from 1.3-67.6 J g^{-1} (Fig. 3.3). Endothermic transitions during desorption were always smaller than the exothermic responses to mass adsorbed, and in general substrates with higher uptake subsequently lost more mass resulting in larger endothermic transitions. For example, more heat was absorbed by HTS-150, 200, 250 and 300, compared to S-25 and HTS-55 and HTS-100, but significantly less than the heat absorbed by BC-A and BC-B. Partial desorption arising from condensation of NH_3(g) into pores may have caused the smaller endotherms since sorbate diffusion into pores is a phenomenon in sorption processes causing incomplete desorption and hysteresis [Peel et al., 1981; Harding et al., 1998].

3.3.5. Fourier transform infrared spectroscopy

The FTIR results for HTS-150 and HTS-300 substrates before STA-PTA (Fig. 3.6) were in good agreement with previously published absorption spectra for these solids [Ramlogan and Rouff, 2016]. The mid-infrared spectra indicated vibrations for PO_4^{3-}(s) and NH_4^+(s) were consistent with past characterizations [Ramlogan and Rouff, 2016]. Subsequent to desorption, substrates were analyzed by FTIR to determine possible binding sites of NH_3(g) by examining any changes to the infrared spectra of the substrates, where applicable. There were no major changes to the absorption spectra of HTS-150 and HTS-300, after the STA-PTA-FTIR process (Fig. 3.6). This may be due to the sorption of NH_3(g) at concentrations that are below detection and/or produce no effect on the vibrations of the IR sensitive functional groups. A small peak around 1438 cm^{-1} attributed to NH_4^+(s)

[Ramlogan and Rouff, 2016], developed in both BC-A, (not shown), and BC-B substrates (Fig. 3.6), subsequent to STA-PTA. The appearance of the NH_4^+(s) signal indicated protonation of the adsorptive upon contact with BC surfaces, perhaps due to adsorption onto hydroxyl groups [Ahmad et al., 2012].

3.3.6. Struvite-based sorbents for NH_3(g) sequestration

Struvite, and heat-treated struvite were selected as alternative sorbents for NH_3(g) and compared to typical biochar sorbents, using a novel STA-PTA-FTIR technique. The technique was shown to be useful for the purposes of this investigation, with relevant data (TG/DSC) collected using precise, yet relatively fast measurements, and without the complexities of standard volumetric apparatus. Results indicated that HTS substrates effectively sorbed NH_3(g) at 25 ºC and 1 atm. The NH_3(g) adsorption capacity was dependent on the chemical composition of substrates, surface energetics, and physical properties with BC-B > BC-A > HTS-150 > HTS-200 >HTS-250 > HTS-300 > HTS-100 > S-55> S-25. Adsorption was either partly or completely reversible, indicating multiple bonding environments for NH_3(g) depending on the sorbent. Possible mechanisms of NH_3(g) adsorption include both physical adsorption and capillary condensation. Intermolecular attractive forces, such as van der Waals forces, can lead to physical adsorption [Tao and Rappe, 2014]. Hydrogen bonding of NH_3(g) to surface hydroxyl groups [Chen et al., 2016] could have promoted sorption via sites dehydroxylated after pretreatment [Nago et al., 1976]. DSC confirmed exothermic transitions always accompanied adsorption; physisorption is associated with a decrease in free energy and

entropy of adsorption making the process exothermic. TG/DSC data during desorption revealed a partial reversibility in uptake. Capillary condensation could have facilitated the retention of NH_3(g) in HTS-250 and HTS-300 sorbents. However, for HTS-150 and HTS-200 chemisorption and binding to high affinity sites is likely to have also occurred.

Of the HTS substrates, HTS-150 was the most effective at adsorbing NH_3(g), with approximately half of the sorption observed with biochars. Biochars are effective sorbents due to high surface area [Ahmad et al., 2012], and the inherently complex nature of the biochar surface provides many reactive sites for sorption [Ahmad et al., 2014]. For example, biochars produced at different temperatures have been shown to exhibit varied affinity for ions such as copper and zinc [Chen et al., 2011]. Struvite, produced at ambient temperature has been shown to sorb ions such as Cu, Zn, Cr, As [Rouff et al., 2016; Rouff, Ma et al., 2016; Rouff and Juarez, 2014; Rouff, 2013; Rouff, 2012; Ma and Rouff, 2012; Rouff, 2012] from different solutions, through several mechanisms. The advantage of struvite, compared to biochars for pollutant removal from solution, as well as from the gas phase, as demonstrated in this work, is lower energy costs associated with HTS production. Biochar production requires pyrolysis temperatures ranging from 100 to 900 ºC [Ahmad et al., 2013]. For example, past work showed palm oil shell pyrolysis at 500 ºC was necessary to generate a biochar substrate with good affinity for NH_3(g) [Kastner et al., 2008]. Generating HTS-150 for capture of NH_3(g) using substantially lower temperatures than 500 ºC is an energy saving process. Furthermore, if retention of sorbed NH_3(g) is desired, HTS-150 (38%) and BC-B (41%) retained a similar percentage of NH_3(g) after desorption. Additionally, when heating struvite to generate HTS-150 ($MgNH_4PO_4 \cdot H_2O$), structural NH_4^+(s) is not volatilized, but is retained in the structure.

3.4. Conclusion

There is a need to develop low-cost alternative sorbents for $NH_3(g)$ [Zheng et al.,2016]. The HTS substrates are derived from a wastewater byproduct, which requires low temperature treatment for generation of the sorbent. Therefore, wastewater valorization combined with energy savings are major benefits of these non-traditional sorbents. Sorption-desorption behavior and associated enthalpies indicate that HTS substrates sorb $NH_3(g)$ by both physisorption, such as van der Waals and hydrogen bonding, and chemisorption, via hydroxyl and phosphate groups. Though HTS-150 sorbs less $NH_3(g)$ compared to biochars, removal of $NH_3(g)$ can be improved by increasing the mass of sorbent. This in turn is feasible because struvite can be mined in large quantities from wastes and wastewaters, and the preparation of HTS-150 is less energy intensive compared to biochars. Use of HTS-150 for capturing $NH_3(g)$ could therefore be a good reason for developing this type of sustainable sorbent. Since surplus struvite is spontaneously precipitated in wastewater systems under favorable conditions, further uses besides application as fertilizer should be explored. Fundamental research conducted in this work has shown good potential in struvite for development as a low-cost sorbent for $NH_3(g)$.

Acknowledgements

This work was supported by National Science Foundation Grant No. EAR-1506653. The authors thank Dr. Evert Elzinga for use of FTIR, Jalise Wright for acquisition of biochars, and Dr. Kristina Keating for use of BET

Tables and Figures

Table 3.1. STA-FTIR data for sorbent pretreatment.

Sorbent	TG mass loss (%)	DSC endotherm (J g^{-1})	FTIR volatiles
S-25	1.58	7.9	H_2O
HTS-55	1.22	7.5	H_2O
HTS-100	2.91	9.0	CO_2 , H_2O
HTS-150	1.1	7.0	CO_2 , H_2O
HTS-200	1	7.3	CO_2 , H_2O
HTS-250	0.39	6.1	CO_2 , H_2O
HTS-300	0.32	5.2	CO_2 , H_2O
BC-A	0.71	5.4	CO_2 , H_2O
BC-B	4.58	17.0	CO_2 , H_2O

Table 3.2. STA-PTA data for adsorption and desorption processes. The 90% confidence interval for sorption data is italicized and reported in brackets.

Sorbent	NH_3(g) initial (mL)	NH_3(g) sorption (mg g^{-1})	Sorption enthalpy (J g^{-1})	NH_3(g) after desorption (mg g^{-1})	Desorption enthalpy (J g^{-1})
S-25	261	4.1 *(1.8)*	-4.6 *(1.5)*	0.0	1.3
HTS-55	171	4.8 *(0.6)*	-6.8 *(1.6)*	0.0	1.7
HTS-100	180	9.9 *(0.9)*	-21.8 *(13.0)*	3.6	3.5
HTS-150	321	23.5 *(1.9)*	-65.0 *(24.3)*	8.9	11.5
HTS-200	261	15.8 *(1.4)*	-39.4 *(11.7)*	4.2	8.3
HTS-250	216	14.2 *(1.7)*	-35.8 *(2.1)*	4.5	7.0
HTS-300	186	13.8 *(1.1)*	-35.4 *(1.5)*	4.8	5.4
BC-A	300	42.1 *(0.2)*	-83.2 *(25.9)*	5.1	67.6
BC-B	294	50.6 *(0)*	-118.9 *(9.2)*	20.7	1.3

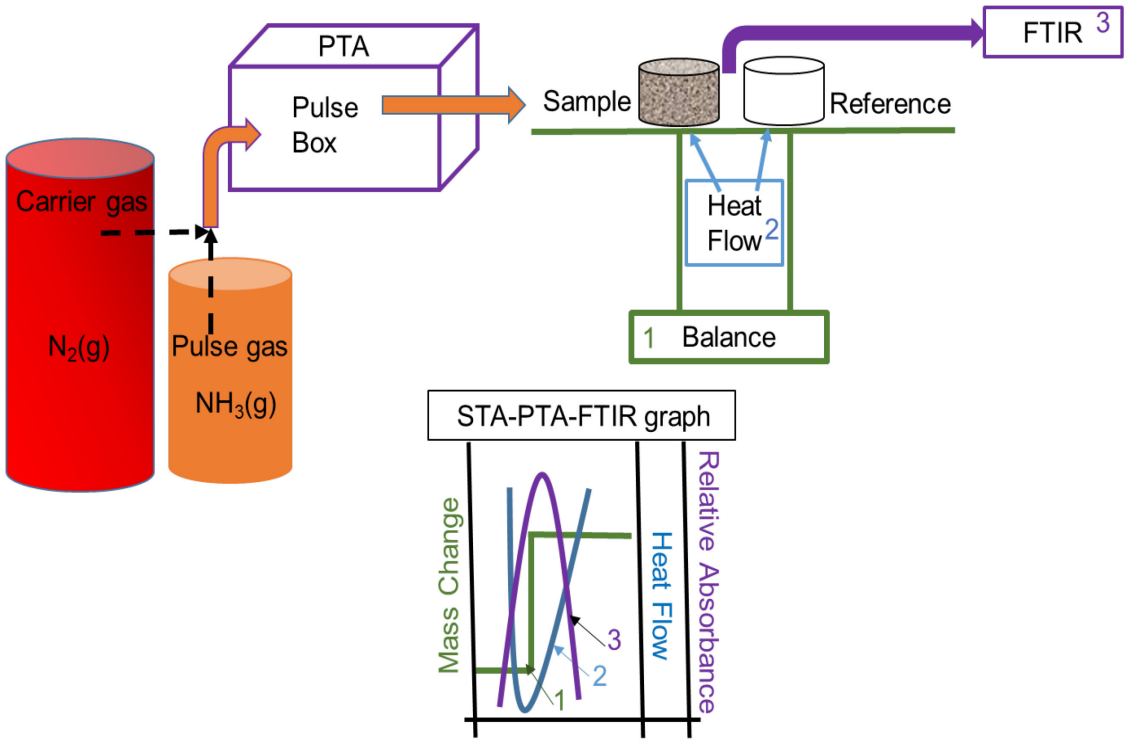

Fig. 3.1. Schematic of the STA-PTA-FTIR experiment. Pulse (NH_3) and probe (N_2) gas pathways are in orange, and the total outgas pathway is in purple. A graph of representative curves obtained is displayed. Number key: 1. Mass change (TG); 2. Heat flow (DSC); 3. EGA (FTIR)

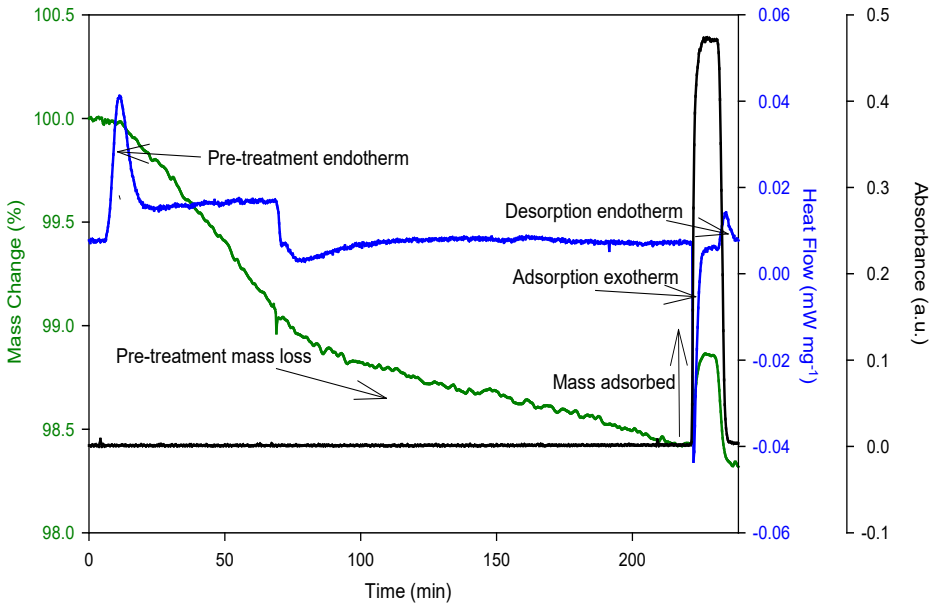

Fig. 3.2. STA-PTA-FTIR results for the S-25 sorbent with pretreatment, adsorption and desorption data delineated. Green, blue and black curves represent TG mass change (%), DSC heat flow (mW mg^{-1}) (exo down), and FTIR Gram-Schmidt absorbance (a.u.), respectively.

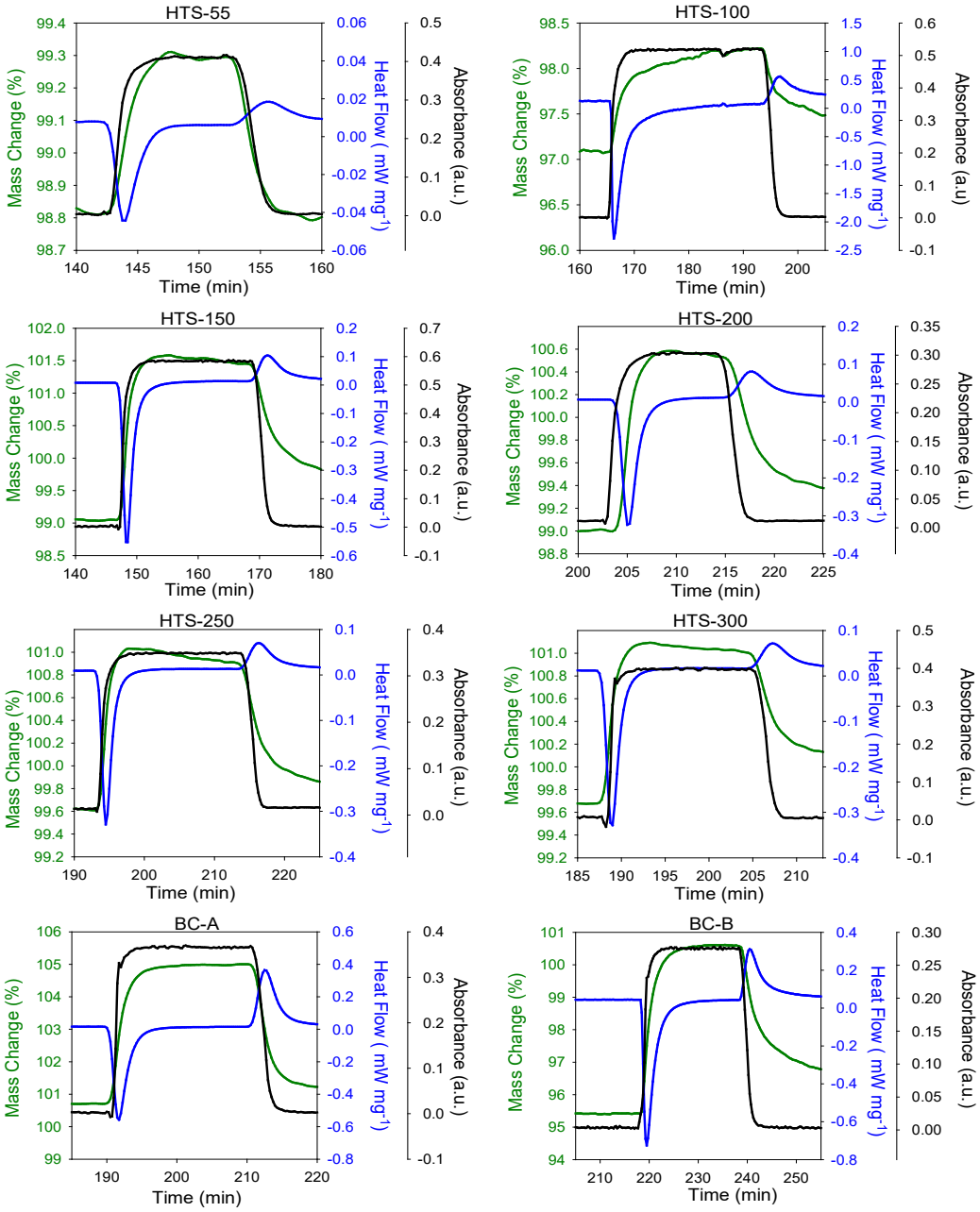

Fig. 3.3. STA-PTA-FTIR data of NH_3(g) uptake for HTS and biochar substrates. The green, blue and black curves represent TG mass change (%), DSC heat flow (mW mg^{-1}) (exo down), and FTIR Gram-Schmidt absorbance (a.u), respectively. Integral heats of adsorption were calculated from the areas under the exothermic peaks (exo down).

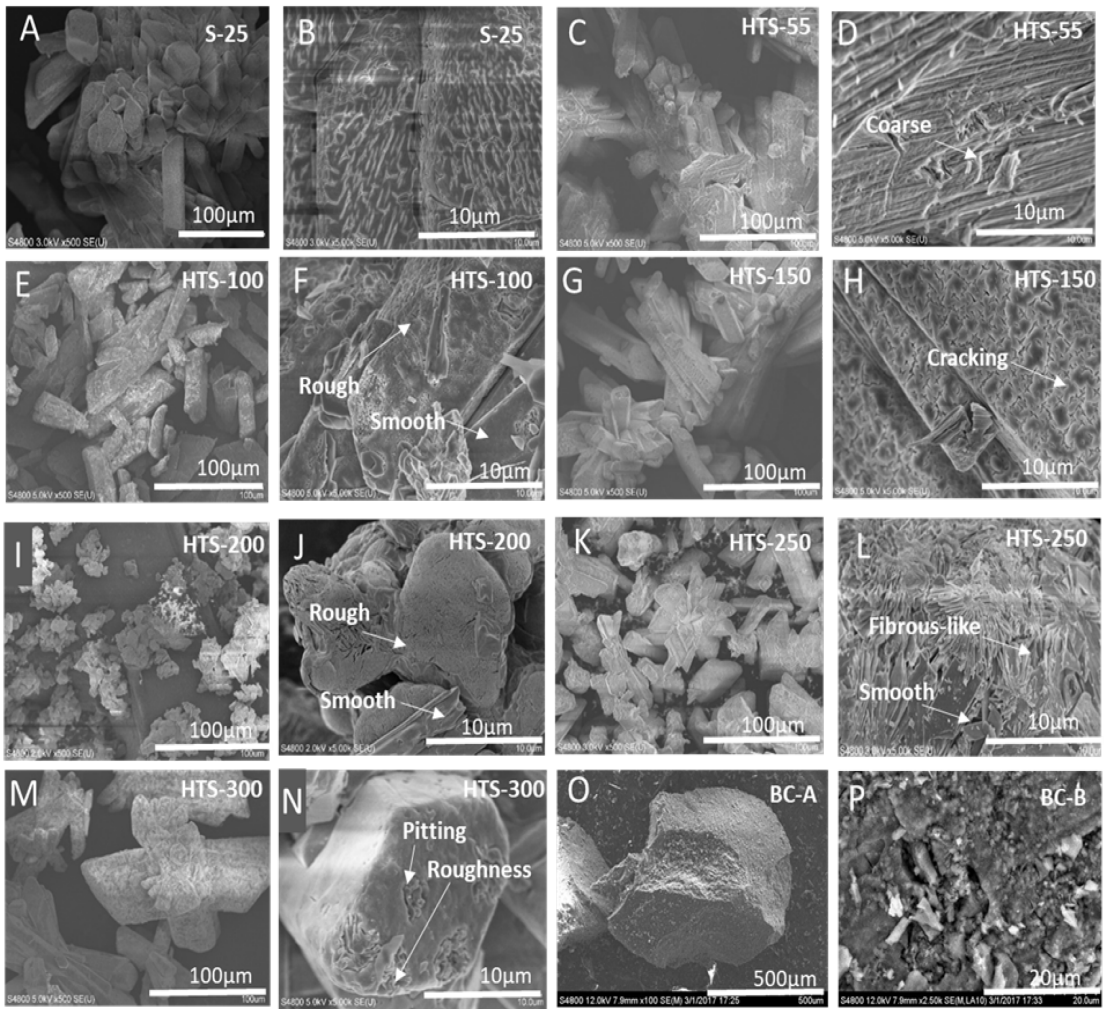

Fig. 3.4. SEM images of S-25 and HTS substrates at 500× (100 µm scale bar), and 5× (10 µm scale bar) magnification (A-N), and SEM images of biochars BC-A and BC-B (O-P).

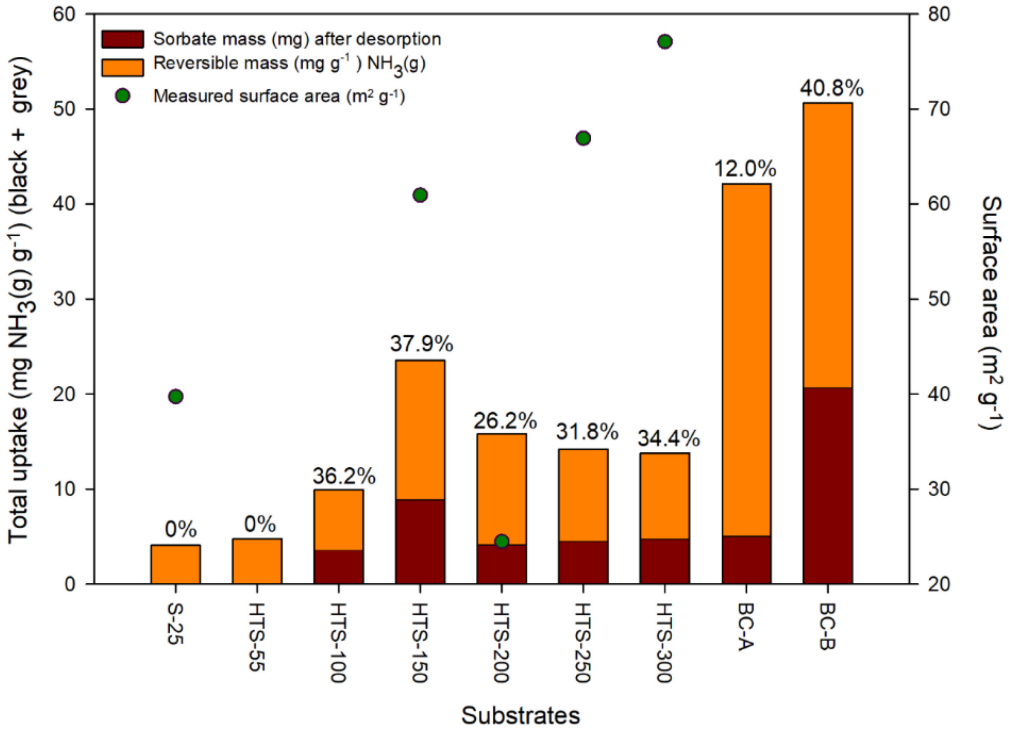

Fig. 3.5. The total uptake of $NH_3(g)$ for all substrates is shown (orange + brown) comprised of the sorbed mass of $NH_3(g)$ (mg g^{-1}) (brown) remaining after desorption, and the reversible sorbate mass (mg g^{-1}) (orange). The percentages of $NH_3(g)$ retained after desorption are given. Surface areas for select substrates are also reported.

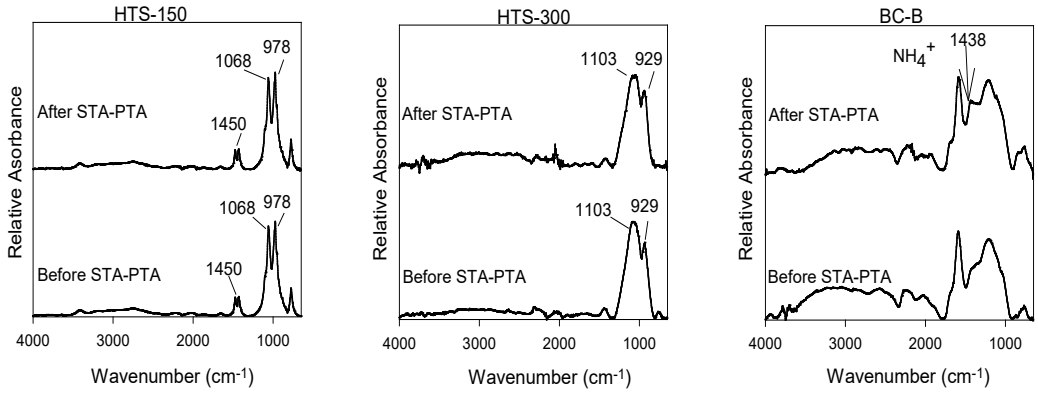

Fig. 3.6. ATR-FTIR spectra before and after sorption for select substrates. The peaks centered around 1000 and 1450 cm^{-1} were attributed to the ν_3 antisymmetric stretching vibration of PO_4^{3-} and the ν_4 asymmetric bending of NH_4^+ respectively (HTS-150). Peaks at 929 and 1103 cm^{-1} were assigned to the δ(POH) vibrational bands of $Mg_2P_2O_7$ (HTS-300). The NH_4^+ band appearing in the BC substrates after STA-PTA is labelled as the peak at 1438 cm^{-1}.

Chapter 4 : Thermochemical Analysis of Ammonia Gas Sorption by Struvite from Livestock Wastes and Comparison with Metal Organic Framework and Biochar Sorbents[3]

Abstract

Ammonia gas (NH_3(g)) sorption onto environmentally relevant solids recovered from swine (S) and dairy (D) wastewaters is evaluated. The objective of this study is to elucidate sorption capacity, and thermodynamic and kinetic parameters associated with NH_3(g) interactions with the heated (150, 300 °C) products of S (struvite) and D (struvite-calcite) precipitates. The sorption of NH_3(g) onto S and D sorbents was performed by simultaneous thermal analysis-pulse thermal analysis-Fourier-transform infrared spectroscopy (STA-PTA-FTIR). Heating S solids to 150 °C enhanced sorption capacity by 320% (S35), and 400% (S15) as compared to unheated solids. Heat treatment of D resulted in slight increases in NH_3(g) sorption. For the S and D sorbents, exothermic heats of sorption from -22.1 to -131J g^{-1} indicated surface energetic heterogeneity. Changes in vibrational modes of surface hydroxyl groups, as detected by attenuated total reflectance-FTIR (ATR-FTIR), were used to determine sorption sites. Following desorption, S and D sorbents retained 0-51% sorptive. Arrhenius parameters calculated from thermogravimetric curves by model-dependent kinetic analysis and Friedman method described the overall kinetics of sorption-desorption. Of the S and D sorbents, the fastest reaction rate k was found for S35-150. The

[3] This chapter is in preparation for submission in Journal of Environmental Chemical Engineering

tested S and D sorbents represent alternative economical and sustainable treatment for NH_3(g) mitigation.

4.1. Introduction

Ammonia ((NH_3(g)) is a highly toxic air pollutant that causes detrimental environmental hazards including formation of atmospheric particulate matter [Zhao et al., 2015; Wu et al., 2016], haze pollution [Wang et al., 2015] and respiratory ailments [Lelieveld et al., 2015]. Transfer of NH_3(g) to terrestrial and aquatic systems via wet and dry deposition can cause eutrophication [Leip et al, 2015] and acidification [Kruse and Bell, 1967], negatively impacting sensitive ecosystems [Ferm, 1998; Walters et al., 2018]. Since NH_3(g) is one of the most important alkaline species on Earth, and is continuously produced [Vikrant et al., 2017], a critical aspect of global air quality control is the mitigation of NH_3(g) emissions. Reducing NH_3(g) emissions lowers the concentration of alkaline and malodorous volatiles present in the atmosphere [Aneja et al., 2008], and limits subsequent impacts on human health and environmental systems.

Agricultural systems (65 Tg N), [Bouwman et al., 1997; Sarkar, 1991] account for over 50% of total annual global NH_3(g) emissions [Gronwald et al., 2018]. Composting of animal manure [Gronwald et al., 2018], food waste [Niraula et al., 2018], and other organic-based wastes emit NH_3(g) during decomposition of organic matter. The release of NH_3(g) from composting is a temperature-dependent process [Gronwald et al., 2018] that occurs in stages at compost heap temperatures of 30-60 °C [Wang and Zeng, 2018]. Field application of manures and commercial fertilizers can result in wasteful depletion of N [Pagans et al., 2006; Wang and Zeng, 2018; Van der Weerden and Jarvis, 1997] due to

volatilization as $NH_3(g)$, exacerbating nutrient loss from soils. The rising demand for reactive (bioavailable) N utilized in global food production may further intensify environmental impacts brought about by concomitant emissions of $NH_3(g)$. Maximizing crop yields by mitigating bioavailable N losses [De-Xi et al., 2007] is therefore imperative.

Chemical additives can be used to reduce N losses in agricultural systems [Shreve et al., 1995; Reece et al., 1979; Bussink et al., 1994; Moore et al., 1996]. For example, acidification of a cattle waste slurry to pH 4.5 using nitric acid ($HNO_3(aq)$) reduced $NH_3(g)$ volatilization by 85% [Reece et al., 1979]. However, cost effectiveness and potential environmental drawbacks restrict the application of chemical amendments [Bussink et al., 1994; Vandre and Clemens, 1996]. Instead, sorbents could be more feasible and environmentally safe additives for $NH_3(g)$ capture, especially near delicate ecosystems [Lefcourt and Meisinger, 2001; Li et al., 2008; Agyarko-Mintah et al., 2017; Sanchez-Monedero et al., 2018]. Previously studied sorbents for $NH_3(g)$ include natural zeolites and sepiolite [Ramlogan et al., 2018], alumina, silica gel, activated carbon [Bernal and Lopez-Real, 1993] and covalent organic frameworks (COFs) [Helminen et al., 2001]. Biochar sorbents derived from greenwaste and poultry litter lowered $NH_3(g)$ emissions of compost bins by 58 and 38% respectively [Li et al., 2008]. Although biochar is a highly effective sorbent, biochar synthesis is complex, emits volatile pyrolysis products such as polycyclic aromatic hydrocarbons (PAH) [Doonan et al., 2010; Hale et al., 2012] and is highly energy intensive, typically requiring >400 °C pyrolysis temperatures [Buss et al., 2016; Xie et al., 2015]. The sorbent properties can be highly variable as the parent material and pyrolysis reactions can significantly alter key characteristics [Xie et al., 2015], including surface chemistry and surface area of the recovered biochar product. Metal-organic frameworks

(MOFs) are also high performing sorbents due to their inherent framework morphology, high porosity and active binding sites [Suliman et al., 2016]. Metal binding sites such as Cu(II) sites in the HKUST-1 MOF facilitate chemisorption of NH_3(g) via electrostatic interactions [Bowser et al., 2018]. The capture of NH_3(g) by HKUST-1 can surpass that of known sorbent materials, for example, porous carbons [Borfecchia et al., 2012; Peterson et al., 2009]. Although MOFs are appealing sorbents, they are known to degrade in water and require considerable design and functionalization [Petit et al., 2011], hence the use of MOFs in agricultural systems is rare [Jasuja et al., 2015].

To reduce costs and conserve natural resources by wastewater valorization, recycling wastes as raw materials for generating alternative sorbents has been suggested [Anstoetz et al., 2016]. Struvite, ($MgNH_4PO_4{\cdot}6H_2O$), is a valuable mineral which is readily recovered from N and phosphorus (P)-rich wastewaters [Silva et al., 2018; Booker et al., 1999]. Commercial struvite and its heat-treated (55-300 °C) decomposition products [Huang and Zhang, 2011] were evaluated as non-conventional sorbents for NH_3(g) [Ramlogan et al., 2018]. Struvite treated at 150 °C (HTS-150) sorbed 23.5 mg NH_3(g) g^{-1} compared to 42.1–52.6 mg NH_3(g) g^{-1} for tested biochars. After desorption, 37.9% sorbed NH_3(g) was retained by HTS-150, which was comparable to or surpassed 12.0–40.8% NH_3(g) retention by biochars [Ramlogan et al., 2018]. Therefore, struvite-based sorbents may be as effective as biochars in retaining NH_3(g). However, further research is required to design and optimize waste-derived alternative sorbents, which in turn are economically produced, environmentally benign and suitable for agricultural applications. In general, very few studies [Ramlogan et al., 2018] have been published describing NH_3(g) sorption on these types of sorbents.

In this study, $NH_3(g)$ sorption to heat-treated solids recovered from livestock wastewater effluents [Rabinovich et al., 2017] was evaluated and compared to sorption by biochar and HKUST-1 MOF. Solids recovered from swine waste were mainly pure struvite, and those from dairy waste were primarily a mixture of struvite and calcite. Sorption experiments were carried out by simultaneous thermal analysis-pulse thermal analysis-evolved gas analysis (STA-PTA-EGA) [Ramlogan et al., 2018]. This method was used to study sorbate-sorbent reactions in-situ under environmental conditions, and at temperatures relevant to agricultural systems, such as during the thermophilic stage of composting processes [Wang and Zeng, 2018]. The combined STA (TG-DSC) data was used to determine kinetic parameters for both sorption and desorption. The research explores a creative and novel use for effluent-derived solids, thereby promoting wastewater valorization [Ramlogan and Rouff, 2016; Rouff, 2012; Ma et al., 2014] and the benefits of using sustainably sourced parent material as sorbents for mitigating atmospheric $NH_3(g)$ pollution.

4.2. Materials and Methods

4.2.1. Sorbents

Sorbents sourced from swine (S) and dairy (D) wastewater were acquired from previous work [Rabinovich et al., 2017]. The sorbents were recovered from swine (SWW) and dairy (DWW) effluents following treatment in an aerated fluidized bed reactor (aerated-FBR) at pH 9, at different retention times, (15, 35, 68 min). The solids were stored

at room temperature for 6 months after initial recovery and labeled according to the waste source and treatment time, (SWW15, SWW35, DWW35, DWW68). The SWW solids were primarily struvite (93-98%), highly crystalline (94%) and had a low organic content (2-5%) [Rabinovich et al., 2017]. The DWW solids were a mixture of struvite (28-33%), calcite (17-55%) monohydrocalcite (4-13%) and K-struvite (3-8%), and were less crystalline (75-87%) and had a higher organic content (7-29% w/w) than SWW solids [Rabinovich et al., 2017]. Commercially obtained struvite (Alfa Aesar, 98%) and calcite (Acros Organics 99%), were evaluated for comparison with wastewater derived samples, and to determine the impact of the mineralogical components of DWW (Table S1). A MOF and a biochar sorbent were also assessed for comparison. A copper benzene-1,3,5-tricarboxylate, ($C_{18}H_6Cu_3O_{12}$), (HKUST-1) MOF sorbent was obtained from Sigma Aldrich (Basolite^{TM} C300, BET surface area 1500-2100 m^2 g^{-1}). The biochar sorbent (BC) was commercially sourced, and was generated by slow pyrolysis of untreated wood materials (saw dust, yard trimmings), at temperatures up to 600 °C.

4.2.2. Preparation and Characterization of Wastewater Sorbents

Heat-treated S15, S35, D35 and D68 sorbents were generated from SWW and DWW solids. Approximately 300 mg of the powdered SWW or DWW solid was placed in 30 mL high-form porcelain crucible and heated from room temperature (~25 °C) for 22 h in a Fisher Scientific Isotemp Muffle Furnace to either 150 or 300 °C. The heat-treated solids were cooled to room temperature in a desiccator and labelled according to the heat treatment temperature, S15-150, 300; S35-150, 300; D35-150, 300; D68-150, 300. The S

and D sorbents were characterized by X-ray diffraction (XRD; D8 Advance, Bruker) for mineralogy, from 5° to 60° 2θ at 0.016° 2θ resolution. Fourier transform infrared (FTIR) spectroscopy data was collected using a Perkin Elmer Spectrum 100 instrument with a universal attenuated total reflectance (UATR) accessory to determine vibrational modes of dominant functional groups in the heated products. The FTIR spectra were recorded from 650 to 4000 cm^{-1} with a resolution of 4 cm^{-1}. The final spectrum was the calculated average of 20 scans. Selected samples were mounted on copper adhesive tape and coated with iridium to determine morphology by scanning electron microscopy (SEM, Hitachi S-4800). Additional FTIR data were collected for select sorbents before and after reaction with NH_3(g) at 60 °C.

4.2.3. Sorption Experiments

Sorption experiments were conducted using a Netzsch Perseus STA 449 F3 coupled to a Bruker ALPHA FTIR. The experiment consisted of 3 steps: pretreatment, sorption and desorption [Ramlogan et al., 2018]. Measurements were conducted using conditions recommended by the International Confederation for Thermal Analysis and Calorimetry (ICTAC) [Vyazovkin et al., 2014]. A mass of 20.2–26.6 mg sorbent was loaded into an open ceramic crucible. Nitrogen (N_2(g)) was used as both protective and pulse gas, with flow rates of 20 and 50 mL min^{-1} respectively, regulated using a mass flow controller (MFC). Prior to sorption experiments, the sorbents were pretreated to release any adsorbed gases. The sorbents were heated from room temperature and held isothermally at either 40, 50 or 60 ºC, depending on final sorption experiment temperature,

for 1 or 24 h. Sorption of NH_3(g) by pretreated sorbents was then assessed. A Netzsch Pulse Thermal Analyzer was used to inject a volume of 50 ppm anhydrous NH_3(g) (99.995%) into the STA chamber at a pulse rate of 0.5 mL/s. The NH_3(g) was pulsed in continuously in 1 mL increments until constant TG/DSC signals were obtained. The pulses lasted for approximately 45-60 min during which time 1350-1800 mL of NH_3(g) was delivered. The FTIR was used to monitor the injections of NH_3(g), and the FTIR cell was kept at 200 °C to prevent condensation of exit gases. Sorption experiments were conducted at 25, 50 and 60 °C at a heating rate of 5 °C min^{-1}. When sorption was carried out at 25 °C, sorbents were first cooled to 25 °C, until TG/DSC signal stabilization occurred such that mass and heat flow changes were no longer detected. For sorption experiments at 50 or 60 °C, the 24 h isothermal step from pretreatment was extended for the duration of pulsing. After completion of sorption, desorption was initiated by removing the pressure of NH_3(g) from the carrier gas stream, and data collected until no mass and heat flow changes of the sorbate-sorbent complex were detected by TG/DSC. Select samples were also desorbed by temperature ramp up to 100 °C using variable heating rates (5, 10, 20 °C min^{-1}). All curves generated from the STA-PTA-FTIR experiments were analyzed using Netzsch Proteus Thermal Analysis (TA) software version 6.1.0. The Proteus TA software was used to analyze TG mass changes over time, integrate DSC data and isolate peaks in DTG curves. Experiments were conducted in duplicate. Mass change and enthalpy data were reported as the average of the two datasets with significant figures within the measurement resolution of ±0.1μg for TG and <1μW for DSC. The uncertainty of these results was expressed as the standard deviation (SD) of replicate measurements.

4.2.4. Kinetic Analysis.

Kinetics of NH_3(g) sorption-desorption with S15-150, S35-150, BC, and MOF sorbents was determined. These sorbents were selected because of their higher uptake capacities compared to the other tested sorbents (unheated S and all D sorbents). Data from isothermal sorption at 25, 50, 60 °C and desorption up to 100 °C, at 5, 10, 20 °C min^{-1} rates were used to determine kinetics. The TG curves obtained from isothermal sorption and dynamic desorption were analyzed by two approaches, Friedman analysis and a simple kinetic model, to determine kinetic parameters such as apparent activation energy (Ea) and preexponential factor (A). The Ea describes the minimum energy needed for the reaction to proceed, while A is a term which includes factors such as frequency of collisions.

In thermal analysis, the rate is described by:

$$\frac{d\alpha}{dt} = k(T)f(\alpha) \tag{4.1}$$

The two variables indicate the rate of reaction (k) depends on temperature (T) and the extent of conversion ($f(\alpha)$) (Equation 4.1). Where conversion is related to the degree of completion of a reaction [Vyazovkin et al., 2014], the conversion in this study is defined as the extent of TG mass change during sorption-desorption reactions. The Friedman analysis is a model-free method, which requires a minimum of two measurements with different heating rates or different isothermal measurements to find Ea and A for sorption, without any assumptions about the reaction model [Vyazovkin et al., 2014]. This is an isoconversional method [Friedman, 1964; Ozawa, 1965; Flynn and Wall, 1966] that states the rate of reaction at a constant conversion (α) is solely a function of temperature (T) [Vyazovkin et al., 2011; Adnadevic et al., 2007]. Friedman analysis therefore defines

kinetic parameters at specific steps in a multi-step reaction. The Ea and A values are calculated from the slope and intersect of isoconversional lines of α from an analysis plot of conversion rate (log dx dt^{-1}) vs inverse log temperature (T).

By contrast, a simple kinetic model was created to describe the overall reaction. This model-based analysis was used to determine the kinetics of the entire sorption or desorption reaction and was performed under three assumptions of a kinetic model for the process. Concisely put, these assumptions state the reaction consists of several elementary reaction steps, each with its own reaction rate, all kinetic parameters remain constant during the reaction progress and the TG signal is equal to the total sum of the signals of the single reaction steps. The multistep reactions necessitated the use of multistep software which use non-linear regression methods to optimize the kinetic parameters. Reaction rate k, as a function of temperature can subsequently be calculated using Arrhenius' equation. The Arrhenius equation defines the temperature dependence of the rate constant

$$k(T) = \mathrm{A}\exp\left(\frac{-Ea}{RT}\right) \tag{4.2}$$

where A is the pre-exponential factor, R is the universal gas constant and Ea, the activation energy. All kinetic analysis was performed using Netzsch Kinetics Neo Software, version 2.1.2.2.

4.3. Results and Discussion

4.3.1. Sorbent Characteristics

4.3.1.1. X-ray diffraction

The mineralogy of the original SWW and DWW (unheated) solids was previously determined by XRD [47]. To assess any changes to the solid mineralogy, for example degradation over time (6 months) at room temperature, diffraction patterns for the unheated S and D sorbents were collected again in this work (Fig. 4.S1). When compared to the original XRD patterns from Rabinovich et al., 2018 there were no significant changes to the mineralogy of the substrates (Fig. 4.S1). The XRD patterns for S and D sorbents before and after heat treatment at 150 and 300 °C were compared (Fig. 4.1a-d). After heating S15 and S35 to 150 and 300 °C, broad diffraction peaks were observed (Fig. 4.1a-b). These results suggest an amorphous phase formed at both temperatures, and the S solids did not maintain a coherent mineral structure, losing crystallinity after heating despite higher initial crystallinity compared to D sorbents. From a previous work, it was reported diffraction peaks for dittmarite, ($MgNH_4PO_4{\cdot}H_2O$), appeared after thermal decomposition of commercial struvite (Alfa Aesar 98%) at 150 °C [Ramlogan and Rouff, 2016]. When compared to a dittmarite reference (Fig. 4.S2), no major peaks for dittmarite were found in either S or D sorbents recovered after heating to 150 °C. For the S sorbents which were characterized as almost pure struvite [Rabinovich et al., 2017], impurities (organics) and the presence of other minor phases (K-struvite) most likely changed the thermal decomposition [Ramlogan and Rouff, 2016] of the recovered S solids. Furthermore, the S samples were recovered from a complex, non-model system as mostly pure struvite with extraneous constituents, while commercial struvite is >99% pure with chemical treatments (stabilizers) added, which may explain why a decomposition pathway leading to dittmarite formation was not observed for S sorbents.

Diffraction patterns for commercially acquired struvite and calcite (Fig. 4.S2) were used to identify major peaks for these minerals in D sorbents. For both D35 and D68, peaks attributed to struvite (15.6, 16.0, 20.6) diminished considerably at 150 °C or disappeared. For example, the peak at 15.6 was reduced significantly in the D35-150 solids (Fig. 4.1c) and missing in the XRD pattern for D68-150 (Fig. 4.1d). After heating to 300 °C, the D35 and D68 XRD patterns (Fig. 4.1c-d) closely matched the XRD pattern for calcite (29.6, 48.4) (Fig. 4.S2). This indicated thermal decomposition of struvite at 300 °C, consistent with previous research [Ramlogan et al., 2018; Ramlogan and Rouff, 2016], leaving calcite which thermally decomposes between 635-800 °C [Halikia et al., 2001]. The D sorbents therefore retained some crystallinity due to residual calcite. A peak at 47.5 associated with monohydrocalcite was not detected at 300 °C in the D35 solids indicating monohydrocalcite (47.5) underwent thermal decomposition with subsequent volatilization of structural H_2O(s) [Neagle and Rochester, 1990].

4.3.1.2. Vibrational spectroscopy

The FTIR spectroscopy data of unheated and heated S and D sorbents were compared (Fig. 4.2a-d). In general, the FTIR data for unheated S15 and S35 solids closely matched struvite [Ramlogan and Rouff, 2016; Rouff and Juarez, 2014]. The peaks located at ~1000 cm^{-1} were attributed to the ν_3 PO_4^{3-}(s) vibrational mode [Ramlogan and Rouff, 2016; Rouff and Juarez, 2014]. Shifting of the peaks in this region to slightly higher wavenumbers (~1035 cm^{-1}) with temperature (Fig. 4.2a-b) is most likely due to structural defects brought about by thermal degradation of the S sorbents [Ramlogan et al., 2018;

Ramlogan and Rouff, 2016]. The peak at 1430 cm^{-1} assigned to ν_4 NH_4^+ vibrations [Rabinovich et al., 2017] (Fig. 4.2a-b) weakened at 150 °C and was absent at 300 °C for both S sorbents (Fig. 4.2a-b). The ν_2 H_2O bending vibrations located at 1600 cm^{-1} [Piatkowski and Bakker, 2011; Makreski et al., 2019] and H_2O overlapping asymmetric ν_3 and symmetric ν_1 stretching vibrations at ~2300-3100 cm^{-1} [Madejova et al., 2002] are due to waters of crystallization. The vibrations for H_2O at ~2300-3100 cm^{-1} decreased with heat-treatment due to evolution of waters of crystallization as $H_2O(g)$ (Fig. 4.2a-b). Therefore, the FTIR result agreed with XRD patterns which showed unheated S samples were mainly struvite that subsequently degraded to an amorphous phase, releasing both $NH_3(g)$ and $H_2O(g)$, after thermal treatment.

The effect of heat on the ν_3 antisymmetric band of PO_4^{3-} (~1012cm^{-1}) in the D35 (Fig. 4.2c) sorbents was not significant with a slight lowering in intensity observed. In contrast, for the unheated D68 sorbent, the sharp ν_3 antisymmetric band of PO_4^{3-} decreased with temperature and slight broadening in the curve was observed (Fig. 4.2d). The peaks for ν_3 CO_3^{2-} (s) vibrations are located at ~873 cm^{-1} and between 1400-1486 cm^{-1} (Fig. 4.2c-d). In D35 solids, the split ν_3 CO_3^{2-} (s) peak appeared since this substrate had the highest monohydrocalcite percentage (42%) [Rabinovich et al., 2018]. The CO_3^{2-} (s) bands increased in intensity with temperature as thermal decomposition of struvite led to a stronger response in the ν_3 CO_3^{2-} (s) regions. The $H_2O(s)$ vibrations located around 1650 and 3150 cm^{-1} [Madejova et al., 2002] are also weakened at 150 °C and absent at 300 °C due to volatilization at that temperature. The ν_3 CO_3^{2-} (s) bands are essentially unaffected at 150 °C in D68 but the split peak resolved to a single peak at 300 °C (Fig. 4.2d). The results from ATR-FTIR showed changes to functional groups occurred with thermal

treatment. The functional groups in the sorbents determine the number of active sites available for NH_3(g) sorption. A past study reported the chemisorption of NH_3(g) on dehydroxylated sites occurred when one molecule of NH_3(g) substituted one molecule of desorbed H_2O(s) [Nagao and Morimoto, 1976]. Therefore, removing H_2O(s) from the sorbent structure via heat treatment (150, 300 °C), and subsequently sorbed H_2O(g) during pretreatment (40 °C) prior to sorption could promote NH_3(g) uptake [Ramlogan et al., 2018; Nagao and Morimoto, 1976].

4.3.1.3. Morphology characterization

The SEM images for surface characterization of select S and D sorbents after heating (150 °C) (Fig. 3) are compared to the original SWW and DWW unheated solids [Rabinovich et al., 2018] (Fig. 4.S3). The SWW solids appeared to have characteristic crystal habit for struvite, with homogenous surfaces [Rabinovich et al., 2018] (Fig. 4.S3). In line with the amorphous phases observed by XRD (Fig. 4.1), crystal faces, and smooth homogenous surfaces were largely absent in the heated S sorbents. The heated S surfaces appeared irregular, with heterogenous pores, cracks, edges and pitting (Fig. 4.3a, b). Most likely such distortions lead to an uneven distribution of reactive sites. The observed changes in morphology are caused by thermal decomposition and evolution of volatiles from the S sorbents.

The original DWW solid surfaces were compact, irregular, and lacking any crystalline habit (Fig. 4.S3). For the heated D sorbents, smooth, dense surfaces surrounded by uneven regions were evident (Fig. 3c, d), but alteration of the surface was not as distinct

when compared to the original unheated solids. The SEM images confirmed structural defects were present in the heated sorbents which could enhance sorption processes, for example by condensation into pore space [Peel et al., 1981; Harding et al., 1998].

4.3.2. Sorption Experiments

4.3.2.1. Pretreatment

Prior to sorption reactions, sorbents were thermally pretreated to enhance sorption capacity. The TG mass loss due to pretreatment at 40 °C ranged from 0.27- 4.2 % (Table 4.1). This mass loss was attributed to volatilization of surface-bound species [Ramlogan et al., 2018], including atmospheric gases, and most likely led to an increase in the availability of active sorption sites [Linares-Solano et al., 1998]. For the S and D sorbents, the outgassed mass decreased with increasing initial heat treatment (Table 4.1). Endothermic transitions (5.0–37.1 J g^{-1}) recorded simultaneously by DSC accompanied the sorbent outgassing (Table 4.1) and are indicative of bond breaking and desorption.

4.3.2.2. Sorption Capacity

Sorption of NH_3(g) was evaluated for struvite (Fig. 4.S4), calcite (Fig. 4.S5), and all effluent-derived (S, D) sorbents (Fig. 4.S6ab) after continuous injections of NH_3(g) by STA-PTA-FTIR. Sorption capacities of all tested sorbents (Table 4.1) were directly obtained from the mass change in the TG curves. The isothermal TG profiles are comprised

of three regions representing different rates of uptake (mass change % min^{-1})): a rapid mass increase, a slower mass increase, and a flattening in the curve (Fig. 4.S6). The initial rapid mass increase was attributed to physical adsorption [Ramlogan et al., 2018], the region of slower mass increase was due to a decrease in the ratio of available to filled sorption sites, and flattening of the curve indicated no further uptake due to saturation of available sites. The lowest uptake of NH_3(g) was observed for struvite (4.1 mg g^{-1}) (Fig. 4.S4), and calcite (3.2 mg g^{-1}) (Fig. S5). The sorption capacities for S and D solids ranged from 9.9 to 49.9 mg NH_3 g sorbent $^{-1}$ (Table 4.1). The S15-150 and S35-150 sorbents had the highest overall uptake of the S and D solids at 47.2 and 49.9 mg g^{-1} respectively, comparable to BC at 50.8 mg g^{-1} (Table 4.1). The MOF sorbed the highest mass of NH_3(g) (289.7 mg g^{-1}) (Table 4.1).

The DTG profiles for sorption reactions were obtained by taking the first derivative of the TG curves as a function of time (Fig. 4.S7). The maximum uptake rate determined from the maxima in DTG curves (Fig. 4.S7) ranged from 0.0–0.9 mg min^{-1} (Table 4.1) and always occurred during the initial rapid mass increases. More frequent collisions between NH_3(g) molecules and available sorption sites occurred in the initial stages of sorption. In general, the fastest rates (DTG peaks) of sorption coincided with the highest uptake of NH_3(g) which was an indication of affinity of the sorbents for NH_3(g).

With respect to mineralogy, the original SWW solids were >90% struvite and the sorption behavior of the heated S sorbents were similar to previous work that showed heating struvite to 150-300 °C increased uptake of NH_3(g) by these substrates [Ramlogan et al., 2018]. The uptake of NH_3(g) by unheated D sorbents was ~4-5 times greater than struvite and calcite. The unheated D sorbents also captured ~2 times more NH_3(g) than the

unheated S sorbents, and half that of BC. The high degree of crystallinity and homogeneous composition of the unheated S sorbents [Rabinovich et al., 2018] most likely resulted in less active binding sites compared to the heterogeneous unheated D sorbents. Heat treatment of D sorbents resulted in a marginal increase in uptake at 150 °C, and a decrease in uptake at 300 °C compared to the unheated D sorbents. Calcite reacted weakly with NH_3(g) (Fig. 4.S5), therefore heat treatment of D sorbents produced only a marginal increase in sorption capacity because of the predominance of calcite (Fig. 4.1). The S sorbents heated to 150 °C had comparable sorption capacity to BC, which was produced at much higher temperatures. Using the S sorbents could therefore represent an energy savings alternative compared to biochar. It should be noted that although D solids sorbed less NH_3(g), the unheated D sorbents could be as effective as the heated S sorbents by increasing the mass of sorbent used, which also represents a cost-effective alternative to heating.

4.3.2.3. Sorption Energetics

The data collected by DSC was integrated to obtain enthalpy of the sorption processes over time by selecting the areas under the exothermic transitions (Fig. 4.S6ab). The affinity of the sorbents for NH_3(g) can be described by the values of the integrated exothermic transitions [Ramlogan et al., 2018]. Struvite (-4.1 J g^{-1}) and calcite (-3.1 J g^{-1}) had the lowest enthalpies recorded due to the low affinity for NH_3(g). For the S and D sorbents, the integrated exothermic adsorption enthalpies ranged from -21.4 to -131.0 J g^{-1} (Table 1) with the largest exothermic response observed for heated S sorbents (150, 300

°C). The sorption enthalpy was -117.5 J g^{-1} for BC, and -1041.1 J g^{-1} for MOF. The largest exotherms corresponded to the highest affinity for NH_3(g) based on the observed TG results. The lower sorption capacities observed for the D sorbents produced exothermic transitions that were ~2.5 times lower than those detected for S sorbents. In general, the enthalpy values suggested physisorption was the key sorption mechanism [Sexton and Hughes, 1984] driven by van der Waals forces, electrostatic interactions and pore condensation. However, for MOF, the DSC signal was approximately an order of magnitude greater than the other tested sorbents, indicating in addition to physisorption, chemisorption onto Cu sites may be a dominant mechanism [Vikrant et al., 2017].

The exothermic enthalpy values related to NH_3(g) sorption expressed as enthalpy per mole of NH_3(g) (J mol^{-1}) is shown in Table 2. These values are therefore contingent on the sorbing molecule ($NH_{3(}$g)) as opposed to the sorbent. The magnitude of enthalpy for the heated S sorbents (-44640.7 to 47527.2 J mol^{-1}) was attributed to strong hydrogen bonding for example between the electronegative N atom of NH_3(g) and hydrogen atoms in hydroxyl groups. These values were larger as compared to the heated D and BC sorbents and signified a stronger interaction for the S sorbents. Similar enthalpy values (-47420 J mol^{-1}) were reported for NH_3 bonding to hydroxyl functionalized ionic liquids [Li et al., 2015]. The larger enthalpy for MOF (-61236.5 J mol^{-1}) was due to weak chemisorption to Cu groups. Overall, these enthalpy values indicated the sorption process could be regarded as physical and chemical sorption [Gu et al., 1994].

4.3.2.4. Temperature-Dependent Sorption

To determine sorption capacity of NH_3(g) at temperatures relevant to environmental conditions, for example, during thermophilic composting, sorption experiments were repeated at 50 and 60 °C for sorbents with highest uptake (S15-150, S35-150, BC, MOF). For all sorbents, sorption of NH_3(g) was reduced at 50-60 °C relative to 25 °C (Table 4.2). In comparison with the data obtained at 25 °C, lower sorption capacities and heats of adsorption were expected because sorption is a spontaneous process and the gas-solid reactions studied here are exothermic. From Le Chatelier's principle, exothermic reactions shift to the reactant side when reaction temperatures are increased. More reactants should remain at increased temperatures during exothermic reactions, therefore less NH_3(g) is removed and lower uptake capacities were observed at the elevated reaction temperatures compared to 25 °C (Fig. 4.S8). Though sorption of NH_3(g) with MOF was highest at all temperatures, increased temperature had the most pronounced effect on sorption capacity of this sorbent, with a 44% decrease in uptake from 25 to 60 °C. For BC the amount of sorption decreased by 39% at higher temperature, and the absolute amount of sorbed NH_3(g) was lower (31-32 mg g^{-1}) than that of S sorbents (37-42 mg g^{-1}). In this respect the S sorbents exhibited more favorable sorption at higher temperatures than both MOF and BC, with only a 16-22% decrease in sorbed NH_3(g) at elevated temperatures, and higher values of sorbed NH_3(g) than BC.

4.3.2.5. Sorption Mechanisms and Binding Sites

Greater affinity for NH_3(g) by the heated S sorbents compared to the unheated S sorbents was observed (Table 4.1). A change in the vibrational mode at ~1450 cm^{-1} for

NH_4^+(s) is evident for SW15-150, and SW35-150 solids (Fig. 4.4a, b). This may be due to sorption of NH_3(g) by hydrostatic interactions, and hydrogen bonding [Ramlogan et al., 2018] resulting in protonation of NH_3(g). The appearance of absorption bands at ~1450 cm^{-1} NH_4^+(s) (Fig. 4.4a, b) confirmed the formation of NH_4^+(s) on the sorbent surface [Morimoto et al., 1976] which caused a change in the N moiety from gas to solid. Lowered intensity in the vibrational mode at 1650 cm^{-1} for H-O-H bending was detected; since the sorbents were heat-treated prior to sorption, the decreased IR response was likely due to NH_3(g) binding via hydrogen bonding, and not water displacement.

The BC spectra collected before and after sorption exhibited differences in some absorbance regions, used to infer which functional groups were participating in the sorption process. The absorbance band at 3100-3500 cm^{-1} corresponded to the stretching vibration of hydroxyl (-OH) [Zhang et al., 2017] in the unreacted BC sorbent (Fig. 4.4c). Variations were observed in this band (-OH vibration) after reactions with NH_3(g) (Fig. 4.4c), likely due to sorption reactions occurring at this site [Yin et al., 1999]. Consistent with this interpretation, a small peak developed around 2900 cm^{-1} that could be attributed to N-H stretching modes of NH_4^+(s) ions [Larrubia et al., 2000], as well as a small band at ~1430 cm^{-1} due to protonation of NH_3 [Yin et al., 1999] (Fig. 4.4c).

The FTIR spectrum for the unreacted MOF sorbent displayed vibrational modes at 728, 757, 939, 1111, 1373, 1451 and 1652 cm^{-1} (Fig. 4.5d). The sharp peaks at 728 and 757 cm^{-1} were assigned to C-C ring out-of-plane bending, while the bands at 939 and 1111 cm^{-1} were due to C-H out-of-plane and in-plane bending, respectively [DeCoste et al., 2013]. The stretching modes of the MOF carboxylate groups were assigned to 1373, 1451 cm^{-1} (symmetric stretch). The band at 1652 cm^{-1} for unreacted MOF is assigned to the

carboxylate (-COO) asymmetric stretch where the carboxylate ion is coordinated to two Cu ions. [DeCoste et al., 2013; Dhumal et al., 2016]. After sorption the C-C bands (728 and 757 cm^{-1}) remained unchanged indicating these sites were not available for binding NH_3(g). However, the C-H bands located at 939 and 1111 cm^{-1} disappeared, likely due to chemisorption of NH_3(g) at C-H sites. Similarly, the bands at 1373, 1451 and 1652 cm^{-1} were no longer observed due to protonation with NH_3(g) sorption to the carboxylate groups. A new peak at 1330cm^{-1} is indicative of C-N bond formation (aromatic amine) [Balabanovich et al., 2004] due to NH_3(g) coordination. Also, new peaks were observed around 1432 cm^{-1} (N-H bending), and 1605 cm^{-1} (coordinated NH_3(s)), while the development of a broad band centered around 3250 cm^{-1} was attributed to the N-H stretch of coordinated NH_3(s)) [Larrubia et al., 2000]. Overall, the various stretching and bending deformations observed after sorption was indicative of the formation of multiple coordinated species [Larrubia et al., 2000] by electrostatic interactions and chemisorption.

4.3.2.6. Reversibility of Sorption

The mass of NH_3(g) removed i.e. the reversible fraction, during the desorption step is also indicative of sorption mechanism. The percent NH_3(g) desorbed ranged from 18.8-100% for all tested sorbents (Fig. 4.5). In general, the reversible fraction of NH_3(g) was physisorbed while the sorbate remaining after desorption represented the chemisorbed fraction. For S and D sorbents, the mass of sorbate remaining after desorption generally increased with initial temperature treatment. However, S15-300 retained less sorbate than S15-150 (Fig. 4.5) suggesting less favorable binding sites at higher temperature. The

sorbate mass after desorption was greater for S15-150 and S15-300 sorbents compared with BC and lower than MOF. For the D sorbents, physisorption is likely the dominant mechanism due to the large reversible fraction of NH_3(g). The irreversibly sorbed fraction may include binding of NH_3(g) to metal sites such as Fe and Zn, as has been observed for NH_3(g) sorption with zinc oxides [Morimoto et al., 1976]. Since the Fe and Zn concentrations in D sorbents are ~5-10 times greater than those for S sorbents (Table 4.S1), these metals may have served as active sites for NH_3(g) [Donstova et al., 2005]. Additional sorbate retention was likely facilitated by condensation into pores and pits detected by SEM on the surfaces of S and D sorbents heated to 150 °C (Fig. 4.3).

4.3.4. Kinetics Analysis

4.3.4.1. Model-dependent Kinetics

The TG data for selected sorbents (S15-150, S35-150, BC, MOF) reacted with NH_3(g) at 25, 50 and 60 °C was analyzed using Netzsch Kinetics Neo software. A simple kinetic model was developed to determine Ea and A based on an n^{th} order reaction type (Table 4.3). The S15-150 (13.4 kJ mol^{-1}) and MOF (13.3 kJ mol^{-1}) sorbents had equivalent and smallest Ea values, indicating lowest energy barriers to sorption. Since Ea was comparable, but the absolute amount of sorption was notably different, the extent of sorption was not influenced by Ea but by type and availability of reactive sites. The S35-150 sorbent had the highest Ea and lowest amount of sorption, but sorption amount was close to BC and S15-150. The log A values (log (1 s^{-1})) were also similar for S15-150 (-

0.8) and MOF (-0.6) but differs slightly for S35-150 (4.8) and BC (1.9). According to Table 4.3, decreasing Ea also decreased log A, due to compensation effect between Ea and Log A. The mutual dependence of Ea and log A was attributed to physico-chemical parameters such as bonding energy, and multiple active sites leading to multiple reaction pathways.

The TG data from the desorption step was used to model kinetic parameters from non-linear regression analysis (Table 4.3). The Ea was lowest for MOF (0.08 kJ mol^{-1}) indicating a low energy barrier for desorption. Since water enhances interactions between MOF and NH_3(g) [Borfecchia et al., 2012; Nijem et al., 2015], when MOF was reacted with NH_3(g) in the absence of humidity under dry N_2 (g) atmosphere, minor interaction occurred. The model indicated desorption Ea was highest for S35-150 (41.6 kJ mol^{-1}) and BC (47.9 kJ mol-1). The determined desorption Ea values are a composite of multiple reaction pathways [Vyazovkin et al., 2014], including deprotonation of NH_4^+(s), removal from reversible binding sites and evaporation from pore space.

4.3.4.2. Model-Independent Kinetics

Temperature-dependent sorption data collected isothermally at 25, 50 and 60 °C was used to determine kinetics of sorption for the sorbents with highest NH_3(g) uptake (S15-150, S35-150, BC, MOF). The model-independent Friedman method [Friedman, 1964] was applied to determine Ea (Fig. 4.6a-d) and A (Fig. 4.S9a-d) at various points of α, i.e., extent of sorption ranging from 0-0.99. A representative analysis plot using sorbent S15-150 is shown in Fig. S10. Compared to the model-dependent analysis, the Friedman method is useful for determining Ea at various steps in the reaction but is less accurate and

reliable for determining overall kinetic parameters. Therefore, a direct comparison cannot be made between the Friedman and the model-dependent analysis.

The overall shape of the Ea and A curves was the same for each sorbent; as Ea increased or decreased, A also changed in a similar way. Peaks in the Ea curves represent reaction steps. While the model calculated single Ea values, the apparent Ea values by Friedman are most likely derived from the energy barriers of individual steps, thus negative values can be observed [Vyazovkin et al., 2014]. The apparent Ea values derived from individual steps are not error free (Fig. 6) because they are experimentally determined and can deviate from real values of an individual step primarily due to the presence of parallel and independent reactions which are likely occurring during sorption. The inflection points observed in the Ea curves (Fig. 4.6) were likely caused by different steps, for example rate limiting steps. Of note, although sorption DTG curves (Fig. 4.S7) show a single peak, the kinetic analysis discovered the multistep reactions which occurred.

In general, for the selected sorbents, increases in energy barriers were likely due to rate limiting steps towards the end of the reactions. The decreasing availability of active binding sites with sorption increased Ea and therefore also lowered the frequency of collision. Overall, the effect of degree of sorption on the determined values of the effective Ea for the selected sorbents was a result of rate limiting steps, the distribution of the sorption sites and concomitant Ea values across the sorbent surfaces and attractive or repulsive sorbate interactions.

The Ea at conversion 0 represents the initial energy barrier to sorption. This value is contingent upon the sorbent, with negative values indicating low energy barriers and positive values indicating high energy barriers. Biochar had lowest initial Ea (-19.9 kJ mol^{-}

^{1}) followed by S15-150 (-4.2 kJ mol^{-1}), however these values also had high error. High error occurs since the Friedman analysis cannot provide accurate Ea values for parallel and competitive reactions. Both S35-150 (15.5 kJ mol^{-1}) and MOF (36.9 kJ mol^{-1} had positive initial Ea values, with MOF exhibiting the highest value. High positive Ea for MOF may be due to incomplete pretreatment and reactions in the absence of water, whereas BC was sufficiently activated to facilitate sorption. Initial Ea did not influence the extent of sorption as MOF had highest sorption in spite of the high initial energy barrier.

After overcoming the initial Ea, the reaction proceeds. For S15-150 and S35-150, three and four peaks are observed in the Ea curves respectively (Fig. 4.6a,b). The general shape of each curve is indicative of multiple-step reactions [Vyazovkin et al., 2014]. For the S15-150 sorbent, Ea increased at α=0.14 (3.9 kJ mol^{-1}), α=0.75 (9.1 kJ mol^{-1}) and α=0.98 (32.6 kJ mol^{-1}). For S35-150 at α=0.87, Ea (1.3 kJ mol^{-1}) was lower than α=0.78 (5.2 kJ mol^{-1}) suggesting competing reactions with Ea > 5.2 kJ mol^{-1} at α= 0.3 (Fig. 4.6b). Though these are similar substrates, these changes in Ea or reaction steps occur at different points of conversion. Although the S15-150 and S35-150 sorbents were derived from mineralogically similar substrates, the kinetic parameters describing their reactions with NH_3(g) were different. These differences could be attributed to variations in initial crystallinity and minor variations in the mineral phases comprising the original, unheated S35 (calcite, K-struvite) and S15 (K-struvite) solids. In addition, heat-induced crystalline phase transformations to amorphous phases likely enhanced variability between the S35-150 and S15-150 sorbents with respect to active binding sites available for reactions.

For BC, a minimum of four reaction steps were observed (Fig. 4.6c) likely due to multiple available binding mechanisms, for example hydrogen bonding and pore

condensation. In contrast, the shape of the curve for the MOF indicated at least two reaction steps (Fig. 4.6d) since sorption was limited to reactions with Cu(II) sites, as opposed to multiple reactive sites. In general, for the selected sorbents, there was an increase in the energy barriers as sorption sites were filled towards the end of the reactions.

The kinetic parameters describing the desorption of NH_3(g) from selected sorbents calculated by Friedman analysis were performed using TG data obtained after heating the selected sorbates originally reacted with NH_3(g) at 60 °C, under three different heating rates to a final temperature of 100 °C (Fig. 4.S11). The apparent Ea for the S15-150 solid (-1.9×10^4 to 6.4×10^4 kJ mol^{-1}) and BC (-6.5×10^3 to 9.5×10^3) were several orders of magnitude larger as compared to S35-150 and MOF. The apparent Ea throughout the extent of desorption ranged from -49.3 to -16.4 kJ mol^{-1} for S35-150. An Ea range of -20.9 to 17.8 kJ mol^{-1} was calculated for the MOF. The activation energies for desorption were most likely dependent on the binding mechanism, affinity for active sites, and overall reactivity between sorbent and sorptive. For S15-150 and BC, sorbate interacting with pore spaces, or chemisorbed fractions may have resulted in higher calculated Ea values for these sorbents.

4.3.4.3. Kinetics of NH_3(g) Sorption-Desorption

The Ea and A values from the model-dependent data were used to determine the temperature-dependent rate constant (k) from the Arrhenius rate equation (Eq. 4.2). This data was used because the model-dependent predictions based on non-linear regression analysis of the TG data provides a single Ea for the entire reaction. The model-independent

analysis determines Ea at various points of conversion, has low accuracy, and therefore is less reliable for determining overall kinetic parameters. The value for k was calculated at 25 °C only, but can be determined for other temperatures of interest, and in general will increase with increasing temperature. For sorption, k for S15-150 (7.1×10^{-4} s^{-1}) and BC (6.6×10^{-4} s^{-1}) were comparable. The fastest reaction rate was observed for S35-150 (1.1×10^{-2} s^{-1}) which is 2 orders of magnitude greater than S15-150 despite similarities in parent material and uptake capacity, and an order of magnitude greater than MOF (1.2×10^{-3} s^{-1}). For desorption (Table 4.3), the smallest k was calculated for S35-150 (8.2×10^{-5} s^{-1}) which was an order of magnitude lower than k for S15-150 (8.6×10^{-4} s^{-1}) followed by MOF (4.9×10^{-4} s^{-1}), and BC (3.2×10^{-4} s^{-1}). For S15-150 an S35-150, the inverse relationship between Ea and k is observed.

5. Conclusion

The potential of S and D solids reclaimed from livestock wastewater as alternative sorbents for NH_3(g) has been investigated and compared to conventional BC and MOF sorbents. Thermal data for sorption-desorption of NH_3(g) was collected by STA-PTA-FTIR. Kinetic parameters describing sorption-desorption including Ea and log A could be determined from the experimental STA-PTA information. Of the S and D sorbents, the S sorbents heated to 150 °C showed superior uptake and was comparable with BC. Significant energy demands during pyrolysis production of BC (>400 °C) is greater than heat treatment (150-300 °C) of the effluent-recovered sorbents. Therefore, using S and D sorbents represent energy-saving, low-cost alternatives that also promote wastewater

valorization. The enhanced sorption capacity observed for S sorbents after heat treatment was likely due to increased surface defects (pores, pits), and availability of active sorption sites (functional groups) for physisorption by van der Waals forces, electrostatic interactions, hydrogen bonding and chemisorption.

Energetics information confirmed sorption and desorption of $NH_3(g)$ was characterized by a single exothermic and endothermic transition respectively, where the magnitude of the exotherm was related to affinity of the sorbent for $NH_3(g)$. For sorbents reacted with $NH_3(g)$ at elevated temperatures, a decrease in sorption with increasing reaction temperature was observed. Model-independent analysis by Friedman method showed a distinct correlation between Ea and log A and indicated concurrent and parallel steps occurred. Although MOF had the highest sorption capacity, the reaction rate k was fastest for S35-150 from model-based kinetic parameters. This research provided important knowledge about the development of non-traditional sorbents but in general, further investigation is required to optimize sorption processes with novel sorbents. Combining the thermal and kinetics results provided a good picture of the sorbent-sorbate interactions. The main advantage for using STA-PTA-FTIR technique is the ability to quickly and efficiently collect crucial thermodynamic data in situ for a range of sorbent materials. The small standard deviations for duplicate measurements confirmed the accuracy and repeatability of this technique. Overall the findings here strongly support the potential use of original and heat-treated wastewater solids as sorbents for sequestering $NH_3(g)$.

Acknowledgements

This work was supported by National Science Foundation Grant No. EAR-1506653. The authors thank Dr. Evert Elzinga for use of XRD and FTIR.

Tables and Figures

Table 4.1 Data collected during sorption experiments (25 °C) by STA-PTA including pretreatment mass loss, sorption enthalpy, and total uptake. Standard deviations (SD) are given in parentheses.

Sorbents	Pretreatment Mass Loss (%)	Pretreatment Endothermic Transition ($J\ g^{-1}$)	Sorption Capacity ($mg\ g^{-1}$)	Uptake DTG Maxima ($mg\ min^{-1}$)	Sorption Enthalpy ($J\ g^{-1}$)	Sorption Enthalpy ($J\ mol\ NH_3^{-1}$)
struvite	1.7	7.2	4.1 *(0.5)*	0.1	-4.1 *(0.4)*	-17076.9 *(790.1)*
calcite	1.7	7.5	3.2 *(0.4)*	0.0	-3.1 *(0.1)*	-17194.0 *(2769.8)*
S15 (unheated)	3.2	12.3	9.9 *(1.4)*	0.3	-21.4 *(3.0)*	-33567.7 (*3252.2)*
S15-150	0.57	37.1	49.9 *(2.4)*	0.85	-130.9 *(8.5)*	-47275.3 *(3367.1)*
S15-300	0.37	27.4	37.5 *(1.6)*	0.8	-101.3 *(7.1)*	-47527.2 *(2092.3)*
S35 (unheated)	3.3	11.1	11.2 *(2.0)*	0.25	-22.0 *(1.8)*	-36837.1 *(157.5)*
S35-150	0.84	30.1	47.2 *(0.7)*	0.85	-131.0 *(7.5)*	-44640.7 (*737.6)*

S35-300	0.43	27.7	39.8 *(0.3)*	0.8	-111.1 *(5.7)*	-45951.5 (*1280.9)*
D35 (unheated)	1.77	29.3	22.7 *(0.2)*	0.35	-50.9 *(0.5)*	-36804.4 *(2557.3)*
D35-150	0.48	20.9	22.9 *(0.1)*	0.3	-49.7 *(0.5)*	-38187.7 *(2319.7)*
D35-300	0.46	19.7	16.4 *(0.4)*	0.35	-39.0 *(0.7)*	-41130.1 (*346.9)*
D68 (unheated)	1.6	20.8	18.8 *(0.6)*	0.45	-40.7 *(4.1)*	-38166.3 *(82.9)*
D68-150	0.66	18.2	20.6 *(1.9)*	0.45	-46.1 *(1.4)*	-36982.5 *(228.9)*
D68-300	0.35	13.9	14.0 *(0.7)*	0.3	-33.8 *(1.4)*	-41057.4 *(1704.0)*
BC	4.2	17.9	50.8 *(0.5)*	0.5	-121.3 *(2.7)*	-40066.4 *(1260.8)*
MOF	0.27	5.0	289.7 *(10)*	1.2	-1041.1 *(14.0)*	-61236.5 *(1283.0)*

TABLE 4.2 Temperature-dependent uptake of NH_3(g) (mg g^{-1}) after selected sorbent reactions, the respective sorption enthalpies (J g^{-1}) and the percent (%) decrease at 50 and 60 °C relative to sorption at 25 °C are given. Standard deviations (SD) are italicized and reported in brackets.

	T = 50 °C			T = 60 °C		
Sorbent	Sorption (mg g^{-1})	Decrease (%)	Enthalpy (J g^{-1})	Sorption (mg g^{-1})	Decrease (%)	Enthalpy (J g^{-1})
S15-150	38.9 *(3.3)*	22.0	-139.6 (*2.3)*	39.3 *(3.8)*	21.2	-135.3 (*8.1*)
S35-150	38.2 *(3.2)*	19.1	-120.5 (*2.9*)	36.1 *(1.1)*	23.5	-123.4 (*6.9*)
BC	30.6 *(2.1)*	39.8	-90.4 (*2.7*)	29.9 *(1.7)*	41.1	-85.9 (*0.3*)
MOF	184.4 *(18.8)*	36.3	-737.8 (46.3)	179.7 *(25.9)*	38.0	-845.5 (*84.1*)

Table 4.3 Kinetic parameters and rate constants (k) (sec^{-1}) by model-dependent analysis of TG sorption-desorption data.

Sorption				
	Ea (kJ mol^{-1})	Log A (log s^{-1})	Correlation R	k (s^{-1})
S15-150	13.4	-0.8	0.99997	7.1×10^{-4}
S35-150	43.3	4.7	0.99999	1.3×10^{-3}
BC	29	1.9	0.99995	6.6×10^{-4}
MOF	13.3	-0.6	0.99450	1.2×10^{-3}
Desorption				
	Ea (kJ mol^{-1})	Log A (log s^{-1})	Correlation R	k (s^{-1})
S15-150	9.5	-1.4	0.99997	8.6×10^{-4}
S35-150	41.6	3.2	0.99779	8.2×10^{-5}
BC	47.9	4.9	0.99995	3.2×10^{-4}
MOF	0.08	-3.3	0.99909	4.9×10^{-4}

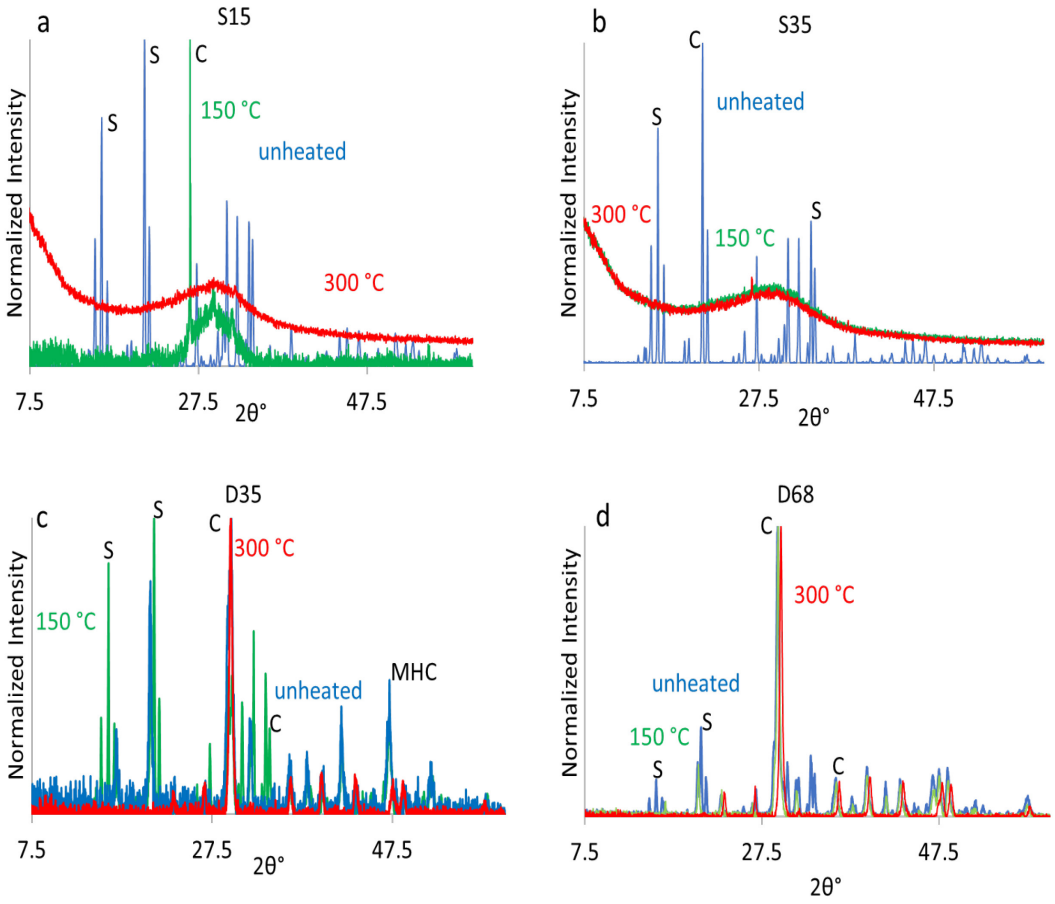

Fig. 4.1. XRD mineralogy comparison of unheated (blue) and solids heat-treated at 150 (green) and 300 °C (red) with major peaks for calcite (c) (29,36) and struvite (s) (21) labeled after comparison to reference reflections (Figure S2).

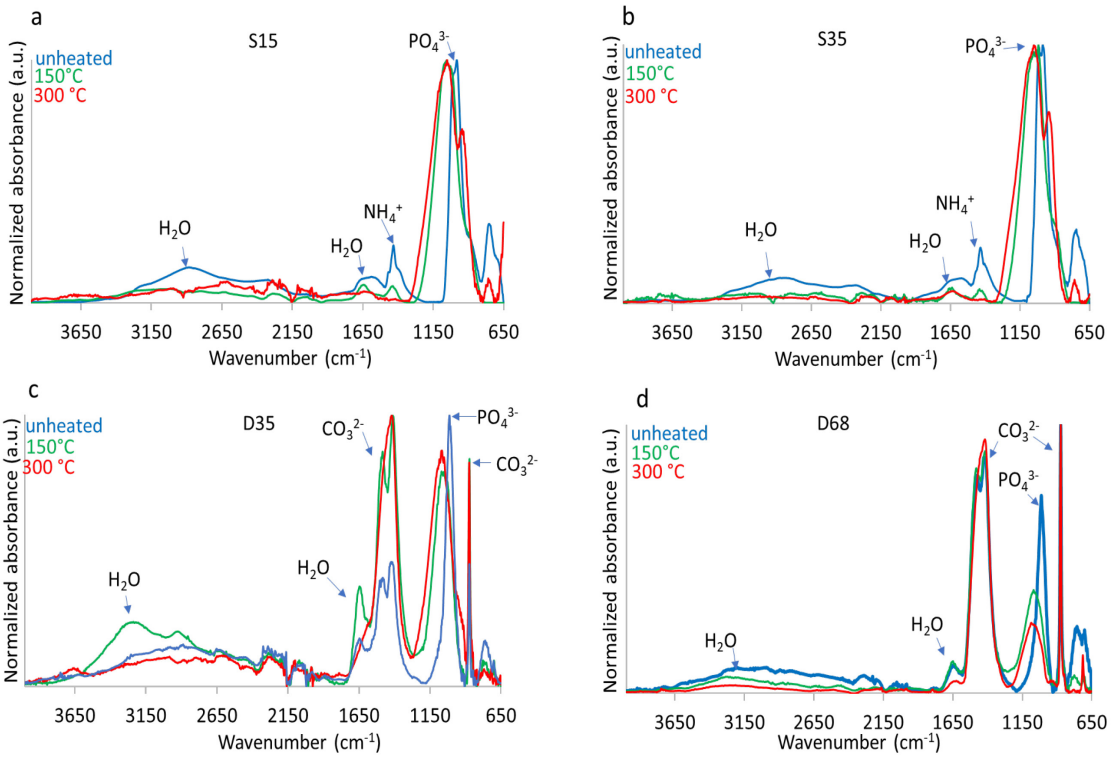

Fig. 4.2. The ATR-FTIR spectra for S (a, b) and D (c, d) solids before (blue) and after heat treatment (green, red). The relevant bands for PO_4^{3-}, (1012 cm^{-1}), CO_3^{2-} (~1450 cm^{-1}) and H_2O (~2800-3200 cm^{-1}) are plotted.

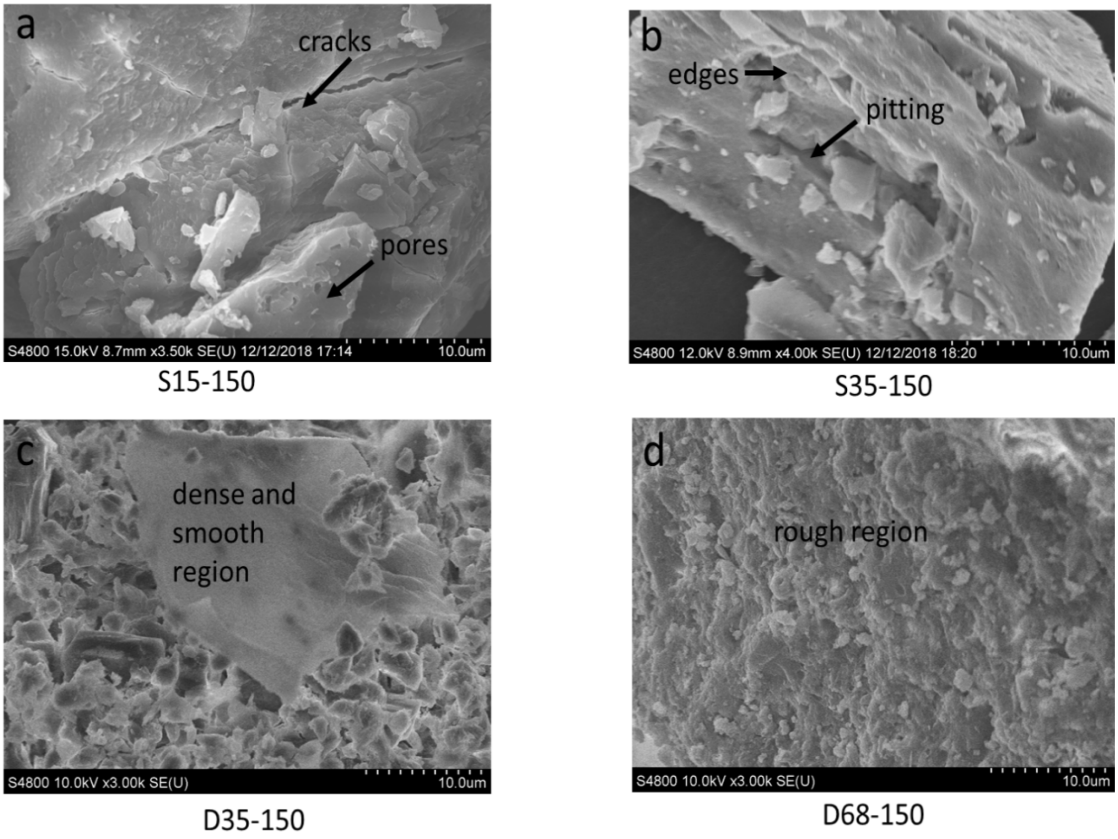

Fig. 4.3. SEM images of selected sorbents recovered from the furnace after heating at 150 °C. The scale bar at the bottom ranges from 1-10 μm.

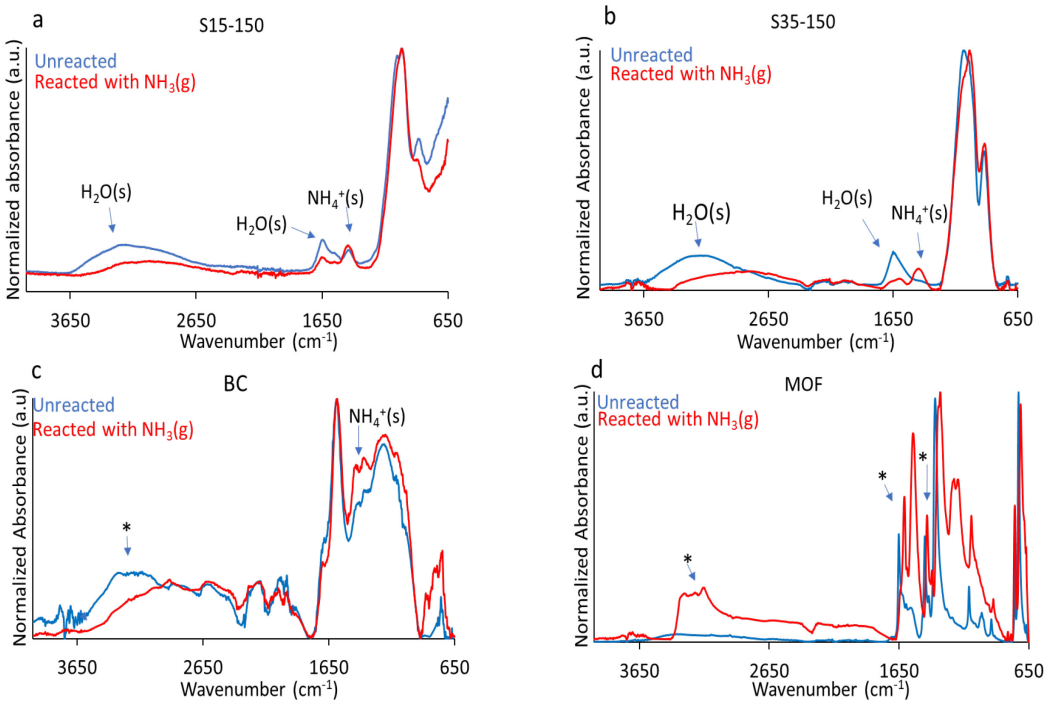

Fig. 4.4. The absorbance ATR-FTIR results for selected sorbents before and after reacting with NH_3(g) at 60 °C. The increase in absorbance after pulsing is shown near the region of the relevant band for NH_4^+ (~1450 cm^{-1}) (red). Perturbations in the H_2O(s) bending (~1650 cm^{-1}) and stretching modes (~2800-3200 cm^{-1}) are also shown. The regions where absorbance changed due to NH_3 coordination is shown with an *.

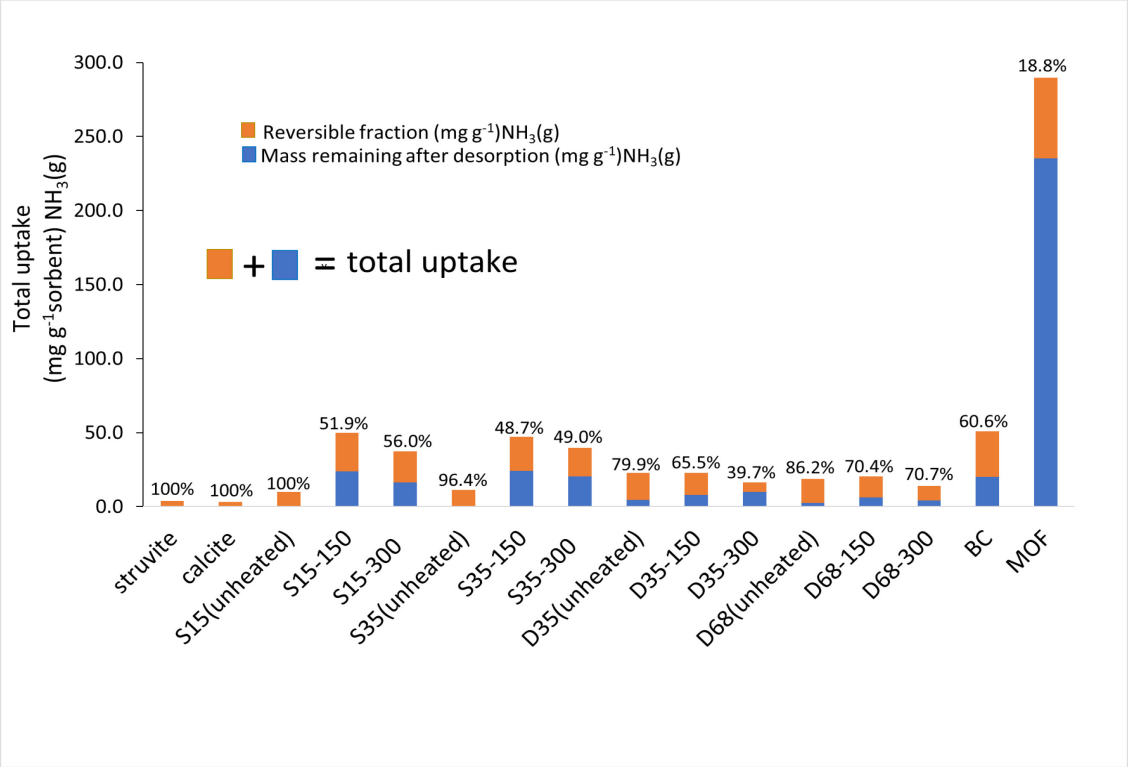

Fig. 4.5. The reversible sorbate (brown) and mass remaining (blue) for mineral phases (struvite, calcite), S and D solids, and BC and MOF reacted with NH_3(g) at 25 °C. The reversible fraction (%) is given.

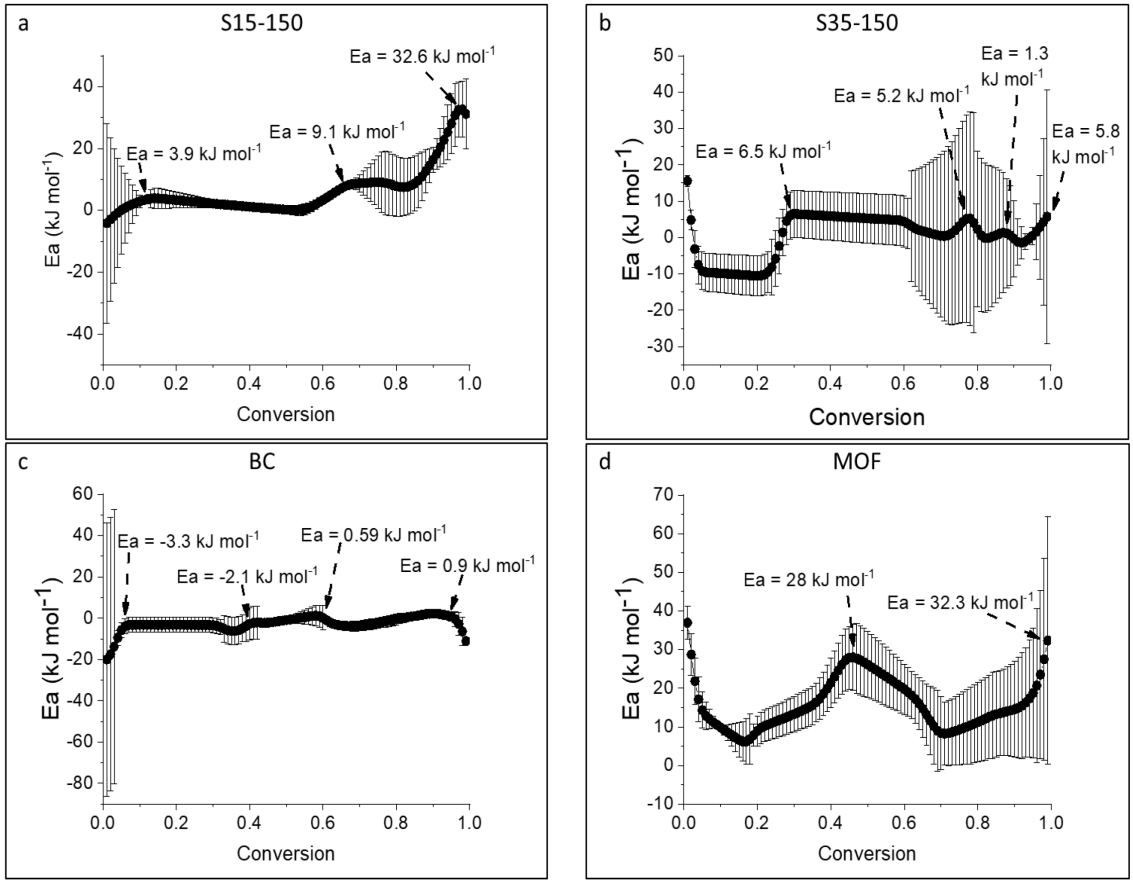

Fig. 4.6. The dependence of activation energies (Ea) (a-d) on the extent of sorption. The error on the Ea values is plotted as vertical lines.

Table 4.S1 Distribution of constituent metal ions, mineralogy and crystallinity for original solids used as S and D sorbents adapted from Rabinovich et al., 2018 [47].

Elements (mM kg^{-1})	**SWW15**	**SWW35**	**DWW35**	**DWW68**
Ca	69	57	1900	3067
Mg	3815	3872	897	1021
P	3519	3615	819	927
Al	32	29	389	399
Fe	32	24	392	336
Mn	57	74	136	142
Zn	17	10	90	59
Minerals (%)				
struvite	98	95	33	28
K-struvite	2	2	8	3
calcite	-	2	17	55
monohydrocalcite	-	-	42	13
Crystallinity (%)	94	94	75	87
Dissolved Organic Carbon	5	2	7	29

Model-Dependent Kinetic Analysis

The model-based approach assumes multi-step reactions and a kinetic equation is found to describe the individual reaction rates for each separate step. The reaction type for each step is described by the function f_j (e_j;p_j). Where the initial reactant e_j, the product concentration p_j, the pre-exponential factor A_j and the activation energy E_j (pertaining only to the step (j), the model can describe the multistep reactions with equation Eq. (S.1).

$$\text{Reaction Rate}_j = -A_j f_j (e_j;p_j \exp\left(\frac{Ej}{RT}\right) \quad \text{(S.1)}$$

The model multiplies the individual reaction rates by the total effect (mass change) of each step to determine the total TG signal.

The model-dependent kinetics are described by the general rate equation (Equation S.2) which combines the Arrhenius equation with the Law of mass action. The model used the following equation with reaction type Fn, n^{th} order.

$$\left(\frac{\mathrm{d(a->b)}}{\mathrm{dt}}\right) = \mathrm{A*[a\text{^}n]*exp}\left(\frac{-\mathrm{Ea}}{RT}\right) \quad \text{(S.2)}$$

Where:

a	= reaction fraction (n^{th} order)
$\left(\frac{\mathrm{d(a->b)}}{\mathrm{dt}}\right)$	= rate of reaction
A	= pre-exponential factor
[a^n]	= kinetic expression
exp	= natural logarithm base
Ea	= activation energy
R	= gas constant
T	= absolute temperature

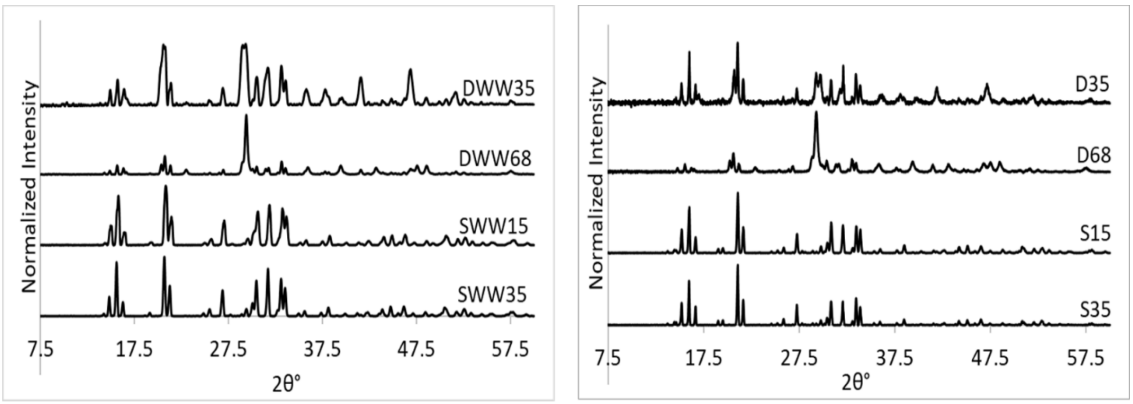

Figure 4.S1. X-ray diffraction patterns for livestock effluent-recovered solids after collection (SWW, DWW), Rabinovich et al., 2018 [47], and after 6 months in storage (S, D) showing no significant mineralogical changes occurred.

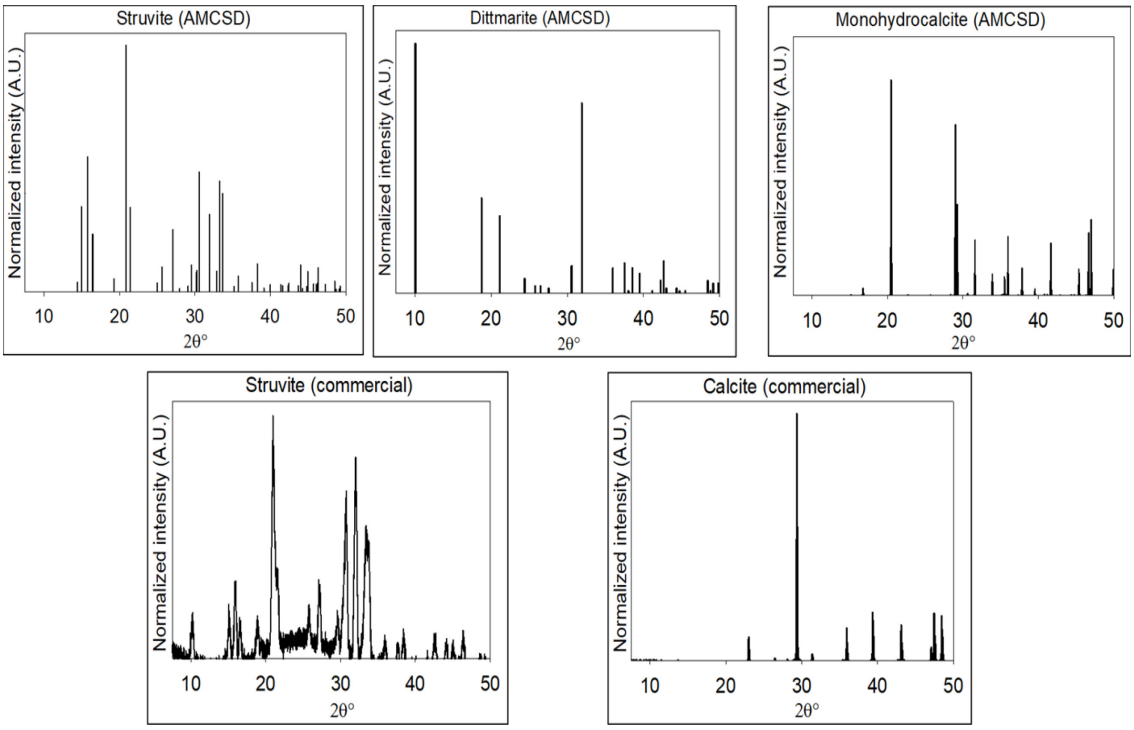

Figure 4.S2. X-ray diffraction patterns acquired from AMCSD for struvite, dittmarite, monohydrocalcite, and collected commercial struvite and calcite patterns.

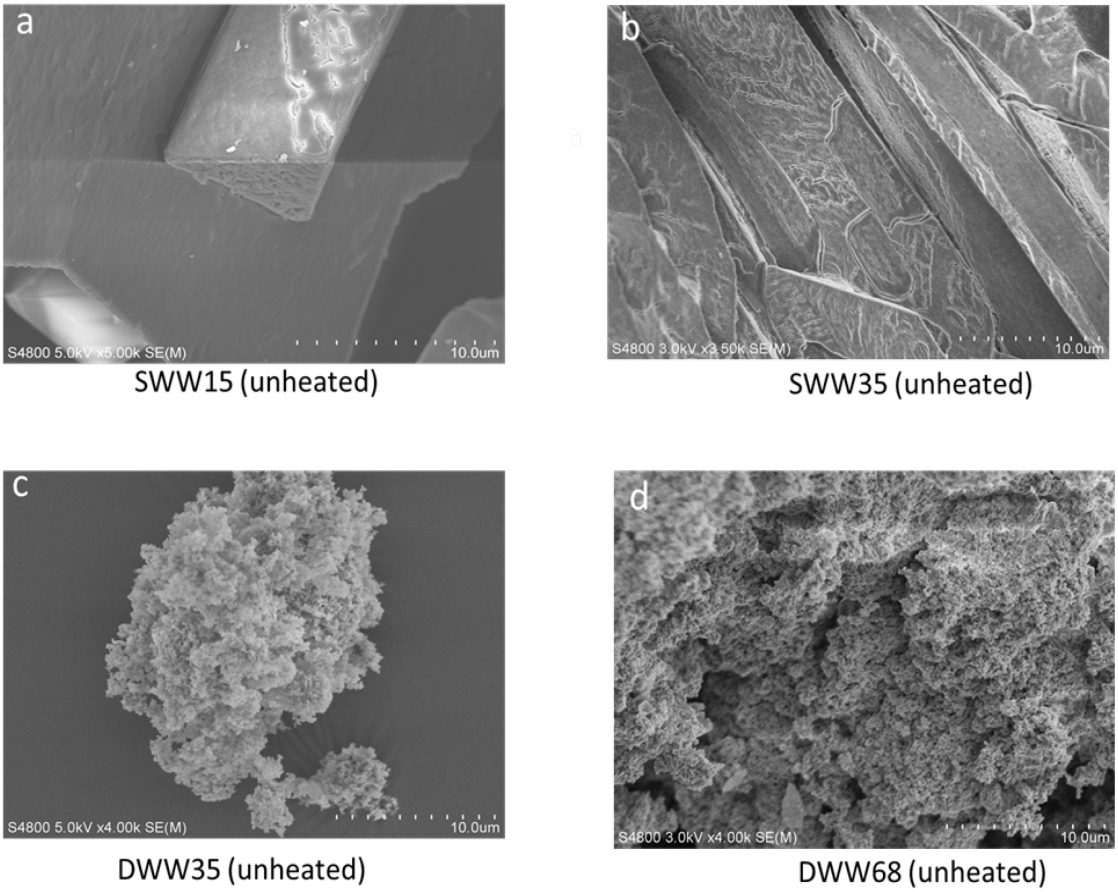

Figure 4.S3. SEM images of unheated, original SWW and DWW solids showing crystalline features (SWW), and homogenous, compact surfaces (SWW, DWW). These images were collected previously by Rabinovich et al., 2018. The bar scale at the bottom ranges from 1-10 μm.

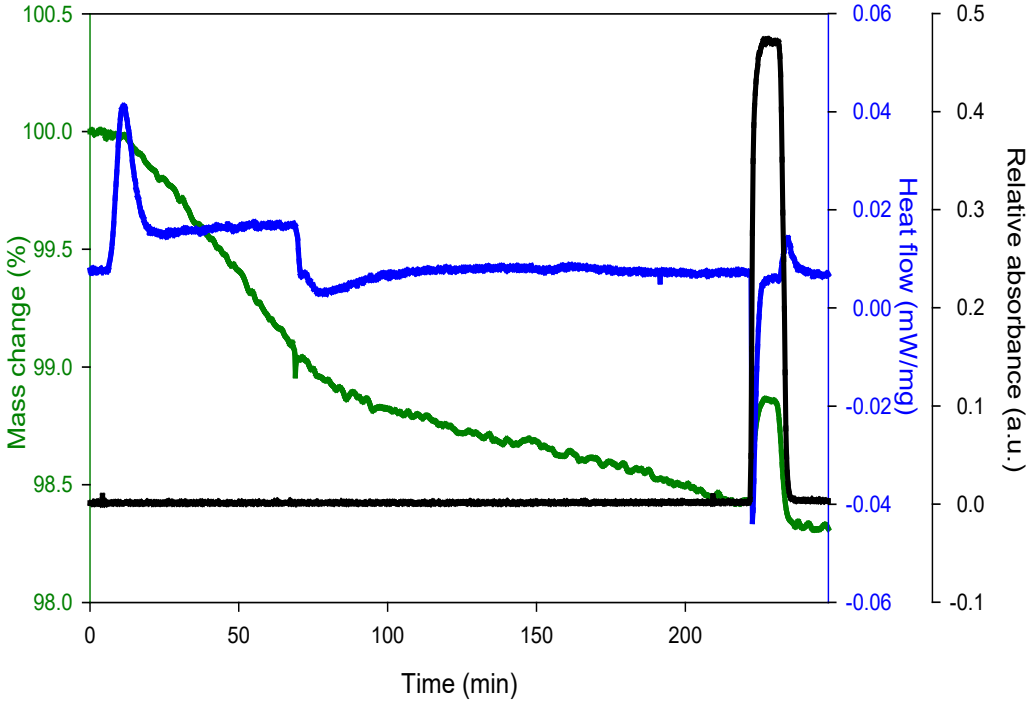

Figure 4.S4. The STA-PTA-FTIR process with struvite as sorbent. Pretreatment, sorption and desorption are indicated. The green, blue and black curves represent mass change (%) by TG, heat flow (mW mg^{-1}) by DSC (exo down), and Gram-Schmidt (a.u.), respectively.

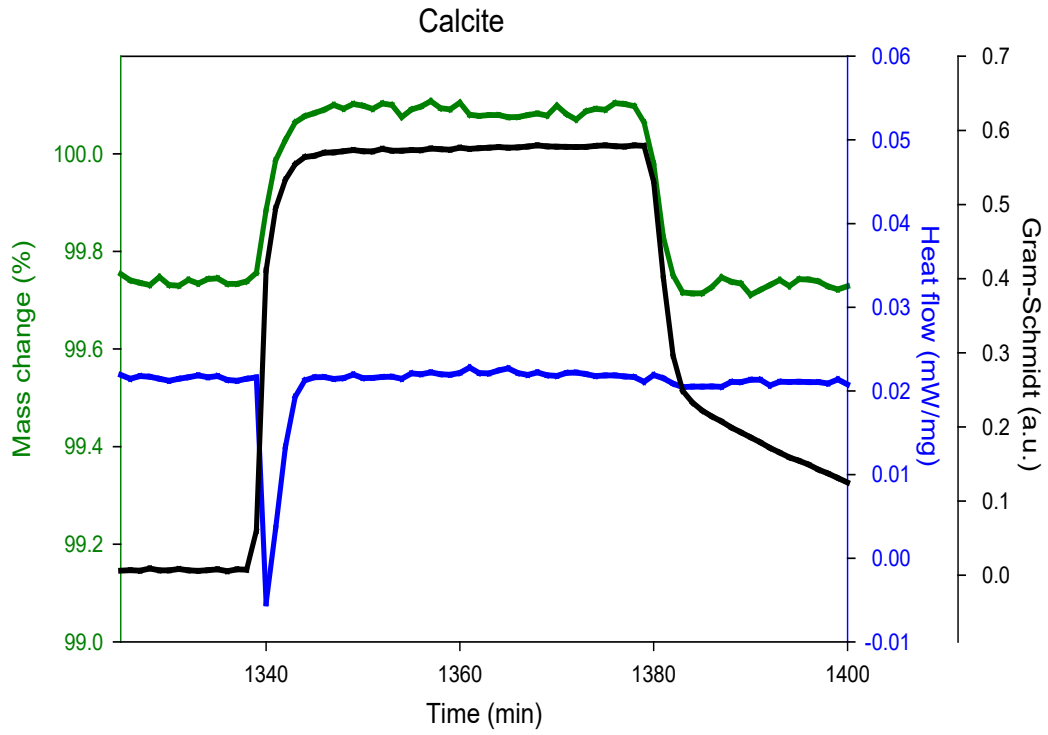

Figure 4.S5. STA-PTA-FTIR with calcite as sorbent reacted with NH_3(g). The green, blue and black lines represent mass change, heat flow and Gram-Schmidt signal respectively.

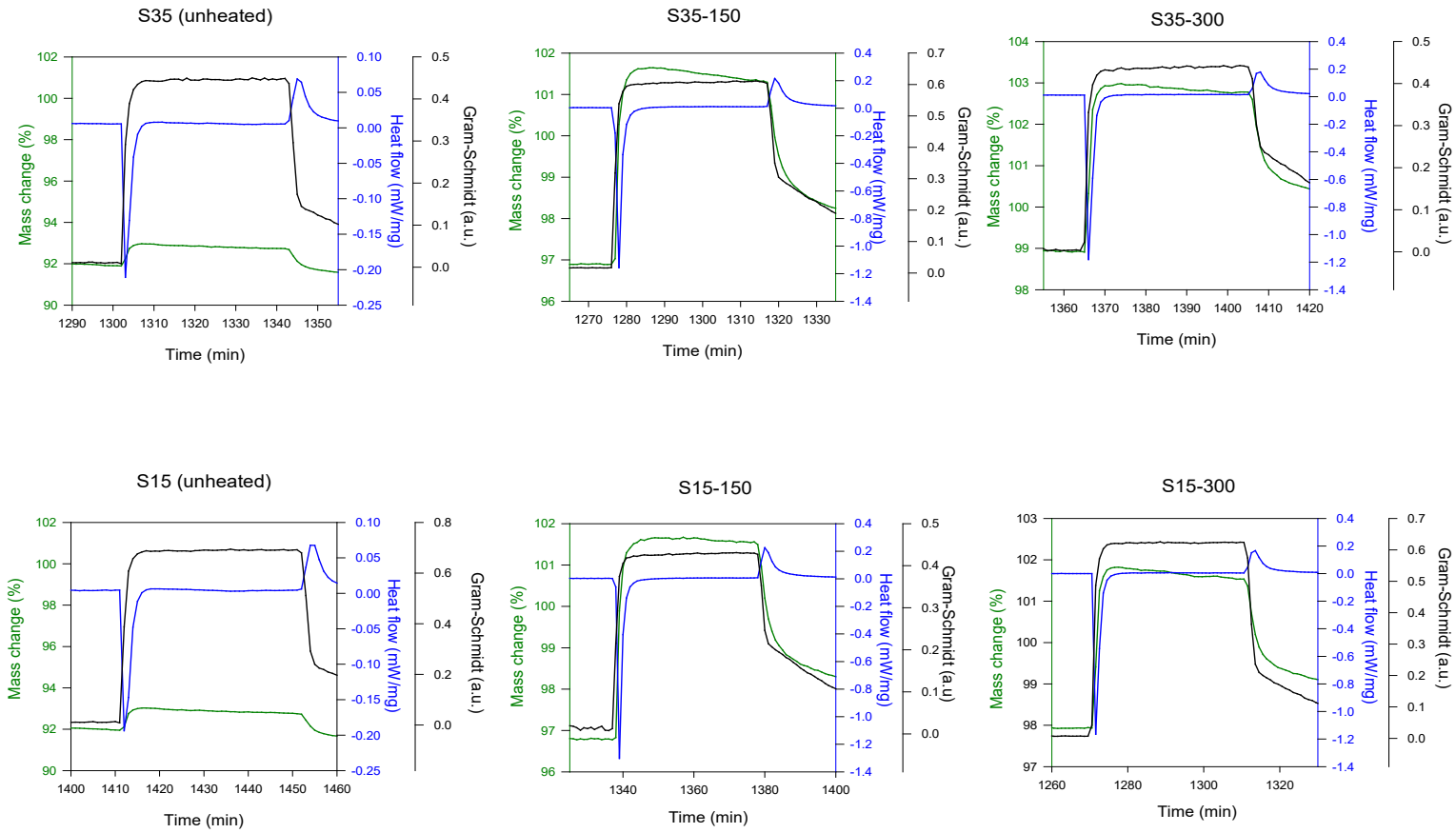

Figure 4.S6a.The STA-PTA-FTIR (25 °C) plots for Swine effluent-recovered sorbents. The green, blue and black curves represent mass change, heat flow and Gram-Schmidt signal respectively.

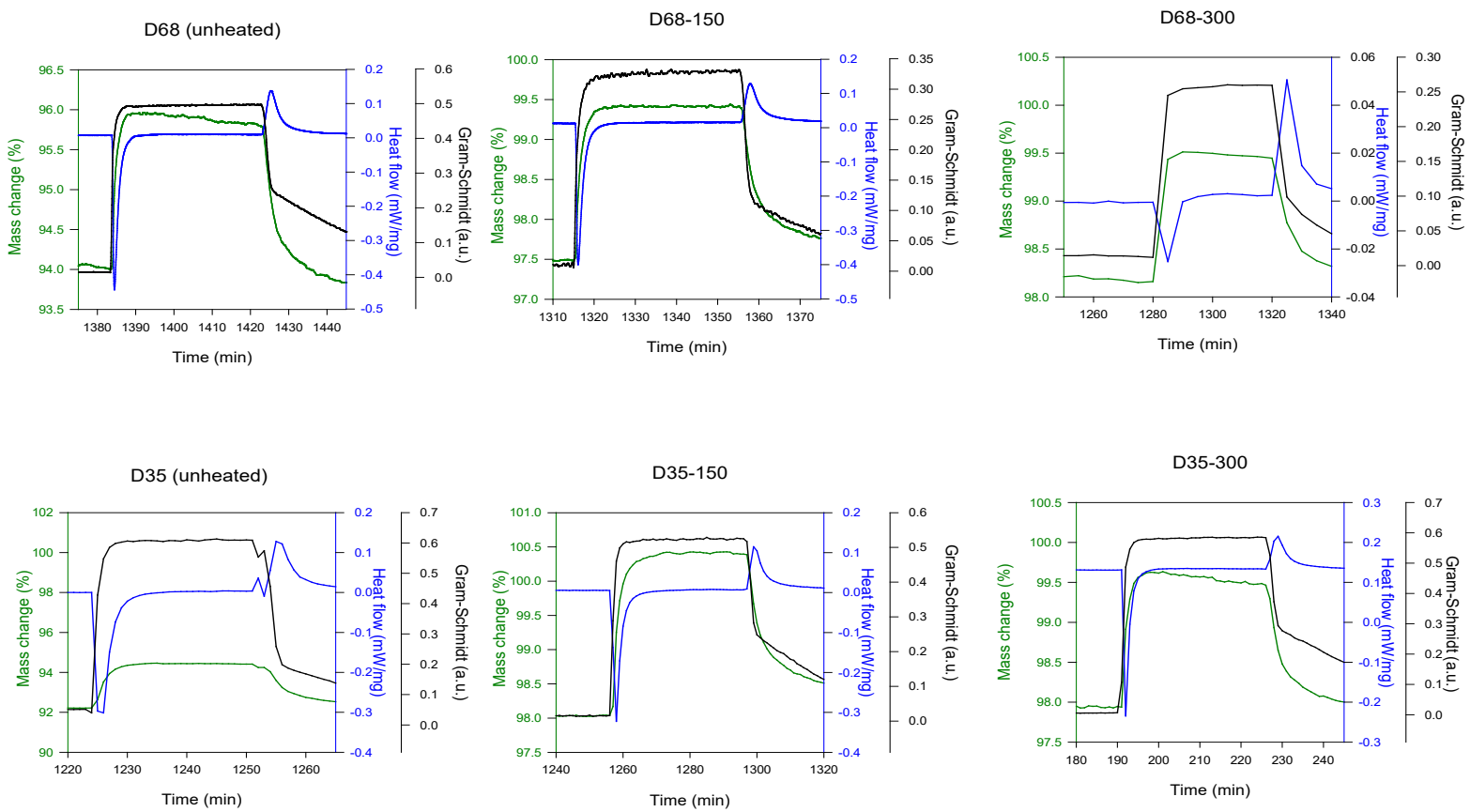

Figure 4.S6b. The STA-PTA-FTIR (25 °C) plots for dairy effluent-recovered sorbents. The green, blue and black curves represent mass change, heat flow and Gram-Schmidt signal respectively.

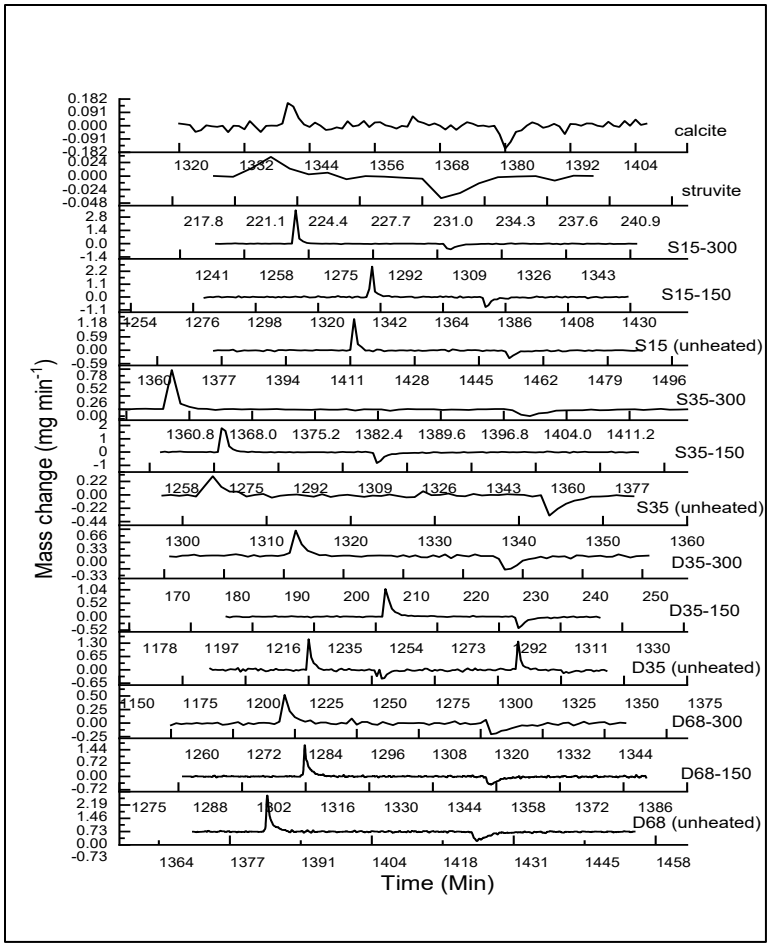

Figure 4.S7. The DTG profiles for all the DW and SW solids from STA-PTA-FTIR showing the maximum rates of sorption and desorption (mg min $^{-1}$).

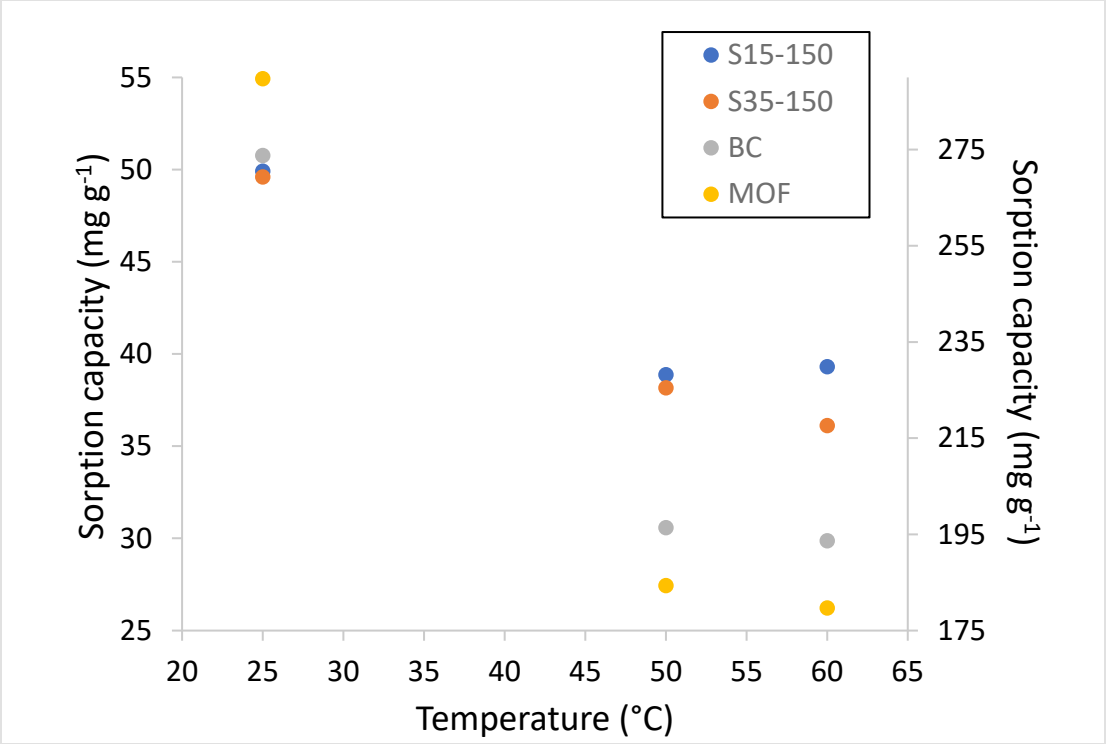

Figure 4.S8. Temperature-dependent sorption of NH_3(g) with selected sorbents.

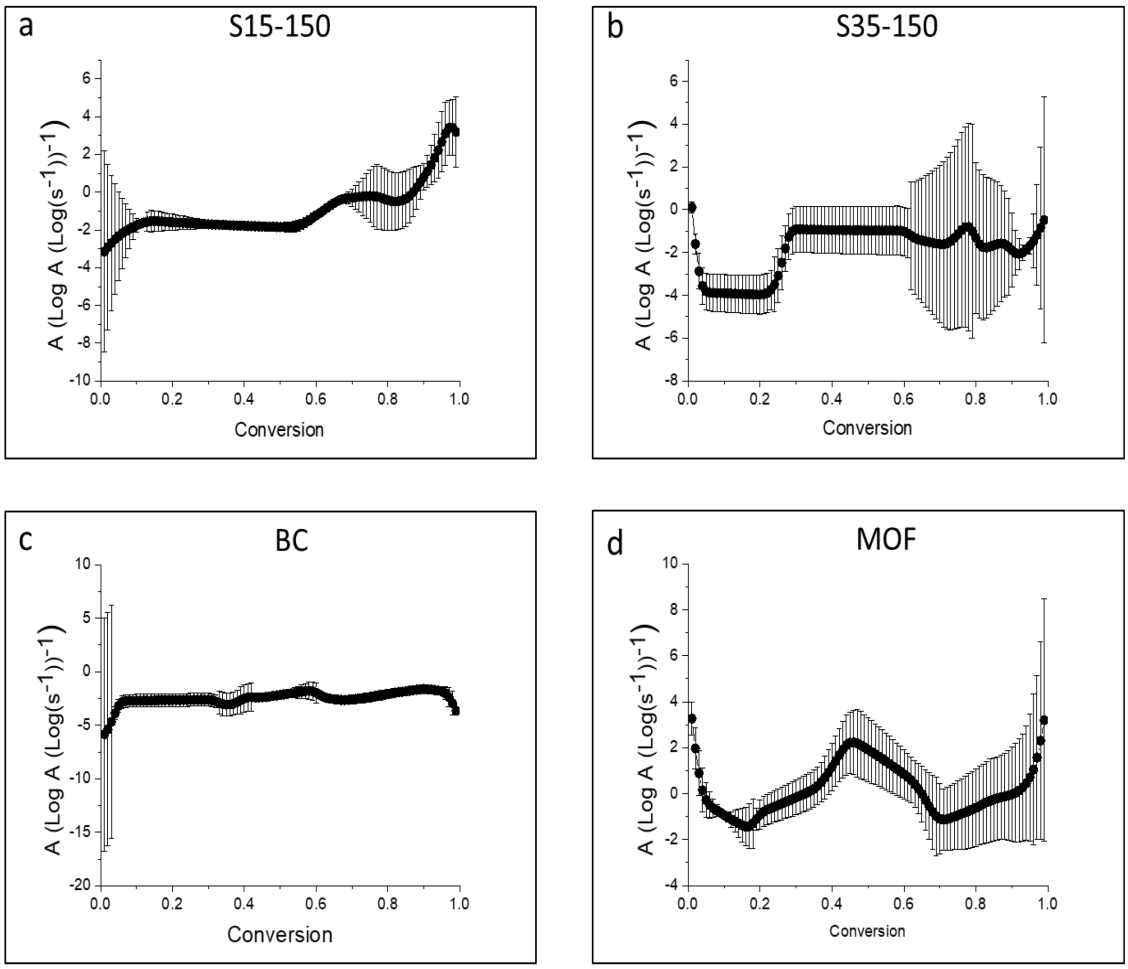

Figure 4.S9. The preexponential factors (A) for sorption, as a function of conversion.

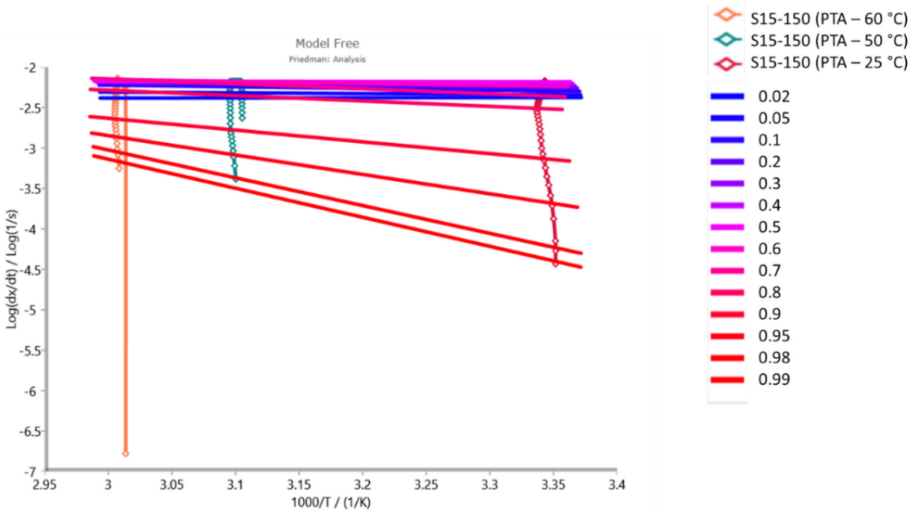

Figure 4.S10. Analysis graph from Friedman kinetics with log conversion rate versus inverse temperature. Lines are drawn through isoconversion points for each sorption experiment (25, 50 60 °C) and Ea and A are calculated from the slope and intersect of these lines respectively.

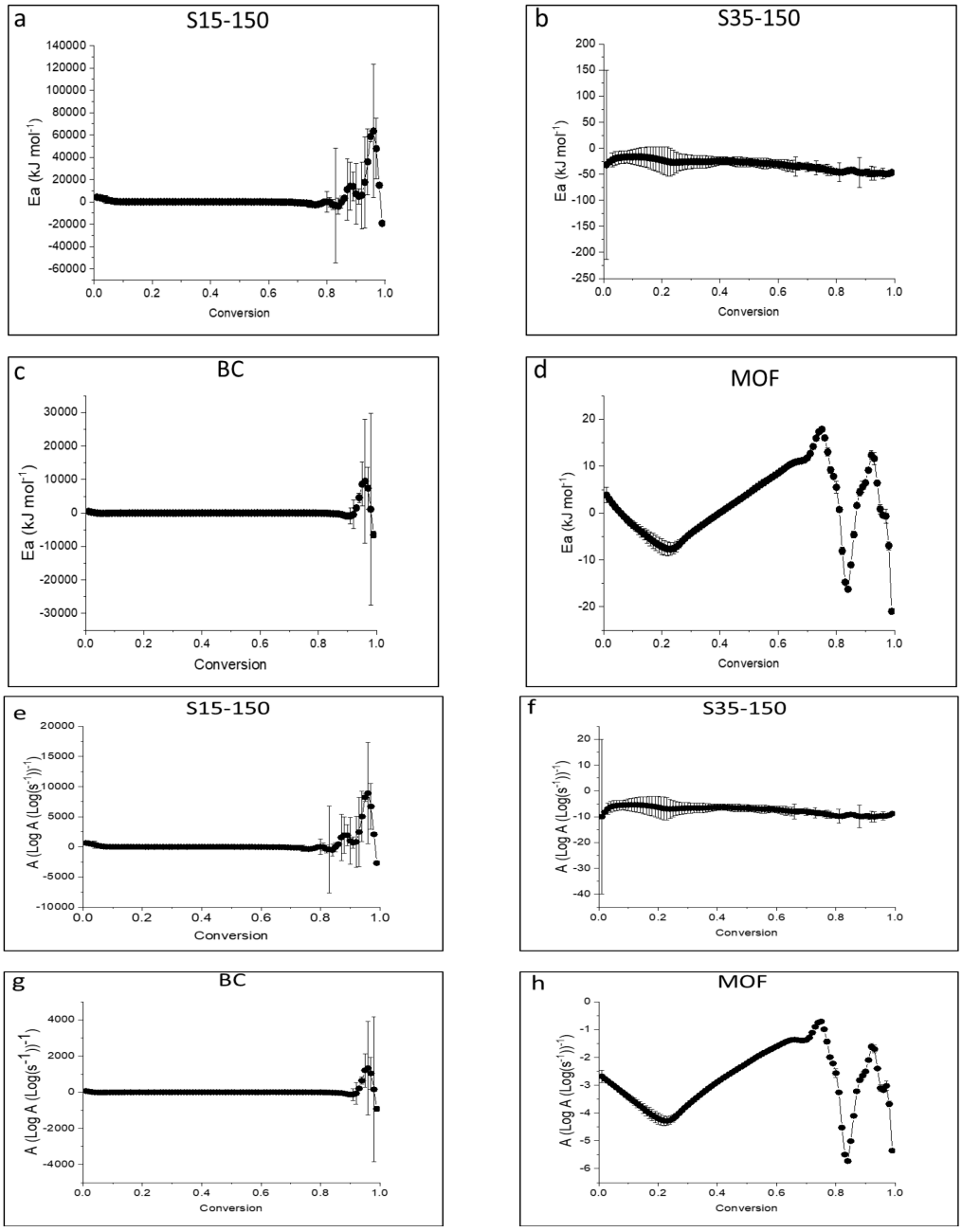

Figure 4.S11. Activation energy (a-d) and preexponential factor (e-h) from Friedman analysis (model-independent) describing desorption of NH_3(g) from S15-150, S35-150, BC and MOF, as a function of conversion.

Chapter 5 : Use of STA-PTA-FTIR to determine effect of pyrolysis temperature on the sorption capacity of sustainably-sourced sorbents for ammonia gas.

5.1. Introduction

Nutrient pollution of the environment from anthropogenic activity is of major concern. This type of environmental pollution can occur when nitrogen (N) from agricultural systems is volatilized and subsequently deposited into sensitive ecosystems [Anderson et al., 2003; Moore et al., 1995]. Volatilization of N from applied fertilizers is caused by N transformations of ammonium (NH_4^+(s)) to ammonia (NH_3(g)) and this process is a major source of atmospheric NH_3(g) [Battye et al., 2003, Bernal et al., 2009]. Manufacturing of NH_3(g) for fertilizer production by industrial nitrogen gas (N_2) fixation consumes approximately 2% of the world's energy and is a significant contributor of carbon dioxide (CO_2(g)) to the atmosphere [Kool et al., 2012]. In addition to environmental concerns, emissions of NH_3(g) from fertilizers thus represent significant economic disadvantages [Nye, 1986]. Inquiries about the nature and significance of N–carbon–climate interactions are becoming increasingly important. To reduce NH_3(g) emissions, sorption techniques may be advantageous, particularly for agricultural systems [Kastner 2009].

Some examples of sorbents typically utilized for removing NH_3(g) from waste streams include metal organic framework (MOF) [Jasuja et al., 2015] and biochar [Krolcyzk, 2014]. The use of MOF has some drawbacks, and field application is limited [Jasuja et al., 2015]. Biochar sorbents are more appropriate for agricultural systems. Some

examples of biochar sorbents for NH_3(g) have included coconut shell [Tsutomu et al,.2004] and woody charcoal [Fortier et al., 2008]. Some potential disadvantages of biochars include high energy demand during pyrolysis and functionalization of the biochar surface to optimize sorption. Sorption capacity of biochars are affected by pyrolysis temperature, parent material, and surface properties (functional groups, surface area, pore size) [Xie et al., 2015]. Further development of sorbents suitable for agriculture is urgently needed [Kastner et al., 2009]. Biochars produced from wastes have shown good potential [Tsutomu et al., 2004]. Therefore, evaluating alternative wastes, for example dairy waste compost, as a source for producing biochar is a sustainable and economical approach.

This work used composted dairy manure (DC) to represent a sustainable and cheap parent material in order to produce low-temperature biochar. Evaluating low temperature chars and recovering products from waste streams for subsequent repurposing is beneficial. The hyphenated simultaneous thermal analysis-pulse thermal analysis-Fourier transform infrared spectroscopy (STA-PTA-FTIR) technique was utilized to investigate the effects of pyrolysis temperature and heating rate, on the sorption capacity of the DC biochars for NH_3(g). This technique offers several advantages, including rapid and facile determination of key sorption data (sorption capacity, sorption enthalpy) under the same experimental setup for one sample. The STA-PTA-FTIR setup allows for carrying out pyrolysis and subsequent sorption-desorption experiments without exposing the sample to surrounding air, thus precluding artefacts [Ramlogan et al., 2018]. The experimental data during pyrolysis and subsequent sorption-desorption of NH_3(g) onto DC biochars was used to determine kinetic parameters (activation energy, preexponential factors, reaction order) by

model dependent and model independent methods, to describe the pyrolysis and sorption process.

5.2. Methods and Materials

Composted dairy manure was acquired from a compost heap located at a farm site. The samples were prepared for heating by Netzsch STA 449, combined with a Bruker Alpha FTIR, (STA-FTIR), under a dynamic heating range from 25 °C to final temperatures of 375 and 425 °C, using three heating rates (5, 10, 20 °C min^{-1}), in an N_2(g) atmosphere. A mass flow controller was used to maintain protective and pulse gas flowing at 20 and 50 ml min^{-1}. A Netzsch Pulse Thermal Analyzer was used to inject a volume of 50 ppm anhydrous NH_3(g) (99.995%) into the STA chamber at a pulse rate of 0.5 ml min^{-1}. The technique allows for the simultaneous collection of thermogravimetric (TG) and differential scanning calorimetry (DSC) data. Sorbents were labelled according to respective heat treatments, (5KSYN375, 10KSYN375, 20KSYN375, 5KSYN425, 10KSYN425, 20KSYN425). The composted manure was ground in a mortar and pestle and approximately 25-40 mg placed in an open ceramic crucible. The sample was heated from 25 °C and held isothermally at the pre-determined temperatures (80, 105, 325°C) required throughout the pyrolysis process prior to ramp up to final temperatures (375, 425 °C). A single pyrolysis without PTA to generate each DC biochar was required to characterize the biochar sorbents before reactions with NH_3(g). The sorbents were characterized by scanning electron microscopy (SEM) for surface morphology, and attenuated total reflectance-FTIR (ATR-FTIR) for functional groups. Next, two new pyrolysis-sorption-desorption experiments were performed to obtain duplicate data. For

sorption-desorption immediately following pyrolysis, the sample was cooled to 25 °C. The newly synthesized DC biochar sample was held isothermally at 25 °C until stable TG and DSC signals were acquired, prior to injections of NH_3(g). The pyrolyzed sample left inside the STA was never exposed to surrounding atmosphere between the different parts of the pyrolysis-sorption-desorption experiment. Acquired STA data was analyzed with Netzsch Proteus Thermal Analysis (TA) software version 6.1.0. The Proteus TA software was used to analyze TG mass changes over time, integrate DSC data and isolate peaks in DTG curves. Netzsch Kinetics Neo Software, version 2.1.2.2. provided kinetics information.

5.3. Results and Discussion

The TG data showing the extent of pyrolysis for DC to final temperatures of 375 (Fig.5.1a) and 425 °C (Fig.5.1b) is plotted. The heating rate is indicated by dashed lines for each respective sorbent. Mass loss was fastest at the highest heating rate. The compost underwent three mass lost steps corresponding to the dynamic heating program (25-80 °C), (80-105 °C), (105-375 °C). Mass loss was lowest in the intermediate temperature range, and highest during final ramp up. This trend was evident for all samples (Fig.5.1ab).

After pyrolysis, samples recovered from the STA were analyzed by SEM and images of biochar surface morphology were obtained (Fig. 5.2). The surfaces appear to have channels and the samples have developed pore spaces. The network of channels that provide a good sorbent framework was best observed for 20KSYN375.

The sorption capacity and integrated sorption enthalpy for reactions with DC biochars and NH_3(g) was obtained by STA-PTA-FTIR (Table 5.1). The maximum uptake

of NH_3(g) recorded by TG ranged from 38-60.7 mg g^{-1}. The sorption capacity for NH_3(g) was highest for the sorbent recovered after pyrolysis at the slowest rate and lowest temperature (5KSYN375) (Fig. 5.3). While the 5KSYN375 sorbent retained almost twice the mass of NH_3(g) as compared to all the other tested sorbents, the sorption capacity for sorbents produced at heating rates of 10 and 20 °C min^{-1} were comparable to each other, but generally increased for the biochars recovered after pyrolysis at 425 °C (Table 5.1). Though highest overall uptake was observed for 5KSYN375, the sorption enthalpy was lower as compared to the other two sorbents produced at faster heating rates (10, 20 °C min^{-1}). The 10KSYN375 sorbent retained approximately half the mass of NH_3(g) despite a larger sorption enthalpy value (-74.7 J g^{-1}) as compared to 5KSYN375 (-65.7 J g^{-1}). By contrast, for the DC sorbents pyrolyzed at 425 °C, sorption enthalpy was more than double for 5KSYN425 despite less total uptake, as compared with 10KSYN425 and 20KSYN425 sorbents. The enthalpy of sorption is directly related to the sorbed amount, types of sorption sites and concomitant binding energies. Differences in the types and amounts of functional groups (sorption sites) present on the surface of biochars are influenced by the heating rate [Xie et al., 2015]. Therefore, surface binding energy of the biochars likely varied with pyrolysis heating rate and was more important for producing the exothermic responses during sorption than the mass of sorbed NH_3(g). This could be attributed to the presence of active sites capable of stronger interactions and thus robust exothermic response, but with overall fewer sorption sites, observed total sorption was lower, as observed with 5KSYN425.

Model kinetics was performed using TG data from the pyrolysis experiments. The activation energies, preexponential factors and reaction orders were provided by the model.

At 425 °C, the model calculated activation energy of 51.54 kJ mol^{-1} with reaction order 1.9. The log A value was 1.99 s^{-1}. For pyrolysis at 375 °C, the model calculated activation energy of 48.88 kJ mol^{-1} with reaction order 1.64. The log A value was 1.57 s^{-1}.

5.3. Conclusion

The biochar sorbents derived from dairy waste compost exhibited good potential for sorbing NH_3(g). The sorption enthalpies suggested binding mechanism (strong and weak interactions) was an important factor for sorption, determined by the types of available active sites. The availability of higher energy sites was primarily dependent on the pyrolysis heating rate. This has implications for the application of these types of biochars. For example, a past study showed slow pyrolyzed biochar loaded with urea exhibited slow release behavior as compared to controls [Manikandan and Subramanian, 2015]. Therefore, biochars could be functionalized during pyrolysis to tightly sequester NH_3(g) via chemisorption or tailored to release sorbed NH_3(g) more easily, for example during application as a slow-release fertilizer after NH_3(g) sorption. The 5KSYN375 sorbent had the highest overall sorption capacity for NH_3(g) suggesting low-temperature treatment to produce biochar from agricultural wastes could be very promising and promotes efficient biomass application.

Tables and Figures

Table 5.1. The uptake of NH_3(g) and related sorption enthalpy.

Dairy Manure Compost	Uptake (mg g^{-1})	Heating Rate (°C min^{-1})	Pyrolysis (°C)	Enthalpy (J g^{-1})
5KSYN375	60.7	5	375	-65.7
10KSYN375	36.2	10	375	-74.7
20KSYN375	38	20	375	-35.05
5KSYN425	35.6	5	425	-70.45
10KSYN425	43.1	10	425	-33.78
20KSYN425	43.3	20	425	-34.98

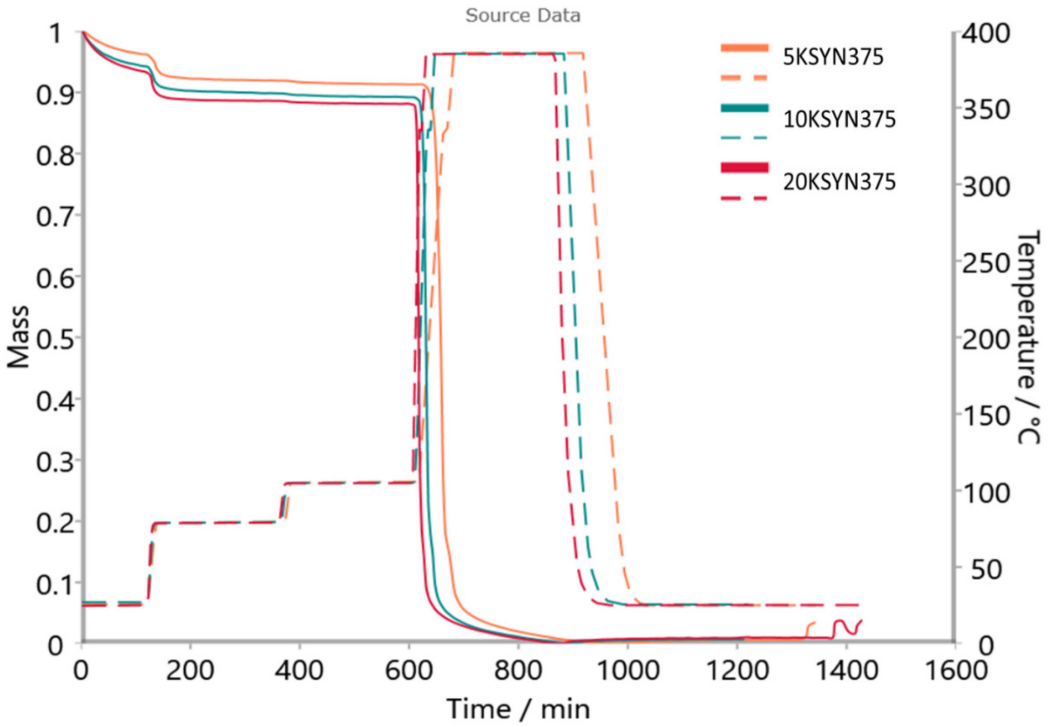

Fig. 5.1a. Pyrolysis of DC to 375 °C. Dashed lines indicate heating program.

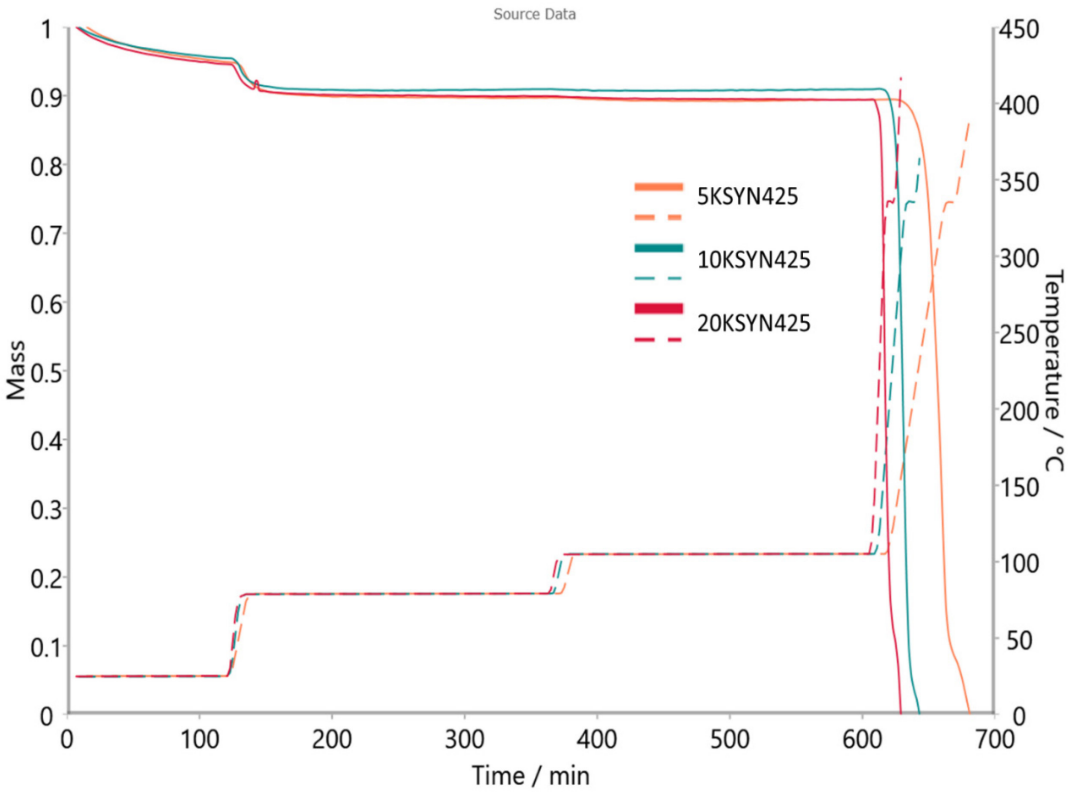

Fig. 5.1b. Pyrolysis of DC to 425 °C. Dashed lines indicate heating program.

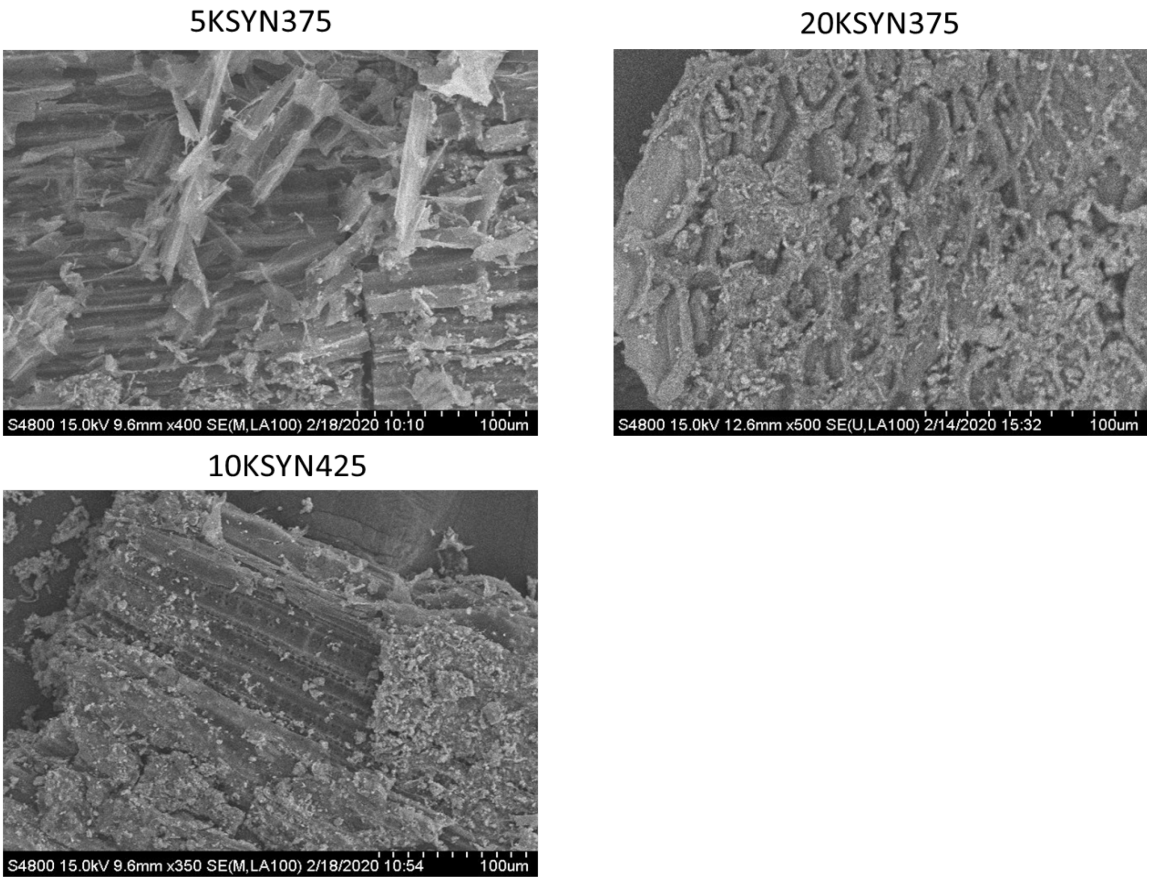

Fig. 5.2. Partial SEM images of DC biochars showing developed channel and framework.

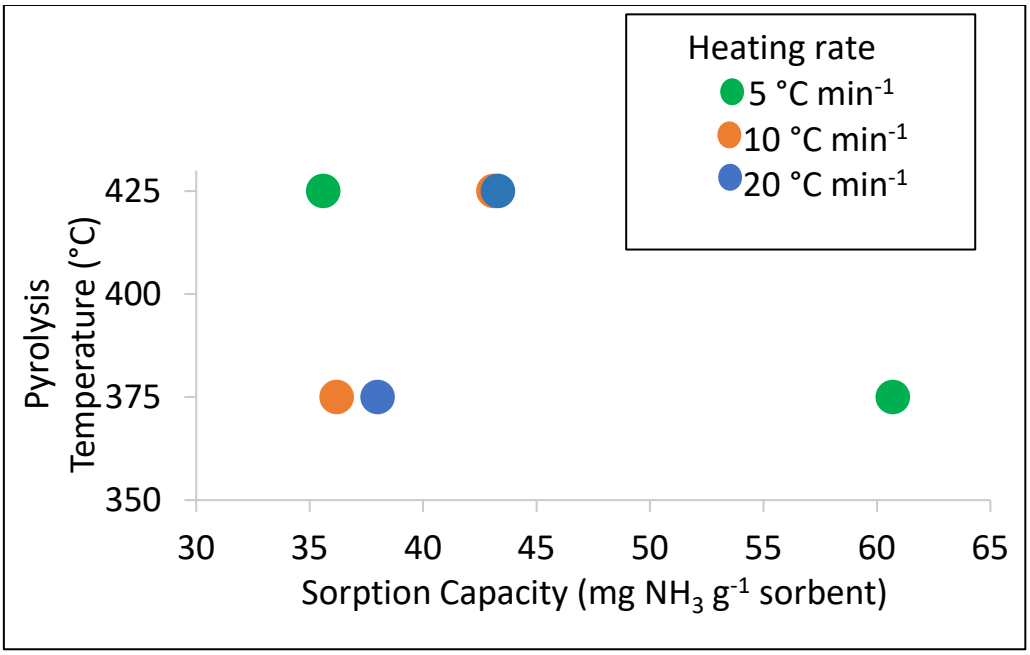

Figure 5.3. The uptake of NH_3(g) for six biochars produced at two heating rates and pyrolysis temperatures.

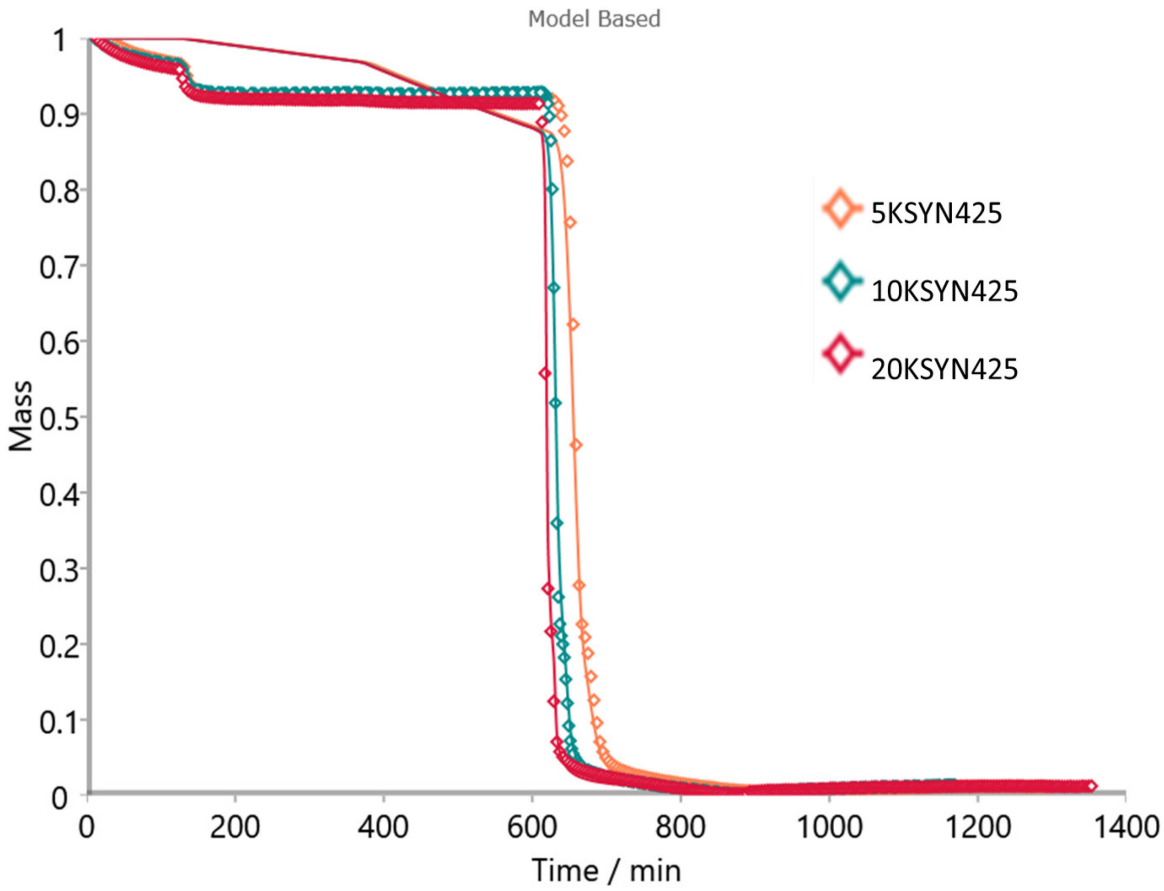

Fig. 5.4a. Model source data from pyrolysis of DC at 425 °C and three heating rates (5, 10, 20 °C min^{-1}). The solid line drawn thorough the points for each heating rate curve indicates the fit between the model and empirical data and suggests excellent agreement.

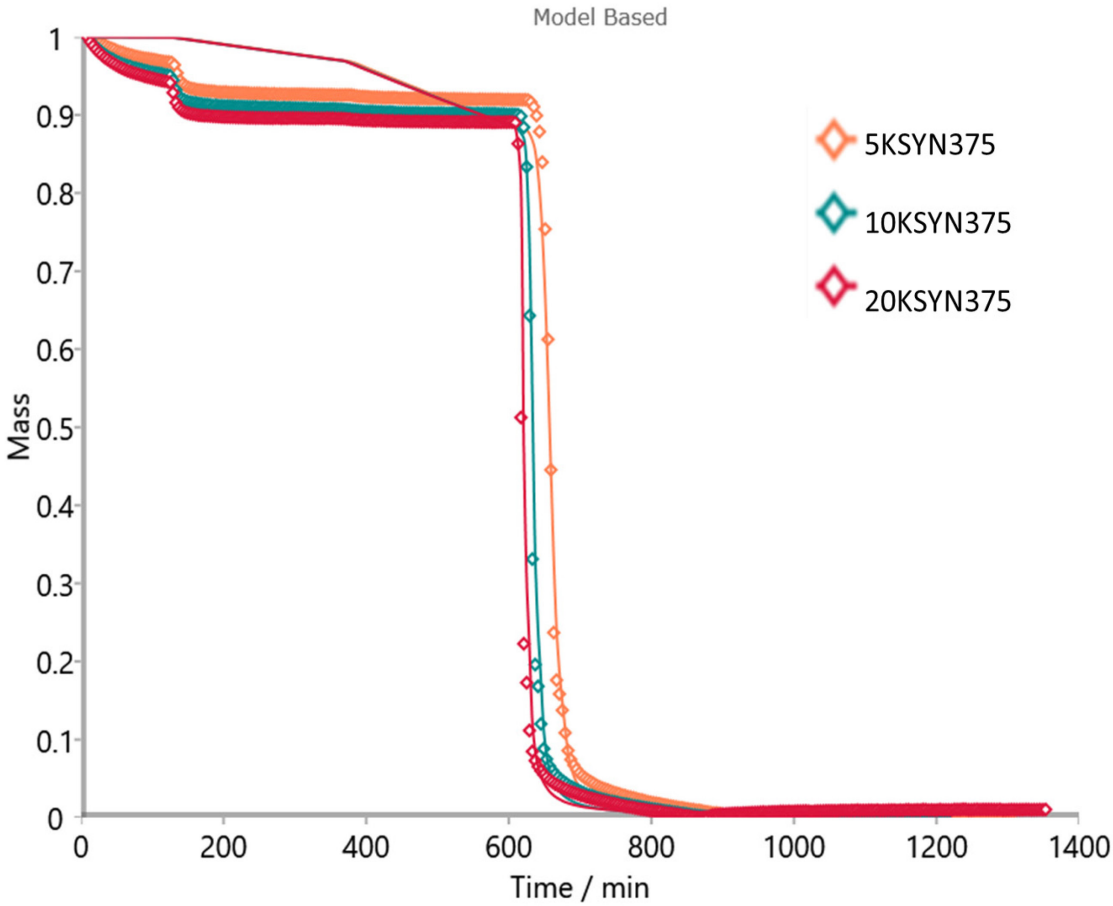

Fig. 5.4b. Model source data from pyrolysis of DC at 375 °C and three heating rates (5, 10, 20 °C min^{-1}). The solid line drawn thorough the points for each heating rate curve indicates the fit between the model and empirical data and suggests excellent agreement.

Chapter 6: Conclusion and Future Works

6.1. Summary of Findings

This thesis has shown STA-PTA-FTIR for sorption-desorption reactions can be used to assess the efficacy of different, sustainable sorbents for capturing NH_3(g). The hyphenated technique provided key data in a rapid and efficient manner. Observations of TG mass changes and the identification of evolved species during sorbent pretreatment enables determination of appropriate temperature to optimize removal of preadsorbed molecules. Following pulsing of NH_3(g), TG mass changes and concomitant enthalpies provided reliable, in-situ observations to better understand sorption phenomena under ambient pressure and specified temperature. Desorption could be carried out immediately following sorption without exposing the sample to surrounding atmosphere thus preserving quality and accuracy of the data.

In the first part of this dissertation (chapter 2), the thermal decomposition products of struvite were characterized which confirmed the appearance of $Mg_2P_2O_7$ above 250 °C from the FTIR, UV-VIS and ICP-OES results, with NH_4^+(s) conserved in the solid at 150 °C. The third chapter confirmed heat-treated commercial struvite (HTS) can sequester NH_3(g) to an extent which was comparable to typical biochar sorbents. Heat treatment at 150 °C resulted in sorbents with fast uptake rate and high sorption capacity which was comparable with biochar. Increased surface energetic heterogeneity, availability of active sites and increased surface area due to heat treatment resulted in larger uptake capacities compared to unheated sorbents. The HTS were produced at significantly lower

temperatures than the biochars, and their use therefore represents an energy savings alternative. Based on the results with HTS, further investigations were required to test struvite reclaimed from wastewaters compared to commercial struvite (chapter 4). Struvite, and struvite-calcite sorbents derived from two varieties of livestock waste [Rabinovich et al., 2018] were evaluated and compared to biochar and MOF sorbents and was shown to be effective at sorbing NH_3(g). The sorbents precipitated from swine wastewater out-performed the sorbents recovered from dairy wastewater. A simple kinetic model was used to describe the kinetic parameters associated with sorption-desorption. Additionally, an isoconversional method showed activation energy and pre-exponential factor dependency suggesting multistep reactions occurred. Thus, besides thermodynamic information, crucial kinetic parameters were obtained under the same experimental setup to describe the interaction between NH_3(g) and sorbents reclaimed from livestock wastes. These kinetic parameters may be beneficial for describing uptake rates, and sorption mechanisms such as rapid physical sorption, which are important characteristics of sorbents. The thermodynamic and kinetic framework for evaluating sustainable sorbents developed in chapters 3 and 4 primarily focused on utilizing solids from wastewaters as sorbents. In chapter 5, the STA-PTA-FTIR technique was used to determine if agricultural wastes, for example, dairy waste compost (DC) can be converted into effective low-temperature (< 400 °C) biochar sorbents for NH_3(g). The biochar (5KSYN375) pyrolyzed at the slowest rate (5 °C min^{-1}) and lowest temperature (375 °C) sorbed the highest amount of NH_3(g) as compared to DC biochars produced at faster (10, 20 °C min^{-1}) and higher temperatures (425 °C). The results from chapter 5 were promising and further encourages the use of

different wastes as parent materials to be converted for alternative purposes, thus promoting waste management.

6.2. Broader Impacts

Sustainability and conservation are cornerstones of environmental science research focused on minimizing negative global environmental impacts from human activity. There is increasing concern and demand for implementing environmentally-friendly methods across many types of industries [Ralegaonkar, 2020]. Reclaiming and recycling products from waste sources is economically and environmentally advantageous. Some regions lack fertilizers and arable land while N is over applied in other areas. Though the world as a whole makes enough food to satisfy global demand entirely, malnutrition is still the main risk factor for ailment worldwide [Sanchez 2005]. Recovering minerals such as struvite can serve to both recoup nutrients from wastes, as well as ameliorate current farming practices where N limitations exist. In this way, wastewaters are valorized, nutrients are conserved, and effluent discharge limits may be more easily achieved.

Furthermore, encouraging the use of struvite from wastewaters as a parent material to generate sorbents for conserving $NH_3(g)$ in agricultural settings also allows for the recovery of N and P from effluents, and therefore has the dual effect of recouping these nutrients for subsequent application. Removal of N and P from wastes will minimize environmental effects such as eutrophication while atmospheric hazards associated with N emissions may be reduced by sorbent addition. This work sought to provide fundamental

information on alternative sorbents for N sequestration and in general, the STA-PTA-FTIR technique is an ideal method for monitoring sorption-desorption phenomena.

6.3. Future works

This body of work served as a fundamental study on the possibilities of using sorbents reclaimed from agricultural wastes. The successful results from the sorbent evaluations suggest further testing of different types of sorbents should be conducted using STA-PTA-FTIR. Sorbents with potential for sequestering $NH_3(g)$ from excess biosolids, for example dairy manure compost, and organic wastes such as crop residues, should be evaluated. This research was limited to laboratory scale testing, under inert $N_2(g)$ atmosphere. This was done to ensure the sample reacted only with temperature, for example during pre-treatment, or elevated temperature experiments, and that all mass changes were only due to $NH_3(g)$ reactions, thus precluding atmospheric deposition of volatiles such as $CO_2(g)$ and water $(H_2O)(g)$. Therefore, testing under air (including humidity), limited-oxygen environments, and evaluating possible competitive gases is recommended. The impact of air on the sorption-desorption processes is likely limited. The presence of competitive gases may affect uptake, rather than ambient oxygen content, since redox reactions are extremely unlikely at the conditions set during the STA trials. Secondly, the $N_2(g)$ STA atmosphere is likely a good proxy as compared to ~80% $N_2(g)$ concentration found under environmental or ambient conditions and thirdly, sorbate competition from a polar gas with good hydrostatic attraction similar to $NH_3(g)$ is unlikely in field settings where manures are the main source of volatiles. Furthermore, controlled

field testing of sorbents in natural settings prone to $NH_3(g)$ volatilization during season long operations should be performed. Initially, bench scale column experiments could be set up, to initially scale up the sorption study. This would allow for observations of both sorption phenomenon and the structural integrity of the sorbents themselves over a longer period of time, but in a controlled laboratory setting. In a soil or manure column, the struvite sorbents may begin breaking down, with dissolution likely over time. The relationship between the thermal stability and solubility of these sorbents should be elucidated from column experiments. For example, struvite is known as a low-soluble product, and dittmarite (HTS-150) is thermally more stable than struvite. However, the struvite-calcite sorbents may prove to be more recalcitrant. Scaling up to volumetric studies at field level, manures placed in a sealed bed, with gas pumps and other apparatus including gas traps filled with sorbents may offer further insights. The gas pressure and flow under volumetric studies may likely increase sorption capacity because in the STA, one drawback is limited sample interaction over time, due to the temporal nature of pulsing. A continuous flow of $NH_3(g)$ over a larger (area) sorbent bed as compared to the STA crucible should allow increased sorption. Increased reactions should occur as the sorbents are more spread out, and bed depth is minimized. However, the solubility behavior of sorbents under environmental conditions as compared to inert STA environment should be examined. Structural breakdown in the sorbent bed over time could occur if the conditions for dissolution are met. Finally, it is recommended to utilize the key feature of PTA, i.e., selective gas pulsing, to develop sorbents for other environmentally relevant gases, for example carbon dioxide and methane.

References

Abdelrazig B, Sharp JH. Phase changes on heating ammonium magnesium phosphate hydrates. 1988;129(2):197–215. (Thermochimica Acta).

Adnadevic B, Mojovic Z, Abu Rabi A, Jovanovic J. Isoconversional Kinetic Analysis of Isothermal Selective Ethanol Adsorption on Zeolite Type NaZSM-5. 2007;30(9):1228–1234. (Chemical Engineering & Technology: Industrial Chemistry-Plant Equipment-Process Engineering-Biotechnology).

Agyarko-Mintah E, Cowie A, Van Zwieten L, Singh BP, Smillie R, Harden S, Fornasier F. Biochar lowers ammonia emission and improves nitrogen retention in poultry litter composting. 2017;61:129–137. (Waste Management).

Ahmad M, Lee SS, Dou X, Mohan D, Sung J-K, Yang JE, Ok YS. Effects of pyrolysis temperature on soybean stover-and peanut shell-derived biochar properties and TCE adsorption in water.

Ahmad M, Rajapaksha AU, Lim JE, Zhang M, Bolan N, Mohan D, Vithanage M, Lee SS, Ok YS. Biochar as a sorbent for contaminant management in soil and water: a review. 2014;99:19–33. (Chemosphere).

Allen ER, Hossner LR, Ming DW, Henninger DL. Solubility and Cation-Exchange in Phosphate Rock and Saturated Clinoptilolite Mixtures. 1993;57(5):1368–1374. (Soil Science Society of America Journal). doi:10.2136/sssaj1993.03615995005700050034x

Almeelbi T, Bezbaruah A. Nanoparticle-sorbed phosphate: iron and phosphate bioavailability studies with Spinacia oleracea and Selenastrum capricornutum. 2014;2(7):1625–1632. (ACS Sustainable Chemistry & Engineering).

Anderson N, Strader R, Davidson C. Airborne reduced nitrogen: ammonia emissions from agriculture and other sources. 2003;29(2–3):277–286. (Environment international).

Aneja VP, Blunden J, James K, Schlesinger WH, Knighton R, Gilliam W, Jennings G, Niyogi D, Cole S. Ammonia assessment from agriculture: US status and needs. 2008;37(2):515–520. (Journal of environmental quality).

Aneja VP, Bunton B, Walker JT, Malik BP. Measurement and analysis of atmospheric ammonia emissions from anaerobic lagoons. 2001;35(11):1949–1958. (Atmospheric Environment).

Anstoetz M, Sharma N, Clark M, Yee LH. Characterization of an oxalate-phosphate-amine metal–organic framework (OPA-MOF) exhibiting properties suited for innovative applications in agriculture. 2016;51(20):9239–9252. (Journal of Materials Science).

Å optrajanov B, Stefov V, Kuzmanovski I, Jovanovski G, Lutz HD, Engelen B. Very low Hâ€“Oâ€“H bending frequencies. IV. Fourier transform infrared spectra of synthetic dittmarite. 2002;613(1–3):7–14. (Journal of Molecular Structure).

Arami-Niya A, Rufford TE, Birkett G, Zhu Z. Gravimetric adsorption measurements of helium on natural clinoptilolite and synthetic molecular sieves at pressures up to 3500 kPa. 2017;244:218–225. (Microporous and Mesoporous Materials).

Baek BH, Aneja VP, Tong Q. Chemical coupling between ammonia, acid gases, and fine particles. 2004;129(1):89–98. (Environmental Pollution).

Balabanovich AI, Hornung A, Merz D, Seifert H. The effect of a curing agent on the thermal degradation of fire retardant brominated epoxy resins. 2004;85(1):713–723. (Polymer Degradation and Stability).

Barbarick KA, Lai TM, Eberl DD. Exchange Fertilizer (Phosphate Rock Plus Ammonium-Zeolite) Effects on Sorghum Sudangrass. 1990;54(3):911–916. (Soil Science Society of America Journal). doi:10.2136/sssaj1990.03615995005400030050x

Barthelmie RJ, Pryor SC. Implications of ammonia emissions for fine aerosol formation and visibility impairment: A case study from the Lower Fraser Valley, British Columbia. 1998;32(3):345–352. (Atmospheric Environment).

Battye W, Aneja VP, Roelle PA. Evaluation and improvement of ammonia emissions inventories. 2003;37(27):3873–3883. (Atmospheric Environment).

Behera SN, Sharma M, Aneja VP, Balasubramanian R. Ammonia in the atmosphere: a review on emission sources, atmospheric chemistry and deposition on terrestrial bodies. 2013;20(11):8092–8131. (Environmental Science and Pollution Research).

Belmabkhout Y, Frere M, De Weireld G. High-pressure adsorption measurements. A comparative study of the volumetric and gravimetric methods. 2004;15(5):848. (Measurement Science and Technology).

Berger AH, Bhown AS. Comparing physisorption and chemisorption solid sorbents for use separating CO2 from flue gas using temperature swing adsorption. 2011;4:562–567. (Energy Procedia).

Bernal MP, Alburquerque JA, Moral R. Composting of animal manures and chemical criteria for compost maturity assessment. A review. 2009;100(22):5444–5453. (Bioresource technology).

Bernal MP, Lopez-Real JM. Natural zeolites and sepiolite as ammonium and ammonia adsorbent materials. 1993;43(1):27–33. (Bioresource technology).

Bernal MP, Lopez-Real JM, Scott KM. Application of natural zeolites for the reduction of ammonia emissions during the composting of organic wastes in a laboratory composting simulator. 1993;43(1):35–39. (Bioresource technology).

Berner AH, Felix JD. Investigating ammonia emissions in a coastal urban airshed using stable isotope techniques. 2020;707:134952. (Science of The Total Environment).

Bhuiyan MIH, Mavinic DS, Koch FA. Thermal decomposition of struvite and its phase transition. 2008;70(8):1347–1356. (Chemosphere).

Bittman S, Mikkelsen R. Ammonia emissions from agricultural operations: livestock. 2009;93(1):28–31. (Better Crops).

Booker NA, Priestley AJ, Fraser IH. Struvite formation in wastewater treatment plants: opportunities for nutrient recovery. 1999;20(7):777–782. (Environmental technology).

Boonchom B. Kinetic and thermodynamic studies of MgHPO4Â· 3H2O by non-isothermal decomposition data. 2009;98(3):863–871. (Journal of thermal analysis and calorimetry).

Borfecchia E, Maurelli S, Gianolio D, Groppo E, Chiesa M, Bonino F, Lamberti C. Insights into adsorption of NH3 on HKUST-1 metal–organic framework: a

multitechnique approach. 2012;116(37):19839–19850. (The Journal of Physical Chemistry C).

Bouwman AF, Lee DS, Asman W, Dentener FJ, Van Der Hoek KW, Olivier J. A global highâ€resolution emission inventory for ammonia. 1997;11(4):561–587. (Global Biogeochemical Cycles).

Bouwman AF, Lee DS, Asman W, Dentener FJ, Van Der Hoek KW, Olivier J. A global high-resolution emission inventory for ammonia. 1997;11(4):561–587. (Global Biogeochemical Cycles).

Bowser BH, Brower LJ, Ohnsorg ML, Gentry LK, Beaudoin CK, Anderson ME. Comparison of surface-bound and free-standing variations of HKUST-1 MOFs: Effect of activation and ammonia exposure on morphology, crystallinity, and composition. 2018;8(9):650. (Nanomaterials).

Buss W, Graham MC, MacKinnon G, Mašek O. Strategies for producing biochars with minimum PAH contamination. 2016;119:24–30. (Journal of Analytical and Applied Pyrolysis).

Bussink DW, Huijsmans J, Ketelaars J. Ammonia volatilization from nitric-acid-treated cattle slurry surface applied to grassland. 1994;42(4):293–309. (NJAS wageningen journal of life sciences).

Cech E. Great Problems of Grand Challenges: Problematizing Engineering ï¾’ s Understandings of Its Role in Society. 2012;1(2):85–94. (International Journal of Engineering, Social Justice, and Peace).

Cervantes-Uc JM, Cauich-RodrÃguez JV, VÃ¡zquez-Torres H, Garfias-MesÃas LF, Paul DR. Thermal degradation of commercially available organoclays studied by TGAâ€“FTIR. 2007;457(1–2):92–102. (Thermochimica Acta).

Chau CK, Qiao F, Li Z. Microstructure of magnesium potassium phosphate cement. 2011;25(6):2911–2917. (Construction and Building Materials).

Chen Q, Yu H, Wang L, Abdin Z, Yang X, Wang J, Zhou W, Zhang H, Chen X. Synthesis and characterization of amylose grafted poly (acrylic acid) and its application in ammonia adsorption. 2016;153:429–434. (Carbohydrate Polymers).

Chen W, Liao X, Wu Y, Liang JB, Mi J, Huang J, Zhang H, Wu Y, Qiao Z, Li X. Effects of different types of biochar on methane and ammonia mitigation during layer manure composting. 2017;61:506–515. (Waste Management).

Chen X, Chen G, Chen L, Chen Y, Lehmann J, McBride MB, Hay AG. Adsorption of copper and zinc by biochars produced from pyrolysis of hardwood and corn straw in aqueous solution. 2011;102(19):8877–8884. (Bioresource technology).

Chen Y, Zhang F, Wang Y, Yang C, Yang J, Li J. Recyclable ammonia uptake of a MIL series of metal-organic frameworks with high structural stability. 2018;258:170–177. (Microporous and Mesoporous Materials).

Cherkasov N, Ibhadon AO, Fitzpatrick P. A review of the existing and alternative methods for greener nitrogen fixation. 2015;90:24–33. (Chemical Engineering and Processing: Process Intensification).

Chiang Y-C, Chiang P-C, Huang C-P. Effects of pore structure and temperature on VOC adsorption on activated carbon. 2001;39(4):523–534. (Carbon).

Cordell D, Drangert J-O, White S. The story of phosphorus: global food security and food for thought. 2009;19(2):292–305. (Global Environmental Change).

Day D, Evans RJ, Lee JW, Reicosky D. Economical CO2, SOx, and NOx capture from fossil-fuel utilization with combined renewable hydrogen production and large-scale carbon sequestration. 2005;30(14):2558–2579. (Energy).

DeCoste JB, Peterson GW, Schindler BJ, Killops KL, Browe MA, Mahle JJ. The effect of water adsorption on the structure of the carboxylate containing metal–organic frameworks Cu-BTC, Mg-MOF-74, and UiO-66. 2013;1(38):11922–11932. (Journal of Materials Chemistry A).

DeLaune PB, Moore PA, Daniel TC, Lemunyon JL. Effect of chemical and microbial amendments on ammonia volatilization from composting poultry litter. 2004;33(2):728–734. (Journal of environmental quality).

De-Xi L, Xiao-Hui F, Feng HU, Hong-Tao Z, Jia-Fa L. Ammonia volatilization and nitrogen utilization efficiency in response to urea application in rice fields of the Taihu Lake region, China. 2007;17(5):639–645. (Pedosphere).

Dhumal NR, Singh MP, Anderson JA, Kiefer J, Kim HJ. Molecular interactions of a Cu-based metal–organic framework with a confined imidazolium-based ionic liquid: a combined density functional theory and experimental vibrational spectroscopy study. 2016;120(6):3295–3304. (The Journal of Physical Chemistry C).

Dontsova KM, Norton LD, Johnston CT. Calcium and magnesium effects on ammonia adsorption by soil clays. 2005;69(4):1225–1232. (Soil Science Society of America Journal).

Doonan CJ, Tranchemontagne DJ, Glover TG, Hunt JR, Yaghi OM. Exceptional ammonia uptake by a covalent organic framework. 2010;2(3):235–238. (Nature chemistry).

Eigenmann F, Maciejewski M, Baiker A. Gas adsorption studied by pulse thermal analysis. 2000;359(2):131–141. (Thermochimica acta).

El Diwani G, El Rafie S, El Ibiari NN, El-Aila HI. Recovery of ammonia nitrogen from industrial wastewater treatment as struvite slow releasing fertilizer. 2007;214(1–3):200–214. (Desalination).

Etter B, Tilley E, Khadka R, Udert KM. Low-cost struvite production using source-separated urine in Nepal. 2011;45(2):852–862. (Water research).

Ferm M. Atmospheric ammonia and ammonium transport in Europe and critical loads: a review. 1998;51(1):5–17. (Nutrient Cycling in Agroecosystems).

Flynn JH, Wall LA. General treatment of the thermogravimetry of polymers. 1966;70(6):487. (Journal of Research of the National Bureau of Standards.Section A, Physics and Chemistry).

Fortier H, Westreich P, Selig S, Zelenietz C, Dahn JR. Ammonia, cyclohexane, nitrogen and water adsorption capacities of an activated carbon impregnated with increasing amounts of ZnCl2 and designed to chemisorb gaseous NH3 from an air stream. 2008;320(2):423–435. (Journal of colloid and interface science).

Fowler D, Coyle M, Skiba U, Sutton MA, Cape JN, Reis S, Sheppard LJ, Jenkins A, Grizzetti B, Galloway JN. The global nitrogen cycle in the twenty-first century. 2013;368(1621):20130164. (Philosophical Transactions of the Royal Society B: Biological Sciences).

Friedman HL. Kinetics of thermal degradation of char-forming plastics from thermogravimetry. Application to a phenolic plastic. Vol. 6. Wiley Online Library; 1964. p. 183–195.

Frost RL, Weier ML, Erickson KL. Thermal decomposition of struvite. 2004;76(3):1025–1033. (Journal of Thermal Analysis and Calorimetry).

Frost RL, Weier ML, Martens WN, Henry DA, Mills SJ. Raman spectroscopy of newberyite, hannayite and struvite. 2005;62(1–3):181–188. (Spectrochimica Acta Part A: Molecular and Biomolecular Spectroscopy).

Fumoto E, Tago T, Masuda T. Recovery of ammonia from biomass waste by adsorption on magnesium phosphate derived from magnesium ammonium phosphate. 2009;42(3):184–190. (Journal of Chemical Engineering of Japan).

Gu B, Schmitt J, Zhihong C, Liang L, McCarthy JF. Adsorption and desorption of natural organic matter on iron oxide: mechanisms and models. 1994;28(1):38-46. (Environmental Science and Technology).

Gronwald M, Helfrich M, Don A, Fuß R, Well R, Flessa H. Application of hydrochar and pyrochar to manure is not effective for mitigation of ammonia emissions from cattle slurry and poultry manure. 2018;54(4):451–465. (Biology and Fertility of Soils).

Hale SE, Lehmann J, Rutherford D, Zimmerman AR, Bachmann RT, Shitumbanuma V, O'Toole A, Sundqvist KL, Arp HPH, Cornelissen G. Quantifying the total and bioavailable polycyclic aromatic hydrocarbons and dioxins in biochars. 2012;46(5):2830–2838. (Environmental science & technology).

Halikia I, Zoumpoulakis L, Christodoulou E, Prattis D. Kinetic study of the thermal decomposition of calcium carbonate by isothermal methods of analysis. 2001;1(2):89–102. (European Journal of Mineral Processing and Environmental Protection).

Harding AW, Foley NJ, Norman PR, Francis DC, Thomas KM. Diffusion barriers in the kinetics of water vapor adsorption/desorption on activated carbons. 1998;14(14):3858–3864. (Langmuir).

Haroon M, Idrees F, Naushahi HA, Afzal R, Usman M, Qadir T, Rauf H. Nitrogen Use Efficiency: Farming Practices and Sustainability. 2019:1–11. (Journal of Experimental Agriculture International).

He B, Zheng X, Wen Y, Tong H, Chen M, Chen C. Temperature impact on SO2 removal efficiency by ammonia gas scrubbing. 2003;44(13):2175–2188. (Energy Conversion and Management).

He S, Zhang Y, Yang M, Du W, Harada H. Repeated use of MAP decomposition residues for the removal of high ammonium concentration from landfill leachate. 2007;66(11):2233–2238. (Chemosphere).

Helminen J, Helenius J, Paatero E, Turunen I. Adsorption equilibria of ammonia gas on inorganic and organic sorbents at 298.15 K. 2001;46(2):391–399. (Journal of Chemical & Engineering Data).

Huang H, Xu C, Zhang W. Removal of nutrients from piggery wastewater using struvite precipitation and pyrogenation technology. 2011;102(3):2523–2528. (Bioresource technology).

Jackson Ml, Chang SC. Anhydrous Ammonia Retention by Soils as Influenced by Depth of Application, Soil Texture, Moisture Content, pH Value, and Tilth 1. 1947;39(7):623–633. (Agronomy Journal).

Janczak D, MaliÅ„ska K, CzekaÅ‚a W, CÃ¡ceres R, Lewicki A, Dach J. Biochar to reduce ammonia emissions in gaseous and liquid phase during composting of poultry manure with wheat straw. 2017;66:36–45. (Waste Management).

Jasuja H, Peterson GW, Decoste JB, Browe MA, Walton KS. Evaluation of MOFs for air purification and air quality control applications: Ammonia removal from air. 2015;124:118–124. (Chemical Engineering Science).

Jeong Y-K, Kim J-S. A new method for conservation of nitrogen in aerobic composting processes. 2001;79(2):129–133. (Bioresource technology).

Kastner JR, Miller J, Das KC. Pyrolysis conditions and ozone oxidation effects on ammonia adsorption in biomass generated chars. 2009;164(2–3):1420–1427. (Journal of hazardous materials).

Kim D, Ryu H-D, Kim M-S, Kim J, Lee S-I. Enhancing struvite precipitation potential for ammonia nitrogen removal in municipal landfill leachate. 2007;146(1–2):81–85. (Journal of hazardous materials).

Kool A, Marinussen M, Blonk H. LCI data for the calculation tool Feedprint for greenhouse gas emissions of feed production and utilization. 2012. (GHG Emissions of N, P and K fertiliser production).

Królczyk JB. Metrological changes in the surface morphology of cereal grains in the mixing process. 2016;30(2). (International Agrophysics).

Kruse M, Bell J. Ammonia emissions and their role in acid deposition. 1987;21(9):1939–1946. (Atmospheric Environment (1967)).

Kurtulus G, Tas AC. Transformations of neat and heated struvite (MgNH4PO4· 6H2O). 2011;65(19–20):2883–2886. (Materials Letters).

Larrubia MA, Ramis G, Busca G. An FT-IR study of the adsorption of urea and ammonia over V2O5–MoO3–TiO2 SCR catalysts. 2000;27(3):L145–L151. (Applied Catalysis B: Environmental).

Le Corre KS, Valsami-Jones E, Hobbs P, Parsons SA. Phosphorus recovery from wastewater by struvite crystallization: A review. 2009;39(6):433–477. (Critical Reviews in Environmental Science and Technology).

Lee H, Shaker G, Naishadham K, Song X, McKinley M, Wagner B, Tentzeris M. Carbon-nanotube loaded antenna-based ammonia gas sensor. 2011;59(10):2665–2673. (IEEE Transactions on Microwave Theory and Techniques).

Lefcourt AM, Meisinger JJ. Effect of adding alum or zeolite to dairy slurry on ammonia volatilization and chemical composition. 2001;84(8):1814–1821. (Journal of dairy science).

Leip A, Billen G, Garnier J, Grizzetti B, Lassaletta L, Reis S, Simpson D, Sutton MA, De Vries W, Weiss F. Impacts of European livestock production: nitrogen, sulphur, phosphorus and greenhouse gas emissions, land-use, water eutrophication and biodiversity. 2015;10(11):115004. (Environmental Research Letters).

Lelieveld J, Evans JS, Fnais M, Giannadaki D, Pozzer A. The contribution of outdoor air pollution sources to premature mortality on a global scale. 2015;525(7569):367–371. (Nature).

Li H, Xin H, Burns RT. Reduction of ammonia emission from stored poultry manure using additives: Zeolite, Al clear, Ferix-3 and PLT. American Society of Agricultural and Biological Engineers; 2006. p. 1.

Li H, Xin H, Liang Y, Burns RT. Reduction of ammonia emissions from stored laying hen manure through topical application of zeolite, Al Clear, Ferix-3, or poultry litter treatment. 2008;17(4):421–431. (Journal of Applied Poultry Research).

Li XZ, Zhao QL. Recovery of ammonium-nitrogen from landfill leachate as a multi-nutrient fertilizer. 2003;20(2):171–181. (Ecological Engineering).

Li Z, Zhang X, Dong H, Zhang X, Gao H, Zhang S, Li J, Wang C. Efficient absorption of ammonia with hydroxyl-functionalized ionic liquids. 2015;99(5):81362–81370. (RSC Advances).

Liang Y, Leonard JJ, Feddes J, McGill WB. Influence of carbon and buffer amendment on ammonia volatilization in composting. 2006;97(5):748–761. (Bioresource technology).

Linares-Solano A, de Lecea CS-M, Alcaniz-Monge J, Cazorla-AmorÃ^{3}s D. Further advances in the characterization of microporous carbons by physical adsorption of gases. 1998;1998(185):316–325. (Tanso).

Linares-Solano A, de Lecea CS-M, Alcaniz-Monge J, Cazorla-Amorós D. Further advances in the characterization of microporous carbons by physical adsorption of gases. 1998;1998(185):316–325. (Tanso).

Liu L, Zhao C, Xu J, Li Y. Integrated CO2 capture and photocatalytic conversion by a hybrid adsorbent/photocatalyst material. 2015;179:489–499. (Applied Catalysis B: Environmental).

Liu Y, Kwag J-H, Kim J-H, Ra C. Recovery of nitrogen and phosphorus by struvite crystallization from swine wastewater. 2011;277(1–3):364–369. (Desalination).

Lonati G, Giugliano M, Butelli P, Romele L, Tardivo R. Major chemical components of PM2. 5 in Milan (Italy). 2005;39(10):1925–1934. (Atmospheric Environment).

Ma N, Rouff AA. Influence of pH and oxidation state on the interaction of arsenic with struvite during mineral formation. 2012;46(16):8791–8798. (Environmental science & technology).

Ma N, Rouff AA, Phillips BL. A 31P NMR and TG/DSC-FTIR investigation of the influence of initial pH on phosphorus recovery as struvite. 2014;2(4):816–822. (ACS Sustainable Chemistry & Engineering).

Madejová J, Janek M, Komadel P, Herbert H-J, Moog HC. FTIR analyses of water in MX-80 bentonite compacted from high salinary salt solution systems. 2002;20(6):255–271. (Applied Clay Science).

Makreski P, Todorov J, Jovanovski G, Stojanovska M, Petrushevski G. Depicting the dehydration and dehydroxylation processes in very rare hydrogen arsenate minerals. 2019;135(4):2265–2276. (Journal of Thermal Analysis and Calorimetry).

Manikandan A, Subramanian KS. Ability of Urea Impregnated Biochar Fertilizers For Securing the Slow Release of Nitrogen in Soilsâ€“Preliminary Study. 2015:0975–3710. (International Journal of Agriculture Sciences, ISSN).

Marnellos G, Stoukides M. Ammonia synthesis at atmospheric pressure. 1998;282(5386):98–100. (Science).

Martins O, Dewes T. Loss of nitrogenous compounds during composting of animal wastes. 1992;42(2):103–111. (Bioresource technology).

McCrory DF, Hobbs PJ. Additives to reduce ammonia and odor emissions from livestock wastes. 2001;30(2):345–355. (Journal of environmental quality).

McCubbin DR, Apelberg BJ, Roe S, Divita F. No title. 2002. (Livestock ammonia management and particulate-related health benefits).

Mestres G, Aguilera FS, Manzanares N, Sauro S, Osorio R, Toledano M, Ginebra M-P. Magnesium phosphate cements for endodontic applications with improved longâ€□term sealing ability. 2014;47(2):127–139. (International endodontic journal).

Mestres G, Ginebra M-P. Novel magnesium phosphate cements with high early strength and antibacterial properties. 2011;7(4):1853–1861. (Acta biomaterialia).

MichaÅ‚owski T, Pietrzyk A. A thermodynamic study of struvite water system. 2006;68(3):594–601. (Talanta).

Modak JM. Haber process for ammonia synthesis. 2002;7(9):69–77. (Resonance).

Moore Jr PA, Daniel TC, Edwards DR, Miller DM. Evaluation of chemical amendments to reduce ammonia volatilization from poultry litter. 1996;75(3):315–320. (Poultry science).

Moore PA, Daniel TC, Edwards DR, Miller DM. Effect of chemical amendments on ammonia volatilization from poultry litter. 1995;24(2):293–300. (Journal of environmental quality).

Morimoto T, Yanai H, Nagao M. Infrared spectra of ammonia adsorbed on zinc oxide. 1976;80(5):471–475. (The Journal of physical chemistry).

Moseke C, Saratsis V, Gbureck U. Injectability and mechanical properties of magnesium phosphate cements. 2011;22(12):2591–2598. (Journal of Materials Science: Materials in Medicine).

Muller J, Hakvoort G, Jansen JC. DSC and TG Study of Water Adosorption and Desorption on Zeolite NaA Powder and attached as layer on metal. 1998;53(2):449–466. (Journal of thermal analysis and calorimetry).

Nagao M, Morimoto T. Relation between Amounts of Chemisorbed Water and Ammonia on Zinc Oxide. 1976;49(11):2977–2980. (Bulletin of the Chemical Society of Japan).

Neagle W, Rochester CH. Infrared study of the adsorption of water and ammonia on calcium carbonate. 1990;86(1):181–183. (Journal of the Chemical Society, Faraday Transactions).

Neyens E, Baeyens J. A review of thermal sludge pre-treatment processes to improve dewaterability. 2003;98(1–3):51–67. (Journal of hazardous materials).

Nijem N, Fürsich K, Bluhm H, Leone SR, Gilles MK. Ammonia adsorption and co-adsorption with water in HKUST-1: spectroscopic evidence for cooperative interactions. 2015;119(44):24781–24788. (The Journal of Physical Chemistry C).

Niraula S, Rahman S, Chatterjee A. Temperature response of ammonia and greenhouse gas emission from manure amended silty clay soil. 2018;68(8):663–677. (Acta Agriculturae Scandinavica, Section B—Soil & Plant Science).

Nye PH. A model of ammonia volatilization from applied urea. III. Sensitivity analysis, mechanisms, and applications. 1986;37(1):31–40. (Journal of Soil Science).

Ozawa T. A new method of analyzing thermogravimetric data. 1965;38(11):1881–1886. (Bulletin of the Chemical Society of Japan).

Paerl HW, Huisman J. Climate change: a catalyst for global expansion of harmful cyanobacterial blooms. 2009;1(1):27–37. (Environmental microbiology reports).

Pagans E, Barrena R, Font X, Sánchez A. Ammonia emissions from the composting of different organic wastes. Dependency on process temperature. 2006;62(9):1534–1542. (Chemosphere).

Paillat J-M, Robin P, Hassouna M, Leterme P. Predicting ammonia and carbon dioxide emissions from carbon and nitrogen biodegradability during animal waste composting. 2005;39(36):6833–6842. (Atmospheric Environment).

Paillat J-M, Robin P, Hassouna M, Leterme P. Predicting ammonia and carbon dioxide emissions from carbon and nitrogen biodegradability during animal waste composting. 2005;39(36):6833–6842. (Atmospheric Environment).

Pan Y, Tian S, Liu D, Fang Y, Zhu X, Zhang Q, Zheng B, Michalski G, Wang Y. Fossil fuel combustion-related emissions dominate atmospheric ammonia sources during severe haze episodes: Evidence from 15N-stable isotope in size-resolved aerosol ammonium. 2016;50(15):8049–8056. (Environmental science & technology).

Panella B, Hirscher M, PÃ¼tter H, MÃ¼ller U. Hydrogen adsorption in metalâ€“organic frameworks: Cuâ€□MOFs and Znâ€□MOFs compared. 2006;16(4):520–524. (Advanced Functional Materials).

Paul I, Varghese G, Ittyachen MA. Thermal decomposition studies of struvites. 2002.

Peel RG, Benedek A, Crowe CM. A branched pore kinetic model for activated carbon adsorption. 1981;27(1):26–32. (AIChE Journal).

Pescatore AJ, Harter-Dennis JM. Effects of ferrous sulfate consumption on the performance of broiler chicks. 1989;68(8):1063–1067. (Poultry science).

Peterson GW, Wagner GW, Balboa A, Mahle J, Sewell T, Karwacki CJ. Ammonia vapor removal by Cu3 (BTC) 2 and its characterization by MAS NMR. 2009;113(31):13906–13917. (The Journal of Physical Chemistry C).

Petit C, Huang L, Jagiello J, Kenvin J, Gubbins KE, Bandosz TJ. Toward understanding reactive adsorption of ammonia on Cu-MOF/graphite oxide nanocomposites. 2011;27(21):13043–13051. (Langmuir).

Piatkowski L, Bakker HJ. Vibrational dynamics of the bending mode of water interacting with ions. 2011;135(21):214509. (The Journal of chemical physics).

Pires J, de Cavalho MB, Carvalho AP, Guil JM, Perdigon-Melon JA. Heats of adsorption of n-hexane by thermal gravimetry with differential scanning calorimetry (TG-DSC): A tool for textural characterization of pillared clays. 2000;48(3):385–391. (Clays and Clay Minerals).

Polat E, Karaca M, Demir H, Onus AN. Use of natural zeolite (clinoptilolite) in agriculture. 2004;12(1):183–189. (Journal of fruit and ornamental plant research).

Rabinovich A, Rouff AA, Lew B, Ramlogan MV. Aerated fluidized bed treatment for phosphate recovery from dairy and swine wastewater. 2018;6(1):652–659. (ACS Sustainable Chemistry & Engineering).

Rahman MM, Liu Y, Kwag J-H, Ra C. Recovery of struvite from animal wastewater and its nutrient leaching loss in soil. 2011;186(2–3):2026–2030. (Journal of hazardous materials).

Ramlogan MV, Arrue DA, Rouff AA. Evaluation of heat-treated struvite as a non-conventional sorbent for ammonia gas using STA-PTA-FTIR. 2018;6(2):2461–2469. (Journal of Environmental Chemical Engineering).

Ramlogan MV, Rouff AA. An investigation of the thermal behavior of magnesium ammonium phosphate hexahydrate. 2016;123(1):145–152. (Journal of Thermal Analysis and Calorimetry).

Reece FN, Bates BJ, Lott BD. Ammonia control in broiler houses. 1979;58(3):754–755. (Poultry science).

Ren L, Schuchardt F, Shen Y, Li G, Li C. Impact of struvite crystallization on nitrogen losses during composting of pig manure and cornstalk. 2010;30(5):885–892. (Waste Management).

Ro KS, Lima IM, Reddy GB, Jackson MA, Gao B. Removing gaseous NH3 using biochar as an adsorbent. 2015;5(4):991–1002. (Agriculture).

Rothrock Jr MJ, Szögi AA, Vanotti MB. Recovery of ammonia from poultry litter using flat gas permeable membranes. 2013;33(6):1531–1538. (Waste Management).

Rouff AA. Sorption of chromium with struvite during phosphorus recovery. 2012;46(22):12493–12501. (Environmental science & technology).

Rouff AA. Temperature-dependent phosphorus precipitation and chromium removal from struvite-saturated solutions. 2013;392:343–348. (Journal of colloid and interface science).

Rouff AA. The use of TG/DSCâ€“FT-IR to assess the effect of Cr sorption on struvite stability and composition. 2012;110(3):1217–1223. (Journal of thermal analysis and calorimetry).

Rouff AA, Juarez KM. Zinc interaction with struvite during and after mineral formation. 2014;48(11):6342–6349. (Environmental science & technology).

Rouff AA, Ma N, Kustka AB. Adsorption of arsenic with struvite and hydroxylapatite in phosphate-bearing solutions. 2016;146:574–581. (Chemosphere).

Rouff AA, Ramlogan MV, Rabinovich A. Synergistic removal of zinc and copper in greenhouse waste effluent by struvite. 2016;4(3):1319–1327. (ACS Sustainable Chemistry & Engineering).

Sanchez-Monedero MA, Cayuela ML, Roig A, Jindo K, Mondini C, Bolan N. Role of biochar as an additive in organic waste composting. 2018;247:1155–1164. (Bioresource technology).

Sarkar AK. Hydration/dehydration characteristics of struvite and dittmarite pertaining to magnesium ammonium phosphate cement systems. 1991;26(9):2514–2518. (Journal of Materials Science).

Scheirs J, Camino G, Tumiatti W. Overview of water evolution during the thermal degradation of cellulose. 2001;37(5):933–942. (European Polymer Journal).

Seinfeld JH, Pandis SN. Atmospheric chemistry and physics: from air pollution to climate change. John Wiley & Sons; 2016.

Sexton BA, Hughes AE. A comparison of weak molecular adsorption of organic molecules on clean copper and platinum surfaces. 1984;140(1):227–248. (Surface Science).

Shreve BR, Moore Jr PA, Daniel TC, Edwards DR, Miller DM. Reduction of phosphorus in runoff from field-applied poultry litter using chemical amendments. 1995;24(1):106–111. (Journal of environmental quality).

Silva CP, Jaria G, Otero M, Esteves VI, Calisto V. Waste-based alternative adsorbents for the remediation of pharmaceutical contaminated waters: Has a step forward already been taken? 2018;250:888–901. (Bioresource technology).

Smet E, Van Langenhove H, Maes K. Abatement of high concentrated ammonia loaded waste gases in compost biofilters. 2000;119(1–4):177–190. (Water Air and Soil Pollution). doi:10.1023/A:1005186327201

Smith VH, Tilman GD, Nekola JC. Eutrophication: impacts of excess nutrient inputs on freshwater, marine, and terrestrial ecosystems. 1999;100(1–3):179–196. (Environmental pollution).

Sommer SG. Effect of composting on nutrient loss and nitrogen availability of cattle deep litter. 2001;14(2):123–133. (European Journal of Agronomy).

Sugiyama S, Yokoyama M, Ishizuka H, Sotowa K-I, Tomida T, Shigemoto N. Removal of aqueous ammonium with magnesium phosphates obtained from the ammonium-elimination of magnesium ammonium phosphate. 2005;292(1):133–138. (Journal of colloid and interface science).

Suliman W, Harsh JB, Abu-Lail NI, Fortuna A-M, Dallmeyer I, Garcia-Perez M. Influence of feedstock source and pyrolysis temperature on biochar bulk and surface properties. 2016;84:37–48. (Biomass and Bioenergy).

Taddeo R, Honkanen M, Kolppo K, Lepistö R. Nutrient management via struvite precipitation and recovery from various agroindustrial wastewaters: Process feasibility and struvite quality. 2018;212:433–439. (Journal of environmental management).

Taghizadeh-Toosi A, Clough TJ, Sherlock RR, Condron LM. A wood based low-temperature biochar captures NH 3-N generated from ruminant urine-N, retaining its bioavailability. 2012;353(1–2):73–84. (Plant and Soil).

Talu O. Needs, status, techniques and problems with binary gas adsorption experiments. 1998;76:227–269. (Advances in Colloid and Interface Science).

Tao J, Rappe AM. Physical Adsorption: Theory of van der Waals Interactions between particles and clean surfaces. 2014;112(10):106101. (Physical Review Letters).

Thommes M. Physical adsorption characterization of nanoporous materials. 2010;82(7):1059–1073. (Chemie Ingenieur Technik).

Tsutomu I, Takashi A, Kuniaki K, Kikuo O. Comparison of removal efficiencies for ammonia and amine gases between woody charcoal and activated carbon. 2004;50(2):148–153. (Journal of Health Science).

Umbreit MH, Paukszta D. The influence of temperature (20â€“1000Â° C) on binary mixtures of solid solutions of CH3COOLiÂ· 2H2Oâ€“MgHPO4Â· 3H2O. 2009;404(20):3620–3636. (Physica B: Condensed Matter).

Van der Weerden TJ, Jarvis SC. Ammonia emission factors for N fertilizers applied to two contrasting grassland soils. 1997;95(2):205–211. (Environmental Pollution).

Vandré R, Clemens J. Studies on the relationship between slurry pH, volatilization processes and the influence of acidifying additives. 1996;47(2):157–165. (Nutrient Cycling in Agroecosystems).

VanLoon GW, Duffy SJ. Environmental chemistry: a global perspective. Oxford university press; 2017.

Vikrant K, Kumar V, Kim K-H, Kukkar D. Metalâ€“organic frameworks (MOFs): potential and challenges for capture and abatement of ammonia. 2017;5(44):22877–22896. (Journal of Materials Chemistry A).

Vikrant K, Kumar V, Kim K-H, Kukkar D. Metal–organic frameworks (MOFs): potential and challenges for capture and abatement of ammonia. 2017;5(44):22877–22896. (Journal of Materials Chemistry A).

VilliÃ©ras F, Cases JM, FranÃ§ois M, Michot LJ, Thomas F. Texture and surface energetic heterogeneity of solids from modeling of low pressure gas adsorption isotherms. 1992;8(7):1789–1795. (Langmuir).

Vorndran E, Ewald A, MÃ¼ller FA, Zorn K, Kufner A, Gbureck U. Formation and properties of magnesiumâ€“ammoniumâ€“phosphate hexahydrate biocements in the Caâ€“Mgâ€“PO 4 system. 2011;22(3):429–436. (Journal of Materials Science: Materials in Medicine).

de Vries S, Postma R, van Scholl L, Blom-Zandstra G, Verhagen J, Harms I. No title. 2016. (Economic feasibility and climate benefits of using struvite from the Netherlands as a phosphate (P) fertilizer in West Africa).

Vyazovkin S, Burnham AK, Criado JM, Pérez-Maqueda LA, Popescu C, Sbirrazzuoli N. ICTAC Kinetics Committee recommendations for performing kinetic computations on thermal analysis data. 2011;520(1–2):1–19. (Thermochimica acta).

Vyazovkin S, Chrissafis K, Di Lorenzo ML, Koga N, Pijolat M, Roduit B, Sbirrazzuoli N, Suñol JJ. ICTAC Kinetics Committee recommendations for collecting experimental thermal analysis data for kinetic computations. 2014;590:1–23. (Thermochimica Acta).

Walters WW, Chai J, Hastings MG. Theoretical phase resolved ammonia–ammonium nitrogen equilibrium isotope exchange fractionations: Applications for tracking atmospheric ammonia gas-to-particle conversion. 2018;3(1):79–89. (ACS Earth and Space Chemistry).

Wang Q, Awasthi MK, Ren X, Zhao J, Li R, Wang Z, Chen H, Wang M, Zhang Z. Comparison of biochar, zeolite and their mixture amendment for aiding organic matter transformation and nitrogen conservation during pig manure composting. 2017;245:300–308. (Bioresource technology).

Wang S, Nan J, Shi C, Fu Q, Gao S, Wang D, Cui H, Saiz-Lopez A, Zhou B. Atmospheric ammonia and its impacts on regional air quality over the megacity of Shanghai, China. 2015;5:15842. (Scientific reports).

Wang S, Zeng Y. Ammonia emission mitigation in food waste composting: a review. 2018;248:13–19. (Bioresource technology).

Wei Y, Van Houten RT, Borger AR, Eikelboom DH, Fan Y. Minimization of excess sludge production for biological wastewater treatment. 2003;37(18):4453–4467. (Water research).

Whitaker A. The decomposition of struvite. 1968;36(282):820–824. (Mineralogical Magazine and Journal of the Mineralogical Society).

Whitehead DC, Raistrick N. Ammonia volatilization from five nitrogen compounds used as fertilizers following surface application to soils. 1990;41(3):387–394. (Journal of Soil Science).

Witter E, Kirchmann H. Peat, zeolite and basalt as adsorbents of ammoniacal nitrogen during manure decomposition. 1989;115(1):43–52. (Plant and Soil).

Witter E, Lopez-Real J. Nitrogen losses during the composting of sewage sludge, and the effectiveness of clay soil, zeolite, and compost in adsorbing the volatilized ammonia. 1988;23(4):279–294. (Biological wastes).

Wu Y, Gu B, Erisman JW, Reis S, Fang Y, Lu X, Zhang X. PM2. 5 pollution is substantially affected by ammonia emissions in China. 2016;218:86–94. (Environmental Pollution).

Xie T, Reddy KR, Wang C, Yargicoglu E, Spokas K. Characteristics and applications of biochar for environmental remediation: a review. 2015;45(9):939–969. (Critical Reviews in Environmental Science and Technology).

Xu L, Penner JE. Global simulations of nitrate and ammonium aerosols and their radiative effects. 2012;12(4). (Atmospheric Chemistry & Physics Discussions).

Yakout SM, Elsherif E. Investigation of strontium (II) sorption kinetic and thermodynamic onto straw-derived biochar. 2015;33(6):579–586. (Particulate Science and Technology).

Yetilmezsoy K, Sapci-Zengin Z. Recovery of ammonium nitrogen from the effluent of UASB treating poultry manure wastewater by MAP precipitation as a slow release fertilizer. 2009;166(1):260–269. (Journal of hazardous materials).

Yin X, Han H, Gunji I, Endou A, Cheettu Ammal SS, Kubo M, Miyamoto A. NH3 adsorption on the Brönsted and Lewis acid sites of V2O5 (010): a periodic density functional study. 1999;103(22):4701–4706. (The Journal of Physical Chemistry B).

Zhang S, Shi H-S, Huang S-W, Zhang P. Dehydration characteristics of struvite-K pertaining to magnesium potassium phosphate cement system in non-isothermal condition. 2013;111(1):35–40. (Journal of thermal analysis and calorimetry).

Zhang T, Ding L, Ren H. Pretreatment of ammonium removal from landfill leachate by chemical precipitation. 2009;166(2–3):911–915. (Journal of hazardous materials).

Zhang Y, Ma Z, Zhang Q, Wang J, Ma Q, Yang Y, Luo X, Zhang W. Comparison of the physicochemical characteristics of bio-char pyrolyzed from moso bamboo and rice husk with different pyrolysis temperatures. 2017;12(3):4652–4669. (BioResources).

Zhao M, Wang S, Tan J, Hua Y, Wu D, Hao J. Variation of urban atmospheric ammonia pollution and its relation with PM2. 5 chemical property in winter of Beijing, China. 2016;16:1378–1389. (Aerosol Air Qual.Res).

Zheng W, Hu J, Rappeport S, Zheng Z, Wang Z, Han Z, Langer J, Economy J. Activated carbon fiber composites for gas phase ammonia adsorption. 2016;234:146–154. (Microporous and Mesoporous Materials).